

Highly-Ionized Gas in the Galactic Halo: A FUSE Survey of O VI Absorption toward 22 Halo Stars

J. Zsargó, K.R. Sembach, J.C. Howk¹

Department of Physics and Astronomy, The Johns Hopkins University, Baltimore, MD 21218

B.D. Savage

Department of Astronomy, University of Wisconsin, Madison, WI 53706

ABSTRACT

Far Ultraviolet Spectroscopic Explorer (*FUSE*) spectra of 22 Galactic halo stars are studied to determine the amount of O VI in the Galactic halo between ~ 0.3 and ~ 10 kpc from the Galactic mid-plane. Strong O VI $\lambda 1031.93$ absorption was detected toward 21 stars, and a reliable 3σ upper limit was obtained toward HD 97991. The weaker member of the O VI doublet at 1037.62 \AA could be studied toward only six stars because of stellar and interstellar blending problems. The measured logarithmic total column densities vary from 13.65 to 14.57 with $\langle \log N \rangle = 14.17 \pm 0.28$ (1σ). The observed columns are reasonably consistent with a patchy exponential O VI distribution with a mid-plane density of $1.7 \times 10^{-8} \text{ cm}^{-3}$ and scale height between 2.3 and 4 kpc. We do not see clear signs of strong high-velocity components in O VI absorption along the Galactic sight lines, which indicates the general absence of high velocity O VI within 2-5 kpc of the Galactic mid-plane. This result is in marked contrast to the findings of Sembach *et al.* who reported high velocity O VI absorption toward $\sim 60\%$ of the complete halo sight lines observed by *FUSE*. The line centroid velocities of the O VI absorption does not reflect Galactic rotation well. The O VI velocity dispersions range from 33 to 78 km s^{-1} with an average of $\langle b \rangle = 45 \pm 11 \text{ km s}^{-1}$ (1σ). These values are much higher than the value of $\sim 18 \text{ km s}^{-1}$ expected from thermal broadening for gas at $T \sim 3 \times 10^5 \text{ K}$, the temperature at which O VI is expected to reach its peak abundance in collisional ionization equilibrium. Turbulence, inflow, and outflow must have an effect on the shape of the O VI profiles. Kinematical

¹Current Address: Center for Astrophysics and Space Sciences, University of California at San Diego, C-0424, La Jolla, CA 92093

comparisons of O VI with Ar I reveal that 8 of 21 sight lines are closely aligned in LSR velocity ($|\Delta V_{LSR}| \leq 5 \text{ km s}^{-1}$), while 9 of 21 exhibit significant velocity differences ($|\Delta V_{LSR}| \geq 15 \text{ km s}^{-1}$). This dual behavior may indicate the presence of two different types of O VI-bearing environments toward the Galactic sight lines. The correlation between the H I and O VI intermediate velocity absorption is poor. We could identify the known H I intermediate velocity components in the Ar I absorption but not in the O VI absorption in most cases. Comparison of O VI with other highly-ionized species suggests that the high ions are produced primarily by cooling hot gas in the Galactic fountain flow, and that turbulent mixing also has a significant contribution. The role of turbulent mixing varies from negligible to dominant. It is most important toward sight lines that sample supernova remnants like Loop I and IV. The average $N(\text{C IV})/N(\text{O VI})$ ratios for the nearby halo (this work) and complete halo (Savage *et al.*) are similar (~ 0.6), but the dispersion is larger in the sample of nearby halo sight lines. We are able to show that the O VI enhancement toward the Galactic center region that was observed in the *FUSE* survey of complete halo sight lines (Savage *et al.*) is likely associated with processes occurring near the Galactic center by comparing the observations toward the nearby HD 177566 sight line to those toward extragalactic targets.

Subject headings: galaxies: halos - galaxies: structure - ISM: structure - ultraviolet: ISM

1. Introduction

The existence of a hot, low density Galactic halo was theoretically postulated to provide pressure support for cool clouds located at large distances from the Galactic plane (Spitzer 1956). Since that prediction, observational evidence has accumulated in support of this hot phase of the interstellar medium (ISM). Detections of absorption lines of highly-ionized atoms, such as O VI, N V, C IV, and Si IV (York 1974, 1977; Jenkins 1978a; Savage & Massa 1987; Sembach & Savage 1992; Savage, Sembach, & Lu 1997; Savage *et al.* 2000; Savage *et al.* 2002; Sembach *et al.* 2002; Wakker *et al.* 2002) suggest the widespread, but patchy, distribution of high temperature gas in the Galactic disk and halo. The detections of O VI are particularly important because the energy needed to ionize O V is 113.9 eV, well above the 54.4 eV ionization potential of He II. The amount of stellar flux capable of ionizing O V in the ISM is limited by strong photospheric He II absorption; therefore, it is likely that collisional ionization and not photoionization is the dominant source of O VI.

The presence of O VI in the Galactic halo and the detection of soft X-ray emission at high Galactic latitudes (Levine et al. 1976, 1977; Snowden et al. 1998) provide support to the existence of a hot Galactic halo.

Our best access to the interstellar O VI, the O VI 1031.93, 1037.62 Å resonance doublet, lies in a wavelength range that is only now being explored in detail. Apart from sporadic and short-lived programs to observe O VI with the Hopkins Ultraviolet Telescope (Davidsen 1993) and the *Orbiting and Retrievable Far and Extreme Ultraviolet Spectrometers* (Hurwitz & Bowyer 1995; Hurwitz et al. 1998; Windmann et al. 1998; Sembach, Savage, & Hurwitz 1999), our understanding of the Galactic distribution of this ion was limited until recently to the interstellar O VI survey by the *Copernicus* satellite (Jenkins 1978a,b). The situation has changed rapidly with the launch of the *FUSE* satellite, which was specifically designed for high resolution and high sensitivity studies of the 905 to 1187 Å spectral range. A primary objective of the *FUSE* program has been to quantify the distribution and properties of hot gas traced by O VI in the Galaxy and nearby universe. Initial studies of the hot gas in the Magellanic Clouds (Howk et al. 2002b; Hoopes et al. 2002) and the low-redshift universe (Sembach et al. 2001) have already been completed.

A large number of Galactic (~ 200) and extragalactic (~ 100) targets have been observed by the *FUSE* Science Team for the purpose of mapping the O VI distribution in the Galactic halo and disk. The halo study is based primarily on a survey of extragalactic objects (Savage et al. 2002; Sembach et al. 2002), while a sample of early-type stars is being used to study the properties of O VI in the Galactic disk at distances greater than those accessible with Copernicus (Jenkins 1978a,b). Extragalactic objects -AGNs and QSOs- offer better sky coverage above $|b| \sim 20^\circ$ in the Galactic halo, because only a handful of suitable halo stars are available. Also, observations toward extragalactic objects sample the full extent of halo gas, providing information on the outer regions of the halo where suitable Galactic targets are rare. However, the kinematical structure of the O VI absorption can be confusing, and it is often difficult to assess where the absorption occurs in the halo. The purpose of including early-type halo stars in the original sample was to provide information about the O VI distribution at intermediate distances away from the Galactic plane ($|z| \sim 0.5-3$ kpc). In the present work, we attempt to provide this information and fill in the distance gap between the disk and halo surveys.

The *FUSE* sample of Galactic halo stars is also well suited for comparisons of the highly-ionized atoms in regions of the Galaxy where many different physical processes may be occurring (see Shull & Slavin 1994). Most of the stars in our sample have been observed previously with the International Ultraviolet Explorer (*IUE*), the Goddard High Resolution Spectrograph (GHRS), or with the Space Telescope Imaging Spectrograph (STIS). Column

density measurements for Si IV, C IV, and N V are readily available in the literature (Sembach & Savage 1992, 1994; Savage & Sembach 1994; Savage, Meade, & Sembach 2001; Savage, Sembach, & Howk 2001) for comparison with O VI. The comparisons of the Si IV, C IV, N V, and O VI columns are important because the models of the hot gas in the Galactic halo predict different density ratios for the highly-ionized species. Several physical processes have been proposed to explain the production of these species in or near the interfaces between the hot and warm gas. These are the cooling Galactic fountain models (Shapiro & Field 1976; Shapiro & Benjamin 1991), cooling supernova remnant (SNR) models (Slavin & Cox 1992, 1993; Shelton 1998), and models that involve interfaces between hot and warm gas with either turbulent mixing (Begelman & Fabian 1990; Slavin, Shull, & Begelman 1993) or conductive heat transfer occurring in the presence of a magnetic field (Borkowski, Balbus, & Fristrom 1990).

This paper is organized as follows. We briefly describe the sample in §2 and the observations in §3. We mention the major difficulties encountered in the interpretation of the measurements and discuss the method used to derive column densities in §4. We present our findings on the distribution and kinematics of O VI in §5, and the O VI columns are compared with earlier and contemporary results on other highly-ionized atoms in §6. We comment on individual sight lines in §7, discuss our results in §8, and summarize our conclusions in §9.

2. Selection of the Sample

The *FUSE* Science Team obtained observations of 57 O- and B-type halo stars during the first two observing cycles of the mission (December 1999 - December 2001). We examined all of these observations and selected a sub-sample to use in the present analysis based on the quality of the data and the complexity of the stellar photospheric and wind features in the vicinity of the O VI 1031.93, 1037.62 Å doublet. In addition to these objects, the sample was expanded with four post asymptotic giant branch (PAGB) stars that have strong interstellar O VI absorption and very straightforward continuum placement in the spectral region of the O VI doublet. These objects were observed for Guest Investigator (GI) programs A026 (PI Heber) and A108 (PI Dixon) that are not related to the present investigation. We are grateful to these investigators for their permission to use their data.

The primary set of halo stars observed by the *FUSE* Team was designed to provide broad sky coverage, sampling as many directions through the Galactic halo as possible at distances (z) greater than ~ 500 pc from the Galactic plane. Since the number of known early-type stars in the halo is relatively small, the sample included stars ranging in spectral type from O6 to B3. The luminosity classes were dominated by giants and supergiants,

although a few main sequence stars with large projected rotational velocities ($v \sin i \gtrsim 100 \text{ km s}^{-1}$) were also included in the sample.

The inspection of the full halo star sample categorized many of the sight lines as being unsuitable for detailed interstellar O VI studies. In general, supergiants often had very complex stellar absorption in the vicinity of the O VI lines, and many of them had the added complication that their values of $v \sin i$ were found to be less than $\sim 100 \text{ km s}^{-1}$. We qualitatively categorized the objects into three classes based on an assessment of the stellar continua and line blending near 1032 \AA : (1) good, with straight-forward continuum placement and a clear picture of line identification and component structure, (2) satisfactory, with detailed modeling required to fully assess the continuum placement or identify absorption lines and blending (e.g., the overlap of the HD $R(0)_{6-0}$ $\lambda 1031.91$ and O VI $\lambda 1031.93$ lines), and (3) poor, with no reasonable prospects for accurate continuum placement or blending decontamination. Of these, we selected the category 1 (good) objects and those from category 2 (satisfactory) for which we had confidence in the continuum placement, line identification, and blending decontamination. The 22 sight lines that were selected for the present investigation (including the objects from the GI programs) are listed in Table 1. To help future investigations of the Galactic halo, we list the rejected stars in Table 2 with the reasons for the rejection and the categories we assigned to them. Figure 1 illustrates examples of category 1 (good), 2 (satisfactory), and 3 (poor) spectra. The interstellar absorption lines are clearly identifiable in the spectrum of HD 116852 (category 1), with moderate absorption from H_2 and a well-developed stellar wind continuum around 1032 \AA . The stellar continuum around O VI $\lambda 1031.93$ is straightforward toward HD 175876 (category 2), but the blending with Cl I, HD, and H_2 lines made the assessment of the O VI absorption at 1032 \AA difficult. The blending decontamination was further complicated by the presence of multiple components in H_2 absorption. We will discuss our decontamination procedure in §4.1 in more detail. Figure 1 also shows that the spectrum of HD 119069 (category 3) contains numerous blended and often unidentified photospheric lines, making the continuum placement and the assessment of the interstellar O VI absorption futile.

3. Data Reduction and Calibration

The details of the *FUSE* instrument design and inflight performance are discussed by Moos *et al.* (2000) and Sahnou *et al.* (2000). In brief, *FUSE* involves four co-aligned telescopes and Rowland-spectrographs that feed two microchannel-plate detectors. Two of these telescope/spectrograph channels are coated with SiC to provide reflectivity below 1000 \AA , while the other two mirrors and gratings have Al:LiF coatings for sensitivity in the $1000 -$

1187 Å range. We will refer to these pairs as SiC and LiF channels in the following discussion, respectively. The data can be taken either in time-tag mode (TTAG) in which each photon event is recorded by its position and arrival time, or in histogram mode (HIST) in which the data are binned to form a spectral image.

Table 3 describes the most important characteristics of the *FUSE* observations of the 22 stars used in the present investigation. The spectra of 14 stars were obtained in histogram mode, with the rest obtained in time-tagged mode. The light of the stars was centered in the large (30" × 30"; LWRS) aperture of the LiF1 channel in 17 cases. The small (1.25" × 20"; HRS) aperture was used for observations of HD 100340, and the 4" × 20" (MDRS) aperture was used for the remaining sight lines. Since the LiF1 channel provides the highest effective area in the wavelength region of the O VI doublet, we have restricted our analysis to data obtained in this channel. Other channels were used to verify the presence of some weak features (e.g., Cl I λ1031.51) as well as to check for fixed-pattern noise introduced by the microchannel-plate detectors.

We followed the basic data handling procedures discussed by Sembach et al. (2000) to reduce the individual exposures using the *FUSE* pipeline calibration software CALFUSE (v1.8.7). For time-tagged data, the photon event lists for an observation were merged before processing with CALFUSE. If the data were taken in histogram mode, the extracted spectra for the exposures were cross-correlated and co-added. When multiple observations were available, the spectra for the observations were also cross-correlated and co-added. The spectral resolution of the fully-reduced data is $\sim 20 \text{ km s}^{-1}$ (FWHM) for all observations. The S/N ratios per resolution element ranged from ~ 10 to ~ 90 and varied from sight line to sight line since the measured fluxes and exposure times were different.

The nominal reference frame for the *FUSE* wavelength calibration should be heliocentric; however, the absolute *FUSE* wavelength zero-point is typically quite uncertain. Corrections of 40-50 km s^{-1} to the CALFUSE calibration are not uncommon. Howk *et al.* (2002b) and Danforth *et al.* (2002), for example, found that a consistent shift of $-47 \pm 5 \text{ km s}^{-1}$ from the CALFUSE v1.8.7 wavelength solution was needed to bring the *FUSE* spectra of LMC/SMC stars onto a proper velocity scale. The magnitude of this error varies from sight line to sight line because the CALFUSE wavelength calibration errors include a sign error in the application of heliocentric correction in all CALFUSE versions prior to v2.0.5. Fortunately, most of the stars in our halo sample were observed with *IUE*, so we used the measurements of Savage *et al.* (2001a) to place the *FUSE* spectra into the proper Local Standard of Rest (LSR) frame. The corrections were calculated by matching the velocity centroids of Si II λ1808.01 in the *IUE* spectra and Si II λ1020.70 in the *FUSE* spectra. For consistency, we applied this procedure for every sight line when both *IUE* and *FUSE* mea-

surements were available, even if no wavelength calibration error was apparent in the *FUSE* spectra. Thompson, Turnrose, & Bohlin (1982) estimated a $\pm 4 \text{ km s}^{-1}$ (2σ) uncertainty for the absolute wavelength zero-point in *IUE* spectra when the object is properly centered in the *IUE* aperture. Therefore, the contribution of the *IUE* uncertainty to the wavelength zero-point uncertainty of the corrected *FUSE* spectra should be similar.

There were six cases, HDE 225757, HDE 233622, NGC 6397-ROB 162, NGC 5904-ZNG 1, NGC 5139-ROA 5342, and NGC 6723-III 60, for which no *IUE* observations were available. We used STIS observations of the Fe II 1608.45 Å line (measurement done by the authors) and *FUSE* spectra of Fe II λ 1055.26 to place the *FUSE* observations into the heliocentric reference frame for HDE 233622, while observations of H I emission (Hartmann & Burton 1997) and the Ar I λ 1048.22 line in the *FUSE* range were used for NGC 5904-ZNG 1. For the remaining sight lines, we could only estimate the magnitude of the errors in the heliocentric correction by comparing the *FUSE* spectra of the Ar I 1048.22 Å line processed by CALFUSE v1.8.7 to those processed by CALFUSE v2.0.5. A further correction for the motion of the Sun with respect to the LSR is necessary to place the heliocentric velocity scales into the conventional LSR frame. We assumed that the Sun is moving in the direction of $l = 56^\circ$, $b = 23^\circ$ at a speed of $+19.5 \text{ km s}^{-1}$ (Mihalas & Binney 1981).

Some of the analysis in our investigation depends on the comparison of absorption features at different wavelengths (e.g., the O VI doublet and several HD lines), so we examined the relative wavelength scale for each object carefully. The observations were binned by 4 pixels, resulting in a velocity sampling of $\sim 7.8 \text{ km s}^{-1}$ ($\sim 0.027 \text{ \AA}$). The standard pipeline processing generally provides relative wavelengths accurate to $\sim 6\text{--}8 \text{ km s}^{-1}$ (1σ) when comparing absorption features separated by intervals of more than a few Ångströms. Given these limitations for the reliability of velocity differences measured in our spectra, we concluded that only velocity differences greater than $10\text{--}15 \text{ km s}^{-1}$ could be considered significant for lines several Ångströms apart. A particularly important example of the *FUSE* wavelength calibration uncertainties is the consistent shift between the absorption profiles of the two O VI lines in spectra reduced by CALFUSE versions prior to v2.0.5. In their survey toward extragalactic sight lines, Wakker et al. (2002) found that a consistent $\sim +10 \text{ km s}^{-1}$ velocity correction to the O VI 1037.62 Å line was necessary to match the velocity profiles of the O VI doublet. In our work, we saw a similar consistent velocity difference between the line centroids of H₂ transitions from the same rotational level but with central wavelengths above and below 1040 Å in all LWRS observations; therefore, we applied a $+10 \text{ km s}^{-1}$ correction not only to the O VI 1037.62 Å line but also to Ar I λ 1048.22 when comparisons with the stronger O VI line or with Si II λ 1020.70 were made.

4. Analysis and Methodology

4.1. Continuum Determination and Contaminating Features

One of the major challenges in our investigation was to find reasonable stellar continua around the two O VI lines, especially in the spectra of B giants and supergiants. We were able to establish the stellar continuum around the $\lambda 1031.93$ line for all stars listed in Table 1. The continuum fits and the resulting normalized spectra are displayed in Figure 2. We were unable to fit the stellar continuum near the O VI $\lambda 1037.62$ transition for 16 stars due to the presence of strong, overlapping C II, C II*, and H₂ lines in this spectral region. For these stars, we could only perform a consistency check by removing the expected O VI contribution at 1037.62 Å and making sure that the residuals were reasonable for the sight lines. We scaled the strength of the O VI absorption at 1031.93 Å by 0.5 to estimate the O VI $\lambda 1037.62$ absorption. The weaker member of the O VI doublet was extracted toward HD 18100, HD 121968, HDE 225757, HDE 233622, NGC 6397-ROB 162, and NGC 5904-ZNG 1. Figure 3 shows the O VI $\lambda 1037.62$ continuum fits and normalized spectra for these sight lines. Generally, these continuum fits were unreliable due to the presence of the aforementioned atomic and molecular lines around 1037 Å. We used these profiles only to estimate the uncertainties in the total O VI column densities and to assess the saturation effects in the O VI absorption. In the subsequent analysis, the description of the O VI absorption and the comparison with other highly-ionized atoms are primarily based on the quantities inferred from the O VI 1031.93 Å line.

The difficulty in finding suitable continuum around the O VI doublet seriously limited our ability to assess the uncertainties introduced by the continuum placement. It is usually one of the major sources of uncertainties in studies of interstellar O VI toward stars and is often estimated by investigating alternative, but still acceptable, continua. Howk *et al.* (2002b) and Hoopes *et al.* (2002) give examples of such procedures and discuss the issues that affect the continuum placement toward early-type stars. Unfortunately, exploring alternative continua was not always possible for our sight lines and of limited use in many cases. As noted in §2, viable continuum placement was one criterion for sample selection. Many sight lines in our sample were borderline cases, for which finding any acceptable continuum is difficult. We found it necessary to base our error estimates only on the S/N of the spectra and the quality of the HD and Cl I decontamination for these sight lines. In Figure 2, we display several possible continuum fits for the sight lines where we explored alternative continua. In these cases, we include the uncertainties introduced by the continuum placement in our error estimates.

The other major difficulty of our study was posed by the presence of molecular and

atomic lines around the stronger member of the O VI doublet. The HD R(0) $\lambda 1031.91$ line was the most important “contaminant” for our sight lines. Occasionally, blending with the Cl I $\lambda 1031.51$ and H₂ R(4) $\lambda 1032.35$ lines also caused problems (like in the case of HD 175876, see below), but the O VI absorption profiles rarely extended to $|V_{LSR}| \geq 120 \text{ km s}^{-1}$ to interfere with these lines. Fortunately, we could use HD R(0) $\lambda 1042.85$ or $\lambda 1021.46$, H₂ R(4) $\lambda 1057.38$, and Cl I $\lambda 1004.67$ to estimate and remove the HD, H₂, and Cl I contaminations from the O VI absorption at 1031.93 \AA . We scaled the absorption profiles of these transitions by the appropriate $f\lambda$ ratios to calculate the HD, H₂, and Cl I contributions. Unresolved components that might be present in the HD, H₂, or Cl I absorption did not seriously affect the O VI decontamination, because the line strengths of the transitions used in the calculation are very similar to those of the offending lines. Since we estimate the contamination of O VI absorption around 1032 \AA by comparing transitions several Angstroms apart, we compare the profiles of Cl I $\lambda 1004.67$, H₂ R(4) $\lambda 1057.38$, HD R(0) $\lambda 1042.85$, and $\lambda 1021.46$ to those of H₂ P(3) $\lambda 1031.19$ or R(4) $\lambda 1032.35$, and look for relative wavelength calibration errors. The comparison never reveals significant LSR velocity differences between the last two H₂ lines and Cl I $\lambda 1004.67$ or HD R(0) $\lambda 1021.46$. In the cases of HD R(0) $\lambda 1042.85$ and H₂ R(4) $\lambda 1057.38$, we detect and correct for velocity shifts of $\sim 10\text{-}15 \text{ km s}^{-1}$.

The complex nature of extracting the O VI column density can be illustrated by the case of HD 175876. Figure 4 shows that there is considerable HD and Cl I contamination in the O VI $\lambda 1031.93$ absorption. The broad feature (FWHM $\sim 100\text{-}150 \text{ km s}^{-1}$) near $V_{LSR} \sim 0 \text{ km s}^{-1}$ in Figure 4 was initially thought to be of stellar origin; however, when we calculated the nearby Cl I, HD J=0, and H₂ J=4 profiles (see Figure 4), this assessment became ambiguous. Unfortunately, the weaker member of the O VI doublet is hopelessly blended with H₂ lines and is thus unavailable for comparison. After the removal of the Cl I, HD, and H₂ contributions, we conclude that there are two components in interstellar O VI absorption, more or less corresponding to the ones visible in the H₂ absorption.

4.2. Column Density Determination

The O VI halo cloud absorption is generally broad enough to be fully resolved by *FUSE*. In such cases, a very simple and efficient method for extracting information about the number of absorbing ions along the sight line is the apparent column density method (Savage & Sembach 1991). The observed flux from an astronomical source can be represented by

$$F(\lambda) = \int_0^\infty F_*(\lambda - \lambda') \exp(-\tau(\lambda - \lambda')) \Phi(\lambda') \delta\lambda' . \quad (1)$$

For *FUSE* data, the stellar continuum ($F_*(\lambda)$) varies slowly over the width of the line spread function ($\Phi(\lambda)$). Therefore, it is possible to estimate the stellar continuum at the wavelengths of the interstellar lines without having to explicitly deconvolve the stellar continuum from the observed spectrum. Thus, we can transform the observed flux to apparent optical depth by

$$\tau_a(\lambda) = \ln \left(\frac{F_*(\lambda)}{F(\lambda)} \right). \quad (2)$$

The apparent column density per unit velocity is defined as

$$N_a(v) = 3.768 \times 10^{14} \frac{\tau_a(v)}{\lambda_0 f}; \quad v = c \frac{\lambda - \lambda_0}{\lambda_0}, \quad (3)$$

where λ_0 , f , and c are the wavelength at the line center (in Å), the oscillator strength of the given transition, and the speed of light, respectively. When the line is fully resolved, the apparent column density per unit velocity is a valid representation of the true column density per unit velocity (see Savage & Sembach 1991; Jenkins 1996). In cases where the line is not fully resolved, the values of $N_a(v)$ may underestimate the true $N(v)$ if saturated structure exists within the profiles. This can be checked by comparing the $N_a(v)$ profiles for several lines of the same species having different values of $f\lambda_0$. Figure 5 shows the apparent column density comparison of the O VI doublet in the six cases when we could extract $N_a(v)$ profiles for both members of the doublet. Five of the 6 profiles in Figure 5 reveal little or no saturation near the line centers. Significant differences occur on the edges of the profiles ($|v_{LSR}| \geq 50 \text{ km s}^{-1}$), but this was expected since blending with strong C II, C II*, and H₂ lines limited the range where the weaker O VI line could be adequately extracted. HD 121968 is the only sight line that shows a modest level of saturation ($\leq 20\%$) near the line center. We explored whether alternative continua around O VI $\lambda 1037.62$ could improve the correspondence between the O VI profiles, and found that we could nearly eliminate the saturation with a marginally acceptable continuum. Since the level of possible saturation toward HD 121968 is small and it can be an artifact of the continuum placement, we did not make any correction for this saturation. The apparent column density profile comparison of the O VI doublet reveals that unresolved saturated structures do not affect most of the sight lines in Figure 5. We expect similar results to apply for the rest of our sight lines since the O VI profile widths and depths are similar for all sight lines in our sample.

We also used the apparent column density method to extract information on the kinematical structure of Ar I and Si II lines. These lines may be affected by unresolved saturated structures, but their kinematical characteristics are not altered significantly. We used the

Ar I and Si II lines for kinematical comparisons only and not for detailed column density determinations.

5. O VI in the Low Galactic Halo

5.1. Distribution of O VI in the Low Halo

The *FUSE* halo survey of Savage *et al.* (2002) mapped the O VI distribution in the Galactic halo (thick disk by their designation) using a sample of 100 extragalactic and 2 Galactic objects, covering much of the sky above $|b| \sim 20^\circ$. Our sample of 22 stars is too sparsely distributed over the sky to make a similar analysis of the halo at lower $|z|$ distances from the Galactic plane. Nevertheless, we can look for the phenomena and tendencies found by Savage *et al.* (2002) and provide important insights on remaining open questions.

Table 4 lists the total O VI columns (N) along our lines of sight, and other useful characteristics of the O VI absorption. The values of N were calculated by integrating the apparent column density profiles over the velocity intervals given in column 3 of Table 4. The logarithm of the total columns range from 13.65 to 14.57, with a median of 14.25. The logarithmic and linear averages are $\langle \log N \rangle = 14.17 \pm 0.28$ (1σ) and $\log \langle N \rangle = 14.24_{-0.36}^{+0.19}$ (1σ), respectively. We also list the projections of the total column densities perpendicular to the Galactic plane, $\log N_\perp = \log(N \sin|b|)$, in column 6 of Table 4. These vary from 13.13 to 14.48 with $\langle \log N_\perp \rangle = 13.77 \pm 0.37$ (1σ), $\log \langle N_\perp \rangle = 13.92_{-0.95}^{+0.28}$ (1σ), and a median of 13.74. The averages and medians are smaller while the standard deviations are greater than the respective values for the extragalactic sample ($\langle \log N \rangle = 14.36 \pm 0.18$ (1σ) and a median of 14.38; $\langle \log N_\perp \rangle = 14.21 \pm 0.23$ (1σ) and a median of 14.23; see Savage *et al.* 2002). The scatter of our measured O VI columns reflects not only the general patchiness of the O VI-bearing gas, but also a general increase of the O VI column density with distance. One can account for this effect in a simplified way by calculating the average densities ($\bar{n} = N_{tot}/d$) along the sight lines, which we list in column 7 of Table 4. The median, average, and standard deviation of the average densities are $1.35 \times 10^{-8} \text{ cm}^{-3}$, $1.56 \times 10^{-8} \text{ cm}^{-3}$ and $0.75 \times 10^{-8} \text{ cm}^{-3}$, respectively.

The large-scale distribution of O VI throughout the Galactic halo is often represented by an exponential function of height (z) above the Galactic disk:

$$n(|z|) = n_0 \exp\left(-\frac{|z|}{h}\right), \quad (4)$$

where n_0 is the mid-plane density of O VI, h is the scale height, and z is the height above or

below the Galactic plane. This is a very rudimentary approximation, but nevertheless useful in describing the O VI distribution within a few kiloparsecs from the Sun. From Equation 4 the vertical projection of the column density is

$$N_{\perp} \equiv N \sin|b| = n_0 h \left(1 - \exp\left(-\frac{|z|}{h}\right) \right). \quad (5)$$

Jenkins (1978b) estimated the mid-plane density and scale height to be $n_0 = 2.8 \times 10^{-8} \text{ cm}^{-3}$ and $h = 0.3 \text{ kpc}$, using *Copernicus* observations of hot stars (Jenkins 1978a; Jenkins & Meloy 1974) mainly in the Galactic disk. A reanalysis of these data by Shelton & Cox (1994) resulted in a new estimate of $n_0 = 1.3\text{-}1.5 \times 10^{-8} \text{ cm}^{-3}$, after taking the Local Bubble into account, and hinted at a larger scale height ($h = 3 \text{ kpc}$). The extragalactic survey by Savage *et al.* (2002) confirms that O VI is not confined to the Galactic plane and suggests a scale height of $h \sim 2.5 \text{ kpc}$. The combined analysis of the *Copernicus* and *FUSE* disk star sample by Jenkins *et al.* (2002) yields a mid-plane density of $n_0 = 1.7 \times 10^{-8} \text{ cm}^{-3}$.

In Figure 6 we plot our values of N_{\perp} (triangles in the upper panel) as a function of $|z|$ on a logarithmic scale, together with the values from the main *FUSE* O VI survey (circles in the lower panel; Savage *et al.* 2002) and the *Copernicus* measurements toward disk stars (squares in the lower panel; Jenkins 1978a). The $|z|$ values of the extragalactic targets that were used to produce Figure 6 are arbitrary; their actual numerical values are irrelevant as long as they are much larger than the O VI scale height. In Figure 6 we also plot three exponential distributions with $n_0 = 1.7 \times 10^{-8} \text{ cm}^{-3}$ and three scale heights. The curves correspond to $h = 1 \text{ kpc}$ (dashed line), $h = 2.5 \text{ kpc}$ (solid line), and $h = 4 \text{ kpc}$ (dotted line). All data are reasonably consistent with a patchy exponential distribution with $n_0 = 1.7 \times 10^{-8} \text{ cm}^{-3}$ and a scale height between 2.3 and 4 kpc. The average N_{\perp} of the extragalactic sample should be a very good measure of the O VI scale height since $\langle N_{\perp} \rangle \sim n_0 h$ from Equation 5; however, Savage *et al.* (2002) found an intriguing asymmetry in the average O VI columns of the two Galactic hemispheres. In particular, $\langle \log N_{\perp} \rangle$ is ~ 0.25 dex higher in the northern Galactic sky than it is in the southern sky. To visualize this asymmetry in $\langle \log N_{\perp} \rangle$, we separated the northern and southern extragalactic targets in Figure 6 by increasing $|z|$ tenfold toward each sight line with $b \geq 0^\circ$. Figure 6 shows that the subsample of northern extragalactic sight lines supports a larger O VI scale height ($h \sim 4 \text{ kpc}$) than the one suggested by the southern extragalactic targets. It is also apparent in the upper panel of the figure that the halo star measurements are also favoring an exponential distributions with higher values of h ($\sim 4 \text{ kpc}$). Savage *et al.* (2002) chose to describe the O VI distribution in the Galactic halo by a combination of an exponential distribution and an excess of O VI in the northern Galactic sky. To examine whether the excess O VI in the Northern sky is reflected by a separation of the measurements made toward northern and southern Galactic stars we display all the data

toward Galactic targets with solid symbols if their Galactic latitude is greater than 0° and $|z|$ is greater than 250 pc. Figure 6 shows that the high $|z|$ region of the low halo sample is dominated by stars in the northern Galactic hemisphere while there are more southern sight lines at lower $|z|$. Unfortunately, the low halo sight lines are not well distributed to assess where the O VI excess in the northern sky occurs. Measurements toward southern stars with higher z are necessary resolve this question.

In Figure 7 we display a Hammer-Aitoff projection of the measured O VI column densities on the sky. The Galactic Center is in the middle of the figure and Galactic longitude increases to the left. The diameter of each circle is scaled by the corresponding O VI column density. Open and closed symbols represent measurements for stars with $d > 3$ kpc and $d \leq 3$ kpc, respectively. We see in Figure 7 that there is a slight excess of O VI in the northern sky; however, this is an artifact of Galactic sight lines sampling material to different distances.

5.2. Kinematics of O VI in the Low Halo

Figure 8 displays the observed normalized absorption profiles of the O VI doublet for comparison with those of the Ar I $\lambda 1048.22$ and Si II $\lambda 1020.70$ lines. We see multiple O VI components clearly along only four sight lines: HD 175876, HD 177989, NGC 6397-ROB 162, and NGC 6723-III 60; there are also strong indications for multiple components in the O VI absorption toward HD 121800 and HDE 233622. We do not see strong high-velocity ($|V_{LSR}| \geq 100 \text{ km s}^{-1}$) O VI absorption toward any of the halo stars. The general absence of high-velocity features greatly simplified the analysis since the absorption from O VI was rarely blended with the H₂ $P(3)$ $\lambda 1031.19$ or H₂ $R(4)$ $\lambda 1032.35$ lines. It is still possible, however, that weak high-velocity absorption was overlooked due to continuum placement or simply because it was masked by H₂ absorption at $\sim -214 \text{ km s}^{-1}$ and $+124 \text{ km s}^{-1}$ relative to the O VI $\lambda 1031.93$ line. There were three sight lines, HD 88115, HD 100340 and NGC 5139-ROA 5342, with extended wings in the O VI absorption at 1032 Å. They are the best candidates for showing weak high-velocity absorption in our sample. However, the continuum placement around O VI $\lambda 1031.93$ is ambiguous toward HD 100340 and NGC 5139-ROA 5342. Therefore, the strongest evidence for high velocity absorption is the negative velocity absorption wing toward HD 88115 extending to $\sim -150 \text{ km s}^{-1}$.

In Table 5 we compare the relevant kinematical characteristics of the O VI $\lambda 1031.93$ and Ar I $\lambda 1048.22$ lines to those of C IV $\lambda 1548.20$, and Si IV $\lambda 1393.76$ from Savage *et al.* (2001a). We use Ar I for comparison to highlight the differences (or similarities) between the truly neutral and the highly-ionized gas. The Si II absorption shares many but not all the features displayed by the Ar I absorption in Table 5 since Si II traces both the neutral

and weakly ionized gas. The average line centroids and velocity dispersions of the species were calculated by the expressions

$$\langle v \rangle = \frac{\int v N_a(v) dv}{\int N_a(v) dv} \quad (6)$$

and

$$b = \sqrt{2} \sqrt{\frac{\int (v - \langle v \rangle)^2 N_a(v) dv}{\int N_a(v) dv}}, \quad (7)$$

where $N_a(v)$ is the measured apparent column density per unit velocity. The quantity b is only formally related to the well-known Doppler parameter, and it becomes the b -value only if the distribution is Gaussian. It includes all the instrumental effects, thermal and turbulent broadening, and can be affected by the presence of multiple components.

Table 5 reveals close alignment ($|\Delta \langle v \rangle| \leq 5 \text{ km s}^{-1}$) between the line centroid of the O VI absorption and that of the Ar I in 8 of 21 cases (HD 97991 is not included since O VI is not detected). Velocity differences greater than 15 km s^{-1} are observed in 9 cases. Only four sight lines exhibit velocity differences that are between 5 and 15 km s^{-1} . The dual behavior of O VI with respect to Ar I may indicate the presence of two different types of O VI-bearing environments in the low halo. We see significant shifts between the centroids of the O VI and Ar I absorption toward the sight lines with multiple O VI components and toward BD+38 2182, HD 100340, HD 121800, and JL 212. These velocity differences are greater than 15 km s^{-1} . The shift of the O VI line or the position of the extra component is usually toward positive velocities with respect to the Ar I lines. We see blueshifted components or significant blueshifts of the O VI centroids in three cases: the HD 175876, HDE 233622, and vZ 1128 sight lines.

Table 5 also reveals significant differences between the average velocities of C IV and Si IV and those of O VI. These differences are occasionally very large. Discrepancies in the average velocities can occur if the distributions of the highly-ionized species are different along the line of sight. If there are multiple absorbing components along a sight line with different O VI, C IV, and Si IV abundances, then the average velocities calculated over the entire line profiles could be significantly different. Such observations are not uncommon; for example, Savage *et al.* (2001b) measured different high ion ratios in the absorbing components toward HD 177989. Unfortunately, the uncertainties of our wavelength calibration could contribute to the velocity differences, but are not likely to be the explanation for all of them since the differences are larger than $10\text{-}15 \text{ km s}^{-1}$ in many cases.

To examine whether Galactic rotation has an imprint on the observed LSR velocities, we created a simple model to predict the expected rotational velocities of the O VI along these sight lines. We used the Galactic rotation curve of Clemens (1985) for the disk and assumed that the halo and disk corotate. The O VI was assumed to be exponentially distributed perpendicular to the disk with a scale height of 2.5 kpc. A turbulent velocity dispersion of $b = 60 \text{ km s}^{-1}$ (Savage *et al.* 2002) was assumed for the non-rotational motions in the lower halo. Figure 9 displays the observed and predicted O VI line centroid velocities for our sight lines. There is no apparent correlation between the predicted Galactic rotation and the observed velocities. The observed average velocities range from ~ -30 to $\sim 30 \text{ km s}^{-1}$ for sight lines with $|V_{exp}| \leq 20 \text{ km s}^{-1}$, which implies that the Galactic rotation does not play a significant role in shaping of the average velocities along the sight lines. The imprint of Galactic rotation in the LSR velocity distribution is limited by the fact that most of our targets are relatively nearby and at higher latitudes, resulting in low expected rotation velocities. In this case, the non-rotational motions like inflow/outflow in the high- z region dominate the average motion of the absorbing material. The fact that we see both excess positive and negative velocities with respect to the predicted rotational velocities indicates that no large scale motion dominates the low halo within 3-5 kpc of the Sun, and that the O VI-bearing gas participates both in inflow and outflow.

Table 5 also gives measures of the line-widths (b -values) for the high-ionization species. The typical line width of O VI is much broader than that expected from a pure thermal broadening in gas at $T_{kin} \sim 3 \times 10^5 \text{ K}$ ($b \sim 18 \text{ km s}^{-1}$). We find that the line dispersion for O VI varies from $b \sim 33 \text{ km s}^{-1}$ to $\sim 78 \text{ km s}^{-1}$. The average, median, and the standard deviation of the line breadths are 45 km s^{-1} , 44 km s^{-1} , and 11 km s^{-1} , respectively. Savage *et al.* (2002) found a $\langle b \rangle = 61 \pm 15 \text{ km s}^{-1}$ (1σ) and a median of 59 km s^{-1} for the full extragalactic sample. The values derived for the Galactic disk by Jenkins (1978a) vary from 10.7 to 56 km s^{-1} with a median of 27 km s^{-1} . The line dispersions in all three samples are larger than the b -value expected from thermal broadening in a gas at $T \sim 3 \times 10^5 \text{ K}$, which suggests that O VI is produced in multiple environments dominated by inflow, outflow, and turbulence. The progressive increase of the average line widths from the disk to the Galactic halo likely reflects an increase in the number of the O VI-bearing environments. Table 5 also shows that the widths of Si IV, C IV, and O VI are similar, with a tendency for the O VI line widths to be slightly larger than those of C IV and Si IV. The C IV and Si IV line widths track each other closely. The average values of $\langle b(\text{C IV}) \rangle = 37 \pm 10 \text{ km s}^{-1}$ (1σ) and $\langle b(\text{Si IV}) \rangle = 34 \pm 9 \text{ km s}^{-1}$ (1σ) are nearly identical. The linear Pearson correlation coefficient of the Si IV and C IV b -values in Table 5 is 0.89, while the same statistical test between the O VI and Si IV/C IV breadths produce correlation coefficients less than 0.5. It is possible, therefore, that some of the O VI along the halo star sight lines sample environments

different from those where the majority of Si IV and C IV reside. Even though the effects of instrumental broadening of *IUE* and *FUSE* on the calculated b -values are similar, caution is required when assessing the significance of this difference between the C IV/Si IV (*IUE*) and O VI (*FUSE*) b -values.

6. Comparison of O VI, C IV, Si IV, and N V Column Densities

O VI is a good tracer of gas in the transitional state between the hot ($T \sim 10^6$ K) and warm ($T \sim 10^4$ K) phases of the ISM. The observed quantities of O VI are most readily produced by collisional ionization at temperatures $T \sim (3 - 5) \times 10^5$ K (Sutherland & Dopita 1993). In this temperature regime, the gas experiences rapid radiative cooling, and the observed amount of O VI should be eliminated in a relatively short time. Therefore, it is likely that hot ($T \gtrsim 10^6$ K) gas is continuously injected into the Galactic halo, replenishing the gas at “transition temperatures” ($T \sim 10^5 - 10^6$ K), as it cools or comes into contact with colder material. The most likely source of the hot, low density gas is the temporally and spatially correlated supernova bursts in OB associations of the Galactic disk. The superbubbles created by these supernovae are thought to break through the denser material of the disk and eject the hot gas in their interiors into the Galactic halo (Norman & Ikeuchi 1989). O VI could then be produced either within the cooling hot gas of the supernova remnants or at the interfaces between the hot gas of the remnant and the ambient interstellar medium.

More can be learned if O VI is studied in conjunction with other highly-ionized species, such as N V, C IV and Si IV. The theories that are proposed to explain the observed quantities of these highly-ionized species, predict different abundance ratios of these ions. Sembach, Savage, & Tripp (1997) summarize these differences in their Table 10 for the most widely accepted models. Of these, the turbulent mixing layer models produce ratios that are the most model specific. Predictions of the other models are fairly similar, usually too close to favor any one model when only a single ion ratio is available and the uncertainties of the respective densities are large.

The behavior of interstellar N V and O VI are similar in some respects. The source of N IV and O V ionization is likely to be primarily collisional. Due to photospheric shielding by He II in normal hot stars, the available stellar flux above $h\nu \geq 54.4$ eV is too low to produce the observed O VI and N V columns in the quiescent warm phase of the ISM. Unfortunately, information about interstellar N V is very limited. The N V doublet around 1240 Å is often very weak and not readily seen in low resolution or low signal-to-noise data. The Si IV and C IV doublets around 1400 Å and 1550 Å, on the other hand, are almost always measurable

and can offer a valuable opportunity for comparison with O VI. Attention is required in this comparison, however, because Si IV and, to a lesser extent, C IV can be produced by photoionization in an environment different from that in which O VI resides. Unlike O V and N IV, the ionization potentials of both Si III and C III are lower than that of He II.

Savage *et al.* (2001a) analyzed *IUE* spectra of the C IV and Si IV doublets and presented total column densities and $N_a(v)$ profiles for 164 early-type stars, including 15 of our sight lines. In addition, high resolution GHRs measurements of the Si IV, C IV, and N V doublets are available for HD 18100 and HD 100340 (Savage & Sembach 1994), and for HD 116852 (Sembach & Savage 1994). Furthermore, Savage *et al.* (2001b) measured column densities of these ions toward HD 177989 using both GHRs and STIS spectra. With the available data, a detailed comparison of C IV, Si IV, N V, and O VI is possible.

6.1. Column Density Ratios of the Highly-ionized Species

6.1.1. Sight-line-averaged Values

Traditionally, the number density ratios of highly-ionized species are approximated by the ratios of the measured total column densities. Table 6 shows the observed $N(\text{C IV})/N(\text{Si IV})$, $N(\text{C IV})/N(\text{O VI})$, $N(\text{Si IV})/N(\text{O VI})$, and $N(\text{N V})/N(\text{O VI})$ ratios with their 1σ errors for those sight lines in our sample that have C IV, Si IV, or N V measurements available in the literature. The sample averages and the 1σ dispersions of the respective ion ratios, together with the various model predictions, are also shown in the table. The sample of $N(\text{C IV})/N(\text{Si IV})$ ratios in column 2 of Table 6 is not well enough constrained to study the processes that are responsible for the production of highly-ionized species in the Galactic halo. We have only lower limits for this ratio in five cases that are consistent with all proposed models. The allowed values and limits are generally less than 5 with a sample average of 3.5 ± 1.1 . This is somewhat smaller than the Galactic average of 4.3 ± 1.9 (Sembach *et al.* 1997), but the two values are still in reasonable agreement. The values of the $N(\text{C IV})/N(\text{Si IV})$ ratio in Table 6 are within the predicted ranges of the cooling Galactic fountain or the turbulent mixing layer models, while the cooling SNR or conductive interface models predict ratios that are much greater than the observed values.

The $N(\text{C IV})/N(\text{O VI})$ ratios in column 3 of Table 6 range from 0.2 to 3.08 with most of the values below unity and often less than 0.5. Without the lower and upper limits the sample average is 0.60 ± 0.47 , which is essentially identical to the average ratio of 0.62 ± 0.10 that was found for complete paths through the thick disk/halo (Savage *et al.* 2002). The large dispersion on our values suggests that C IV and O VI are produced by a diverse set

of environments along the sight lines and that the ratios cannot be explained by a single model. We can classify the $N(\text{C IV})/ N(\text{O VI})$ ratios in Table 6 into three groups. The first group involves eight sight lines with ratios that are between 0.1 and 0.5. These values are the most consistent with the predictions from the cooling Galactic fountain models or with those from the conductive interface models. The cooling SNR model predicts ratios that are somewhat lower than these observations. The second group consists of three sight lines with ratios greater than unity. Such values are predicted only by the turbulent mixing layer models. The third group of the remaining sight lines has values between 0.5 and 1 that cannot be reconciled with any one of the model predictions. This apparent contradiction can be resolved easily if one considers that the proposed models are not exclusive. Observations that sample multiple C IV and O VI-bearing environments can exhibit total column density ratios that are intermediate between the values predicted by the models. For example, a sight line that samples cooling hot gas in a superbubble and mixing hot and warm gas within the bubble walls will most likely exhibit a $N(\text{C IV})/ N(\text{O VI})$ ratio that is between 0.5 and 1.

The $N(\text{Si IV})/ N(\text{O VI})$ ratios in column 4 of Table 6 can be most readily produced by the cooling Galactic fountain or turbulent mixing layer models. The values are generally between 0.03 and 0.5 with the average of $N(\text{Si IV})/ N(\text{O VI})= 0.20\pm 0.13$. These ratios are too high to be produced by the cooling SNR or conductive interface models. Column 5 of Table 6 shows that the $N(\text{N V})/ N(\text{O VI})$ ratios are generally between 0.06 and 0.41 with an average of 0.12 ± 0.07 . This is marginally lower than the average ratio of 0.18 ± 0.05 measured for complete paths through the Galactic halo (Savage *et al.* 2002). Since O VI and N V behave similarly in the transition temperature gas, the models predict similar values for their ratio. The only exception is the turbulent mixing layer model that predicts the highest $N(\text{N V})/ N(\text{O VI})$ ratios, somewhat distinct from the predictions of the other models. Our sample of $N(\text{N V})/ N(\text{O VI})$ ratios shows that the cooling Galactic fountain and the turbulent mixing layer models are very successful in reproducing the observed $N(\text{N V})/ N(\text{O VI})$ ratios, but the cooling SNR and conductive interface models are also capable of explaining many of the observed values.

The synthesis of the results on the $N(\text{C IV})/ N(\text{Si IV})$, $N(\text{C IV})/ N(\text{O VI})$, $N(\text{Si IV})/ N(\text{O VI})$, and $N(\text{N V})/ N(\text{O VI})$ ratios suggests that O VI primarily traces cooling hot gas along most of the sight lines, and that there are contributions from other processes, most likely from turbulent mixing in the interfaces between the hot and warm ISM phases. This contribution varies from sight line to sight line. The high ion ratios toward approximately half of the targets in Table 6 are consistent with the predictions of the cooling Galactic fountain model of R. Benjamin (2002, private communication) without any contributions from turbulent mixing. On the other hand, turbulent mixing seems to be the primary high

ion producer toward HD 121968 and HD 177989. The ratios toward the remaining sight lines require comparable contributions from cooling hot gas and from turbulent mixing. These conclusions are well illustrated by Figures 10-12 where we plot the various high ion ratios against each other. Figure 10 shows the $N(\text{C IV})/N(\text{O VI})$ ratios as a function of the $N(\text{N V})/N(\text{O VI})$ ratios. In the figure, we display the values allowed by the various theoretical models by rectangles. Strictly speaking, this representation is incorrect because the ratios of the highly-ionized species are not independent from each other. However, the available information on the various model predictions did not permit us to explore such correlations; therefore, we decided to use this simple method to visualize the model predictions. Three groups of the sight lines are immediately apparent in the figure. The $N(\text{N V})/N(\text{O VI})$ and $N(\text{C IV})/N(\text{O VI})$ ratios toward HD 100340, JL 212, and probably toward HDE 233622 are well described by the cooling Galactic fountain model, while turbulent mixing is the dominant high ion producing mechanism toward HD 121968 and HD 177989. Ratios toward the HD 18100, HD 116852, and HD 148422 sight lines indicate mixed environments with varying contributions from the two aforementioned processes. Figures 11 and 12 support these conclusions. Sight lines like HD 121968 and JL 212 systematically have $N(\text{C IV})/N(\text{O VI})$, $N(\text{Si IV})/N(\text{O VI})$, and $N(\text{N V})/N(\text{O VI})$ ratios that are in agreement with the same model in all figures. Figures 10-12 also show no difference in the behavior of the high ion ratios measured toward northern and southern sight lines and suggest that the high ion-bearing environments are similar in the two Galactic hemispheres.

There is an important difference between the behavior of the ratios in Figure 10 and those in Figures 11 and 12. The conductive interface and cooling SNR models are viable models in the first figure while their predictions could not even be displayed in the last two. Figure 10 displays the $N(\text{C IV})/N(\text{O VI})$ and the $N(\text{N V})/N(\text{O VI})$ ratios that are the least affected by photoionization. The $N(\text{Si IV})/N(\text{O VI})$ ratio that is very sensitive to the photoionization effects are shown in the other two figures. Among the models we used in our study, only the cooling Galactic fountain model of R. Benjamin (2002, private communication) and the turbulent mixing layer model of Slavin *et al.* (1993) take photoionization into account. Contributions from photoionization could be very important for the cooling SNR and the conductive interface models because a hybrid model of photoionization and any of the two may also reproduce those $N(\text{C IV})/N(\text{O VI})$, and $N(\text{Si IV})/N(\text{O VI})$ ratios that are well described by the cooling Galactic fountain model. This phenomenon is also apparent in the $N(\text{C IV})/N(\text{Si IV})$ ratios in Table 6. Since Si IV is more readily produced by photoionization than C IV, the contribution from photoionization could lower the $N(\text{C IV})/N(\text{Si IV})$ ratio and explain why the conductive interface and cooling SNR model consistently overestimate this ratio. It is possible, therefore, that the success of the cooling Galactic fountain model in reproducing many of our high ion ratios may be the result of the

more sophisticated state of the modeling (included photoionization) rather than the actual role of cooling Galactic fountains in the high ion production. Incorporating photoionization into the cooling SNR model could be especially promising since this model underestimates C IV but correctly estimates N V for those sight lines that are consistent with the cooling Galactic fountain model (see Figure 10). The same is not true for the conductive interface model. Clearly, further theoretical work is necessary to fully assess the role of cooling SNRs and conductive interfaces in the production of highly-ionized atoms.

There are two sight lines in our sample, HD 177989 and HD 121968, that show high ion ratios that suggest a dominant role for turbulent mixing in the production of Si IV, C IV, N V, and O VI. HD 121968, for example, displays very large $N(\text{C IV})/N(\text{O VI})$, $N(\text{Si IV})/N(\text{O VI})$, and $N(\text{N V})/N(\text{O VI})$ ratios. Both HD 121968 and HD 177989 sample special regions on the sky. HD 121968 is behind the Radio Loop I and IV supernova remnants, while HD 177989 is behind the Scutum supershell. Sembach *et al.* (1997) observed anomalous $N(\text{C IV})/N(\text{Si IV})$ and $N(\text{C IV})/N(\text{N V})$ ratios toward Loops I and IV using GHRS observations of HD 119608 and 3C 273. The observed values were very different from the respective Galactic averages. Savage *et al.* (2001b) saw a similar deviant behavior in the gas associated with the Scutum supershell. They used high resolution STIS and GHRS spectra of HD 177989 to identify the component associated with the supershell and measure $N(\text{C IV})/N(\text{Si IV})$ and $N(\text{C IV})/N(\text{N V})$ ratios. A hybrid model, with equal contribution from turbulent mixing, cooling hot gas, and conductive heating was necessary to explain the deviant ratios toward both directions. The high values for $N(\text{C IV})/N(\text{O VI})$ and $N(\text{N V})/N(\text{O VI})$ ratios toward HD 121968 and HD 177989 show that the atypical behavior extends to O VI and confirms the increased importance of turbulent mixing toward these directions.

6.1.2. Column Density Ratios as a Function of LSR Velocity

To test the conclusions that were drawn from the comparison of the total columns, we also compared the column densities in the velocity bins of the respective absorption profiles. If the observed amounts of high ions are produced by mixed environments then one would expect significant variation in the ratios as a function of LSR velocity. Figure 13 shows such a comparison of C IV and O VI for our sight lines. The C IV $\lambda 1548.20$ profiles are *IUE* observations from Savage *et al.* (2001a), except for HDE 233622 and JL 212, which were extracted from STIS archival spectra. Detailed profile comparisons of high resolution STIS spectra of C IV and *FUSE* O VI observations also exist for HD 116852 (Fox *et al.* 2002) and for HD 177989 (Sterling *et al.* 2002). The upper panels in Figure 13 display the apparent column density profiles of the O VI $\lambda 1031.93$ and C IV $\lambda 1548.20$ lines rebinned to 10 km s^{-1}

velocity bins, while the lower panels show the $N(\text{C IV})/ N(\text{O VI})$ ratios in each velocity bin. The ratios are displayed only if their uncertainties were less than the ratios themselves, which excluded HD 3827, HD 88115, HD 97991, and HD 121800 from the detailed profile comparison.

The detailed comparison of $N_a(v)$ profiles could introduce additional difficulties not present in the comparison of total column densities. The resolution differences between the *IUE*, *STIS* and *FUSE* spectra, for example, could cause problems. Fortunately, we saw little or no saturation in the profiles of the O VI doublet whenever we could extract both members. Similarly, C IV appeared well-resolved for the sight lines presented here (Savage *et al.* 2001a), except in the case of HD 177989. Also, the *STIS* profile of C IV $\lambda 1548.20$ toward HDE 233622 showed no significant change after convolving with a line spread function that is appropriate for *FUSE* (FWHM $\sim 20\text{-}25 \text{ km s}^{-1}$). Therefore, we conclude that the different resolutions of *IUE*, *STIS*, and *FUSE* should not significantly affect the detailed comparison of C IV and O VI $N_a(v)$ profiles in most cases. The other difficulty arises from the relative wavelength calibration errors between the *FUSE* and the *IUE* spectra. Since we expect that these uncertainties are generally less than $\pm 10 \text{ km s}^{-1}$, we estimated the column density errors due to the wavelength calibration uncertainties by the magnitude of $N_a(v)$ changes that occurred in each velocity bin after moving the profiles by $\pm 10 \text{ km s}^{-1}$. These uncertainties, together with the statistical errors, are included in the error estimates of the $N(\text{C IV})/ N(\text{O VI})$ ratios displayed in the lower panels of Figure 13. Generally, the ratios at the line edges and at LSR velocities where abrupt changes in $N_a(v)$ occur are the most affected by velocity errors.

Most sight lines in Figure 13 show at least a modest level of variation in the $N(\text{C IV})/ N(\text{O VI})$ ratios, which may indicate the presence of multiple components with different ratios toward these sight lines. HD 121968 and HD 177989, which have very high integrated $N(\text{C IV})/ N(\text{O VI})$ ratios, clearly show the presence of several components, including one unusually high (≥ 2) ratio. The very high $N(\text{C IV})/ N(\text{O VI})$ ratios around $V_{LSR} \sim -40 \text{ km s}^{-1}$ toward HD 121968 are probably the reflections of the turbulent edge of Loop IV that this sight line passes through. Likewise, the component toward HD 177989 at $\sim 45 \text{ km s}^{-1}$ is associated with the turbulent environment of the Scutum supershell and has high $N(\text{C IV})/ N(\text{O VI})$ ratios. Sight lines like HD 18100 and HD 219188 that show moderate level of variations in the ratio across the line profiles also have total $N(\text{C IV})/ N(\text{O VI})$ ratios between 0.5 and 1. A combined model of turbulent mixing and cooling hot gas is necessary to explain these ratios. The sight lines whose total $N(\text{C IV})/ N(\text{O VI})$ ratios are most consistent with a single model (cooling Galactic fountain – HD 100340, HDE 233622, and JL 212) display relatively featureless $N(\text{C IV})/ N(\text{O VI})$ ratios as a function of LSR velocity. The detailed comparison of C IV and O VI columns, therefore, supports the conclusions

drawn by the comparison of the total column densities in §6.1.1.

6.2. High Ion Ratios as a Function of Distance from the Galactic Midplane

The vertical distribution of Si IV, C IV, and N V has been extensively studied in the past. Savage *et al.* (1997) examined a mixed sample of Galactic and extragalactic sight lines and found that the distributions of these ions are reasonably well-characterized by patchy exponential stratifications in the Galactic halo. The mid-plane densities and scale heights of Si IV, C IV, and N V are $n_0(\text{Si IV})=2.3 \times 10^{-9} \text{ cm}^{-3}$, $h(\text{Si IV})=5.1 \text{ kpc}$, $n_0(\text{C IV})= 9.2 \times 10^{-9} \text{ cm}^{-3}$, $h(\text{C IV})= 4.4 \text{ kpc}$, and $n_0(\text{N V})= 2.6 \times 10^{-9} \text{ cm}^{-3}$, $h(\text{N V})= 3.3 \text{ kpc}$, respectively. Our sample of high ion ratios toward Galactic halo stars also offers a valuable opportunity to study the vertical distribution of the highly-ionized species and completes the results of Savage *et al.* (1997) by including the O VI distribution in the investigation. Figures 14-17 display the different high ion ratios as functions of $|z|$ height of the background stars. Besides our measurements, we also show the ratios measured toward 6 disk stars (Spitzer 1996) and the available ratios toward extragalactic targets (Savage *et al.* 2002; Hoopes *et al.* 2002). The vertical distributions that are expected from the exponential stratifications of high ions are also plotted. We used the mid-plane densities and scale heights of Savage *et al.* (1997) for Si IV, C IV, and N V, as well as $n_0(\text{O VI})= 1.7 \times 10^{-8} \text{ cm}^{-3}$ and $h(\text{O VI})= 2.5 \text{ kpc}$ for O VI to calculate these predicted curves.

The exponential distributions of Savage *et al.* (1997) suggest that the $N(\text{C IV})/ N(\text{Si IV})$ ratios are relatively constant at most $|z|$. Figure 14 shows that the observed ratios are in agreement with this prediction up to the distant regions of the Galactic halo. The largest discrepancies occur in the disk sample, which involves nearby stars ($d \leq 0.3 \text{ kpc}$) with low and unreliable C IV and Si IV column densities. Despite the considerable dispersion in the $N(\text{C IV})/ N(\text{Si IV})$ ratio, Figure 14 shows that Si IV and C IV trace each other well and may be produced together in the same environment. The $N(\text{C IV})/ N(\text{O VI})$ ratios in Figure 15, on the other hand, do not follow the distribution predicted by the exponential stratifications. The observed ratios are much lower in the disk than the predicted value of ~ 0.54 . At intermediate z ($-0.5 \leq \log|z| \leq 0.5$) the low halo sight lines display a “chaotic” behavior in the $N(\text{C IV})/ N(\text{O VI})$ ratio. The average value of 0.6 ± 0.47 is close to the ratios predicted by the exponential distributions of C IV and O VI, but the dispersion is very large. The values range from 0.2 to 3.08 with no obvious correspondence to the $|z|$ heights of the background stars. The $N(\text{C IV})/ N(\text{O VI})$ ratios toward the complete sight lines of Savage *et al.* (2002) do not differ significantly from those in the Galactic sample, but their scatter is smaller. Also, no extragalactic sight line shows a ratio much lower than 0.5. The behavior of

the $N(\text{Si IV})/N(\text{O VI})$ and $N(\text{N V})/N(\text{O VI})$ ratios in Figure 16 and 17 are similar to that of $N(\text{C IV})/N(\text{O VI})$ in Figure 15. The ratios in the disk are generally very low while those in the halo are closer to the predictions, but with large dispersions. The scatter decreases with increasing $|z|$, and the extremely low ratios are rare toward the extragalactic targets.

It is difficult to understand the vertical distribution of the highly-ionized species without accurate information on the disk gas. Spitzer (1996) reported an average $N(\text{C IV})/N(\text{O VI})$ ratio of $0.15_{-0.07}^{+0.11}$ and $0.93_{-0.48}^{+0.97}$ in the disk and halo, respectively. This result is in marked contrast with the preliminary findings of E. Jenkins (2002, private communication) who found an average $N(\text{C IV})/N(\text{O VI})$ ratio of $0.62_{-0.32}^{+0.68}$ (shown by a cross-hatched region in Figure 15) in the disk based on a sample of 54 stars with $|z| \leq 0.4$ kpc. Since the later work is a more global assessment of the disk gas and involves a large sample of disk stars, it is likely that the sample of Spitzer (1996) is biased by selection effects. The high fraction of nearby stars in this sample indicates that the high ion ratios displayed for the disk in Figures 14-17 reflect the conditions in the local ISM and are not representative for the average disk gas. Unfortunately, the results of the Jenkins *et al.* (2002) survey are not yet available for detailed comparison. If their preliminary result for the $N(\text{C IV})/N(\text{O VI})$ ratios hold, then Figure 15 would show similar average $N(\text{C IV})/N(\text{O VI})$ ratios in the disk, low halo, and distant halo. Then, the only apparent difference between the halo and disk ratios is the gradual decrease of scatter and the disappearance of the extremely low ratios.

The $N(\text{Si IV})/N(\text{O VI})$ ratios in Figure 16 also indicate a possible peak around $\log|z| \sim -0.15$. Such a feature would be a strong departure from the distribution predicted by the simple exponential stratifications of Si IV and O VI. A closer inspection of Figure 15 reveals the possibility of a corresponding peak in the $N(\text{C IV})/N(\text{O VI})$ ratios. A similar enhancement in the $N(\text{Si IV})/N(\text{N V})$ and $N(\text{C IV})/N(\text{N V})$ ratios was observed by Savage *et al.* (1997), albeit at larger z heights ($\log|z| \sim 0.5$). Unfortunately, it is difficult to assess the exact nature of these features in the $N(\text{Si IV})/N(\text{O VI})$ and $N(\text{C IV})/N(\text{O VI})$ ratios since only limits on both ratios are available at the most crucial heights. If the peaks are real, they may indicate that ultraviolet radiation from OB associations is leaking out of superbubbles and producing C IV and Si IV without corresponding O VI and N V, as was predicted by Ito & Ikeuchi (1988).

Finally, to look for any large-scale structure, or longitude or latitude dependence of the high ion ratios, we displayed the Hammer-Aitoff projection of the Galactic distribution of the $N(\text{C IV})/N(\text{O VI})$ ratios in Figure 18. No large scale longitudinal or latitudinal distribution is apparent in the figure. The absence of latitude dependence is further supported by the fact that Figures 14-17 display no obvious difference in the behavior of the ratios measured toward the northern (solid symbols) and the southern (open symbols) sight lines.

7. Comments on Individual Sight Lines

In this section we comment on interesting sight lines, and compare our measurements to those of Savage *et al.* (2002) toward specific directions. Table 7 shows the characteristics of the thick disk and high velocity O VI absorption for those Galactic and extragalactic sight lines that are separated in direction by 8° or less. In general, the measured thick disk absorptions toward halo stars are less than those measured toward the extragalactic objects. This behavior is expected if the large-scale halo/thick disk O VI distribution follows an exponential stratification (see §5.1). We note, however, that the comparisons of these sight lines can be very problematic. The recent study of the Galactic O VI absorption toward the Magellanic Clouds (Howk *et al.* 2002c) revealed large column density variations on sub-degree scales, comparable to those observed over large angular scales (Savage *et al.* 2002). It is not yet clear whether this is a local phenomenon or applies to the entire O VI halo. One should therefore be very careful when comparing observations even with small angular separations. Despite these caveats, we believe that such comparisons can still provide useful insights on the distribution of O VI along a path, especially if more than two sight lines in the same general direction are involved. We limited the comparisons to those opportunities when three or more closely aligned targets were available in a given direction, and when these observations did not reveal significant column density variations on small angular scales. For example, the HD 219188 sight line is within $\sim 6^\circ$ of the directions toward NGC 7469 and NGC 7714 from the extragalactic sample. The measured thick disk O VI columns and the kinematical structures are very similar for these sight lines which make them suitable for comparison (see §7.4). This is in contrast with the situation toward HDE 233622, Mrk 106, and Mrk 116, another set of closely aligned Galactic and extragalactic sight lines in the general direction of $l \sim 160^\circ$ and $b \sim 45^\circ$. Here, a difference of ~ 0.24 dex between the measured O VI columns for the two extragalactic targets indicates the presence of significant small scale variations.

7.1. BD+38 2182, HD 121800, HDE 233622, and the Intermediate Velocity Clouds

BD+38 2182 is a sight line in the direction of high-velocity cloud Complex M in the northern Galactic hemisphere. Danly, Albert, & Kuntz (1993) constrained the distance to Complex M by using BD+38 2182 and the much closer star HD 93521, which is $\sim 1^\circ$ away from the direction of BD+38 2182. Unfortunately, *FUSE* has not observed HD 93521 as of August 2002. We used BD+38 2182 alone to compare the low- and high-ionization states toward Complex M. Ryans *et al.* (1997) detected several high and intermediate velocity com-

ponents in Ca II and Na I absorption. Of these, we see the intermediate velocity components near $\sim 50 \text{ km s}^{-1}$ in Ar I and Si II absorption (see Figure 8). They are probably present in C IV since the C IV lines have extended blue wings in Figure 13. There is no indication, however, that intermediate velocity components at these or any other velocities are present in O VI absorption. The average velocity of O VI is $\sim 3 \text{ km s}^{-1}$ smaller than the predicted velocity from Galactic rotation. It is likely that the O VI absorption toward BD+38 2182 is not related to the Intermediate Velocity Arch.

A similar phenomenon is apparent in the spectra of HD 121800, located behind the Intermediate Velocity Arch near Complex C. Absorption from intermediate velocity clouds (IVC9 and IVC19 in Wakker 2001) is present in the low-ionization states, but not in those of O VI or C IV. The average velocity of the O VI absorption is redshifted by $\sim 18 \text{ km s}^{-1}$ with respect to the predicted value from the Galactic rotation, and there is a strong and broad O VI component at $\sim 12 \text{ km s}^{-1}$ that has no counterpart in the absorption of the low-ionization states. The nature of this O VI component is not clear. However, we can conclude that the O VI absorption toward HD 121800 is probably not related to the Intermediate Velocity Arch. This is in contrast with the observation toward PG 1351+640, an extragalactic sight line near the direction of HD 121800 (see Table 7), where O VI absorption is detected at the velocities of both IVC9 and IVC19 (see Savage *et al.* 2002).

HDE 233622 lies toward the extension of the Low Latitude Intermediate Velocity Arch. Wakker (2001) reported an H I intermediate velocity cloud at LSR velocity of $\sim 40 \text{ km s}^{-1}$ toward this sight line. This intermediate velocity cloud is very prominent in Si II absorption but weak in Ar I. In this case, there is a corresponding component in O VI absorption, visible in the spectrum of both member of the O VI doublet at $\sim 40 \text{ km s}^{-1}$. The correspondence between O VI and H I intermediate velocity absorption seems plausible toward this sight line. This conclusion is further reinforced by the detection of O VI absorption at $\sim 40 \text{ km s}^{-1}$ toward two nearby extragalactic targets, Mrk 106 and Mrk 116 (see Table 7).

The absence of intermediate velocity O VI absorption toward BD+38 2182 and HD 121800 implies that the neutral and the weakly ionized intermediate velocity gas in these directions may not interface with hot ($T > 10^6 \text{ K}$) gas. If such an interface existed we would expect to see transition temperature gas ($10^4 \text{ K} < T < 10^6 \text{ K}$) traced by O VI in the interface, as the case is toward HDE 233622.

7.2. HD 175876, HD 177989, and the Scutum Supershell

The measured O VI column densities toward two stars in our sample, HD 175876 and HD 177989, provide an interesting opportunity to do some in-depth mapping of the Galactic O VI distribution. Both sight lines lie in the general direction of the Scutum Supershell (GS 018-04+44), which is centered at $l = 17.5^\circ$, $b = -4^\circ$ at a distance of $d \sim 3.5$ kpc and which spans about 5° on the sky (Callaway *et al.* 2000). HD 177989 is situated behind the Scutum supershell, while HD 175876 is in front of it (see Table 7). Sterling *et al.* (2002) concluded that the component at $V_{LSR} = +42$ km s $^{-1}$, having $N(\text{O VI}) = 7.76 \times 10^{13}$ cm $^{-2}$, is associated with the Scutum supershell by simultaneous component fits to the O VI and C IV profiles. A closer inspection of Figure 8 and 13 shows that this component is essentially absent in the O VI profiles of HD 175876 and is very prominent in those of HD 177989, which is in accord with the picture that the supershell is located between the two stars.

We measured a total O VI column of 2.04×10^{14} cm $^{-2}$ toward HD 177989 using the apparent column density method. If one subtracts $N(\text{O VI}) = 1.38 \times 10^{14}$ cm $^{-2}$, the value for HD 175876, a column density of 6.60×10^{13} cm $^{-2}$ can be associated with the Scutum supershell. This is in reasonable agreement with the value of $N(\text{O VI})$ estimated by Sterling *et al.* (2002).

There is also an interesting component toward HD 175876 at $V_{LSR} \sim -50$ km s $^{-1}$ that is present in O VI and Ar I, and possibly in C IV absorption (see Figure 8 and 13). Pottasch, Wesselius & Arnal (1980) observed a high-velocity cloud at $V_{LSR} \sim -95$ km s $^{-1}$ in the spectrum of HD 175754, just $\sim 1.5^\circ$ away from HD 175876 and roughly at the same distance. We could clearly see the high-velocity feature in C II $\lambda 1036.34$ and Fe II $\lambda 1144.94$ toward HD 175754, but the complex stellar wind features and strong H $_2$ absorption prevented us from extracting the O VI doublet (therefore, HD 175754 was not part of our survey). On the other hand, no high or intermediate velocity feature is apparent in the spectrum of HD 177989 at $V_{LSR} \sim -50$ to -95 km s $^{-1}$. It would be useful to clarify whether these features in the spectrum of HD 175754 and HD 175876 are related.

7.3. Sight Lines Toward the Galactic Center

An important finding of Savage *et al.* (2002) is the enhancement of O VI toward the region $l = 330^\circ$ to 36° just south of the Galactic disk. They measured large O VI columns toward PKS 2005-489, Tol 1924-416, Mrk 509, and ESO 141-G55 that could be either the result of processes occurring near the Galactic center or they may be associated with the Loop I supernova remnant. It was not possible to resolve this question based on the extragalactic

sight line measurements alone.

In Table 7, we list three Galactic and extragalactic sight lines that are closely aligned and lie in this general direction. HD 177566 and NGC 6723-III 60 are two sight lines in our sample that lie within $\sim 4^\circ$ and $\sim 8^\circ$ of the direction toward Tol 1924-416, respectively. The separation between HD 177566 and NGC 6723-III 60 is $\sim 5^\circ$. The measured O VI column toward HD 177566 is $\log N = 13.65_{-0.08}^{+0.06}$, the lowest in our sample, which is consistent with the very small distance to the background star ($d = 1.1$ kpc). We found a much higher column density of $\log N = 14.37_{-0.12}^{+0.10}$ toward NGC 6723-III 60, which is a PAGB star in a globular cluster roughly 8.8 kpc away. Savage *et al.* (2002) measured a $\log N(\text{O VI}) = 14.62 \pm 0.05$ for Tol 1924-416, the highest among the three sight lines. Surface brightness-diameter relations (Berkhuijsen 1973) resulted in an estimate of 130 ± 75 pc for the distance and 230 ± 135 pc for the diameter of Loop I; therefore, all of the three sight lines in question are behind the supernova remnant. Since we measure a very low O VI column for HD 177566 it is likely that the strong thick disk O VI absorption toward Tol 1924-416 and NGC 6723-III 60 is not related to the Loop I supernova remnant and probably arises near the central regions of the Galaxy.

There are two possible caveats with the above analysis. One is, of course, the possibility of small scale angular variation in the O VI column density. However, the difference between the observed O VI columns toward HD 177566 and Tol 1924-416 is almost tenfold. The probability for such a large variation over 4° is small, less than 10% (Howk *et al.* 2002c). The other problem is that the distance to HD 177566 is not well defined. Despite the uncertainties in its distance, we do not expect HD 177566 to be in front of the Loop I supernova remnant.

7.4. Directions with Weak O VI Absorption

The *FUSE* survey of O VI toward extragalactic targets (Savage *et al.* 2002) also found that the general region around $l = 80^\circ$ to 175° and $b = -30^\circ$ to -60° is deficient in O VI. Two of the sight lines with the smallest measured O VI columns in the extragalactic sample, NGC 7469 and NGC 7714, are toward this region (see Table 7). One of our sight lines, HD 219188 lies near the directions to NGC 7469 and NGC 7714, with an angular separation of $\sim 6^\circ$ from each. The observed thick disk O VI columns are $\log N = 13.96 \pm 0.09$, 13.85 ± 0.15 , and 13.97 ± 0.06 , for NGC 7469, NGC 7714, and HD 219188, respectively. The kinematical characteristics of the O VI absorptions, average LSR velocities, and line dispersions are also similar. This correspondence is remarkable since an exponential O VI stratification with $h(\text{O VI}) = 2.5$ kpc and a $z = -1.789$ kpc for HD 219188 predicts a ~ 0.29 dex column density

difference between the extragalactic and the HD 219188 sight lines. There may be little O VI absorption beyond $|z| \sim 2$ kpc in this general direction, which would explain the O VI deficiency observed by Savage *et al.* (2002).

8. Discussion

8.1. The Absence of High-Velocity Absorption

The lack of any evidence for strong or even weak high-velocity component in the O VI absorption toward our sight lines is in striking contrast with the results toward extragalactic targets. Sembach *et al.* (2002) studied the high-velocity O VI absorption toward 100 extragalactic objects and 2 distant halo stars. High velocity absorption was found toward $\sim 60\%$ of these targets. The average logarithmic column densities of these features was found to be 13.95 ± 0.34 , comparable to the lowest O VI columns in our sample. If high-velocity O VI absorption was as common toward halo stars as toward extragalactic targets one would expect 10-12 detections of high-velocity absorption in our sample. The general absence of high-velocity O VI absorption in the halo star sample is very important because it justifies the association of the thick disk O VI with the low velocity ($|V_{LSR}| \leq 100 \text{ km s}^{-1}$) gas. The difference between the high-velocity cloud statistics of the nearby halo and that of the more distant halo can be illustrated by the sight lines listed in Table 7. Primary examples are the closely aligned HD 121800, PG 1351+640, and Mrk 279 sight lines, or the direction toward HD 100340 and Mrk 734. The angular separation between the first three objects is $\sim 3^\circ$, but we do not see the high velocity O VI absorption toward HD 121800 that is present in the spectra of PG 1351+640 and Mrk 279. Similarly, there is a very strong high velocity O VI absorption toward Mrk 734 that is certainly not seen toward HD 100340. The general direction toward HD 219188, NGC 7469, and NGC 7714, or the direction toward JL 212 and Fairall 9 are also very interesting. Strong high-velocity O VI absorption from the Magellanic Stream has been detected toward the extragalactic objects, but no absorption at similar LSR velocities has been seen in the spectra of the halo stars. The non-detection toward the halo stars supports the association of these high velocity features with the Magellanic Stream.

The possibility remains, however, for the presence of weak high-velocity absorption in our sample. Such features could be overlooked due to the complex nature of the stellar continua around the O VI 1031.93 Å line or because they were blended with the H₂ $P(3)$ $\lambda 1031.19$ or H₂ $R(4)$ $\lambda 1032.35$ lines. HD 88115 and HD 100340 are the most promising candidates to show weak high velocity O VI absorption. Toward HD 100340, for example, we observed a red wing in the O VI profile that extends to $V_{LSR} \sim 140 \text{ km s}^{-1}$ and maybe related to the strong redshifted high velocity feature that is seen toward Mrk 734 (see Table 7). If the

positive velocity wing toward HD 100340 is real it supports the idea advanced by Sembach *et al* (2002) that the positive high velocity wings are due to the outflow of gas from the disk into the halo.

8.2. The Origin of the Highly-Ionized Gas in the Galactic Halo

Our results confirm that the origin and distribution of Si IV, C IV, N V, and O VI in the Galactic halo cannot be described in the framework of a single physical process. Observations toward halo stars reveal the diversity of the high ion producing environments. Most of the observed high ion ratios suggest the presence of cooling hot gas along the sampled path with a varying contribution from turbulent mixing in the interfaces of hot and warm material. Sight lines toward special regions in the sky (e.g., HD 121968 toward Loop I and IV, and HD 177989 toward the Scutum supershell) require a dominant role for turbulent mixing in order to reconcile the observations with the predictions. The observed similarities in the kinematical structures of Si IV and C IV absorption, as well as the kinematical differences between C IV/Si IV and O VI profiles suggest that photoionization may also contribute significantly to the Si IV and C IV production. Photoionization could be especially important in the superbubble walls where substantial UV flux is available from the OB associations within the bubble. Our observations highlight the need for hybrid models that predict the combined results of multiple physical processes. There have been several efforts to create such models. Ito & Ikeuchi (1988), for example, employed a combination of cooling fountain flow from superbubbles and photoionization by the EUV radiation from OB associations in the superbubbles to predict the Si IV, C IV, and N V columns. Another example is the hybrid model of Shull & Slavin (1994) which combines turbulent mixing and cooling SNR gas. The role of turbulent mixing was assumed to be increasing with $|z|$ to explain the different C IV and N V scale heights. Any of these models could be a promising candidate to describe our observations if their predictions for O VI columns were available.

The dual behavior of the O VI line centroids in comparison with the line centroids of the Ar I lines is a further evidence that several high ion producing mechanisms are at operation in the Galactic halo. We observe significantly different O VI and Ar I line centroids in 9 of 21 cases (excluding HD 97991). A poor correspondence between the LSR velocities of O VI and those of the colder gas are expected when the majority of the O VI is produced in cooling hot gas. However, we see good agreement between the line centroid velocities of the low- and high-ionization states in 8 of 21 cases, which is difficult to understand if O VI is only produced in cooling hot gas. Therefore, significant amount of O VI must be produced by turbulent mixing or thermal conduction in the interfaces between the hot and warm gas

since such an arrangement would naturally explain the kinematical correspondence between the low- and high-ionization states (Cowie *et al.* 1979).

Because of its large cross-section for photoionization (Sofia & Jenkins 1998; Jenkins *et al.* 2000), Ar I is easily ionized in the ISM and it therefore is not a good tracer of low column density neutral gas structures or of warm ionized gas structures. Such structures could also give rise to O VI absorption if the structures are surrounded by hot 10^6 K gas. An inspection of the line profiles in Figure 8 reveals that O VI is better aligned with Si II $\lambda 1020.70$ than with Ar I $\lambda 1048.22$. The Si II ion may represent a better comparison ion for O VI since it traces cool and warm gas with wider ranges of conditions than Ar I. Detailed intercomparisons of the kinematical relationships among O VI and the many other tracers of the cold neutral, warm neutral, and warm ionized gas along the 22 sight lines studied here would represent a valuable extension of this investigation. Such an investigation should be pursued with spectra extracted with the best possible wavelength calibrations.

9. Summary

We have measured the O VI $\lambda\lambda 1031.93, 1037.62$ absorption along partial path lengths through the Galactic halo toward 22 Galactic halo stars, and examined the O VI distribution within ~ 3 -5 kpc of the Galactic mid-plane. Our results are compared to the findings of Savage *et al.* (2002) and Sembach *et al.* (2002) toward 102 complete sight lines through the Galactic halo. We also study the role of different physical processes in the production of highly-ionized species by comparing the observed $N(\text{C IV})/N(\text{Si IV})$, $N(\text{C IV})/N(\text{O VI})$, $N(\text{Si IV})/N(\text{O VI})$, and $N(\text{N V})/N(\text{O VI})$ ratios to the predictions of the current models. Our main results are as follows:

1. Strong O VI absorption is observed at 1031.93 \AA in all of the directions, except toward HD 97991. We were able to extract the O VI absorption at 1037.62 \AA for 6 directions. We find that the total O VI logarithmic column densities vary from 13.65 to 14.57 with an average of $\langle \log N \rangle = 14.17 \pm 0.28$ and a median of 14.25. The logarithm of the column density perpendicular to the Galactic mid-plane for these partial paths varies between 13.13 and 14.48 with an average of $\langle \log N \sin |b| \rangle = 13.77 \pm 0.37$.

2. The O VI column densities toward the 22 halo stars are reasonably well described by a patchy exponential distribution. Our measurements are the most consistent with $n_0 = 1.7 \times 10^{-8} \text{ cm}^{-3}$ and a scale height between 2.3 and 4 kpc.

3. We do not see any strong or weak high-velocity component in the O VI absorption along our sight lines. Sembach *et al.* (2002) reported high velocity O VI absorption toward

~60% of the complete halo sight lines. The non-detection of high-velocity absorption in our sample suggests that these features originate in the distant halo and confirms the association of the thick disk gas with the low velocity ($|V_{LSR}| \leq 100 \text{ km s}^{-1}$) absorption in the O VI survey of Savage *et al.* (2002).

4. Comparison of the O VI and Ar I line centroid velocities reveals a mixed picture. Significant velocity differences ($\geq 15 \text{ km s}^{-1}$) are observed in 9 cases. Ar I and O VI are closely aligned ($|\Delta V_{LSR}| \leq 5 \text{ km s}^{-1}$) in 8 cases and there are 5-15 km s^{-1} differences in the remaining 4 cases. The dual behavior of O VI with respect to Ar I may indicate the presence of two types of O VI-bearing environments along the sight lines studied.

5. There is no obvious correlation between Galactic rotation and the measured LSR velocities of the O VI absorption. We see deviations from the predicted rotational velocities in positive and negative directions with equal frequency. The O VI-bearing gas in the low halo participates both in inflow and outflow toward the Galactic plane.

6. The velocity dispersions (b -values) of the O VI profiles vary from 33 to 78 km s^{-1} with an average of $45 \pm 11 \text{ km s}^{-1}$. These values are much larger than the profile widths $b \sim 18 \text{ km s}^{-1}$ expected at $T \sim 3 \times 10^5 \text{ K}$, the temperature at which O VI peaks in abundance in collisional ionization equilibrium. A considerable amount of turbulent broadening or the presence of multiple components is necessary to explain the observed line breadths. The average O VI line width is smaller toward the halo stars than it is along complete sight lines through the halo (Savage *et al.* 2002), reflecting the larger number of O VI-bearing structures along the complete sight lines.

7. Kinematical comparisons of the Si IV, C IV, and O VI line profiles reveal that the Si IV and C IV line centroids and line widths correlate with each other well but not with those of the O VI absorption. There may be a substantial amount of photoionized C IV and Si IV without corresponding O VI along the sight lines.

8. The origin of the highly ionized species in the halo cannot be described by a single physical process. The observed $N(\text{C IV})/N(\text{Si IV})$, $N(\text{C IV})/N(\text{O VI})$, $N(\text{Si IV})/N(\text{O VI})$, and $N(\text{N V})/N(\text{O VI})$ ratios along the sight lines suggest that the highly-ionized species are most readily produced by cooling gas in a Galactic fountain flow with contributions from the turbulent interfaces between hot and warm gas. The role of turbulent mixing varies from sight line to sight line.

9. The high $N(\text{C IV})/N(\text{O VI})$ ratios toward HD 121968 behind the Loop I and IV supernova remnants, and toward HD 177989 behind the Scutum supershell suggest that turbulent mixing has a dominant role in producing C IV and O VI toward the disturbed environments of supernova remnants and supershells.

10. Detailed comparisons of the C IV and O VI profiles reveal modest to large variations in the $N(\text{C IV})/N(\text{O VI})$ ratios across the line profiles. We see the largest fluctuations when turbulent mixing has an important role in the production of C IV and O VI.

11. The vertical distribution of the high ion ratios toward the halo stars (present analysis) and the complete (Savage *et al.* 2002) sight lines suggest that C IV and Si IV trace each other well in the Galactic halo, while C IV and O VI exhibit large variations. The average $N(\text{C IV})/N(\text{O VI})$ ratio is ~ 0.6 throughout the entire halo with a decreasing dispersion toward larger z heights.

12. The O VI absorption does not correlate well with the known H I intermediate velocity clouds. We can identify known intermediate velocity features in the O VI absorption toward HDE 233622, but we see no correspondence toward BD+38 2182 and HD 121800. In the case of HD 121800, the component structure of the O VI absorption is drastically different from that of the low-ionization states.

13. Observations toward Galactic stars located in the general direction of $l = 355^\circ$ to 360° and $b = -16^\circ$ to -21° suggest that the large O VI columns observed by Savage *et al.* (2002) toward the region $l = 330^\circ$ to 36° and $b = -24^\circ$ to -33° are related to processes occurring near the Galactic center, and are not associated with the Loop I supernova remnant.

14. Savage *et al.* (2002) found that the general region in the sky toward $l = 80^\circ$ to 175° and $b = -30^\circ$ to -60° is deficient in O VI. Our observation toward HD 219188 in this direction reveals an O VI column similar to those of the nearby extragalactic sight lines. This suggests that the O VI may be confined to within 2 kpc of the Galactic mid-plane in this direction.

This work is based on data obtained for the Guaranteed Time Team by the NASA-CNES-CSA *FUSE* mission operated by the Johns Hopkins University. Financial support to U. S. participants has been provided by NASA contract NAS5-32985. KRS acknowledges support through NASA contract NAS5-32985 and Long Term Space Astrophysics grant NAG5-3485. We thank Ulrich Heber and Van Dixon for their permission to use their *FUSE* guest investigator data, and Alex Fullerton for providing the *FUSE* spectra processed by CALFUSE v1.8.7.

REFERENCES

- Alcaino, G. & Liller, W. 1980, *AJ*, 85, 680
- Begelman, M. C. & Fabian, A. C. 1990, *MNRAS*, 244, 26P
- Berkhuijsen, E. M. 1973, *A&A*, 24, 143
- Bohlin, R. C., Smith, A. M., Stecher, T. P., Sweigart, A. V., Cornett, R. H., & Hill, J. K. 1983, *ApJ*, 267, L89
- Borkowski, K. J., Balbus, S. A., & Fristrom, C. C. 1990, *ApJ*, 355, 501
- Callaway, M. B., Savage, B. D., Benjamin, R. A., Haffner, L. M., & Tufte, S. L. 2000, *ApJ*, 532, 943
- Clemens, D. P. 1985, *ApJ*, 295, 422
- Cowie, L. L., Jenkins, E. B., Songaila, A., & York, D. G. 1979, *ApJ*, 232, 467
- Danforth, C. W., Howk, J. C., Fullerton, A. W., Blair, W. P., & Sembach, K. R. 2002, *ApJS*, 138, 81
- Danly, L., Albert, C. E., & Kuntz, K. D. 1993, *ApJ*, 416, L29
- Davidson, A. F. 1993, *Science*, 259, 327
- Dickens, R. J., Brodie, I. R., & Bingham, E. A. 1988, Rutherford Appleton Laboratory, RAL 88-04
- Fox, A. J., Savage, B. D., Sembach, K. R., Fabian, D., Richter, P., Meyer, D. M., Lauroesch, J., & Howk, J. C. 2002, *ApJ*, in press
- Harris, W.E. 1996, *AJ*, 112, 1487
- Hartmann, D. & Burton, W. B. 1997, “Atlas of Galactic Neutral Hydrogen”, Cambridge University Press
- Heber, U. & Kudritzki, R. P. 1986, *A&A*, 169, 244
- Hoopes, C. G., Sembach, K. R., Howk, J. C., Savage, B. D., & Fullerton, A. W. 2002, *ApJ*, 569, 233
- Howk, J. C., Sembach, K. R., & Savage, B. D. 2002a, *ApJ*, in press

- Howk, J. C., Sembach, K. R., Savage, B. D., Massa, D., Friedman, S. D., & Fullerton, A. W. 2002b, *ApJ*, 569, 214
- Howk, J. C., Savage, B. D., Sembach, K. R., & Hoopes, C. G. 2002c, *ApJ*, 572, 264
- Hurwitz, M., Appenzeller, I., Barnstedt, J., Bowyer, S., Dixon, W. V. D., Grewing, M., Kappelman, N., Kraemer, G., Krautter, J., Mandel, H. 1998, *ApJ*, 500, L61
- Hurwitz, M. & Bowyer, S. 1995, *ApJ*, 446, 812
- Ito M., & Ikeuchi, S. 1988, *PASJ*, 40, 403
- Jenkins, E. B. 1978a, *ApJ*, 219, 845
- Jenkins, E. B. 1978b, *ApJ*, 220, 107
- Jenkins, E. B. 1996, *ApJ*, 471, 292
- Jenkins, E. B. & Meloy, D. A. 1974, *ApJ*, 193, L121
- Jenkins, E. B., Oegerle, W. R., Gry, C., Vallerga, J., Sembach, K. R., Shelton, R. L., Ferlet, R., Vidal-Madjar, A., York, D. G., Linsky, J. L., Roth, K. C., Dupree, A. K., & Edelstein, J. 2000, *ApJ*, 538, L81
- Jenkins, E. B. *et al.* 2002, in preparation
- Levine, A., Rappaport, S., Doxsey, R., & Jernigan, G. 1976, *ApJ*, 205, 226
- Levine, A., Rappaport, S., Halpern, J., & Walter F. 1977, *ApJ*, 211, 215
- Menzies, J. 1974, *MNRAS*, 168, 177
- Mihalas, D. & Binney, J. 1981, *Galactic Astronomy*, (2d ed; San Francisco: Freeman), Ch. 6
- Moos, H. W., *et al.* 2000, *ApJ*, 538, L1
- Norman C. A. & Ikeuchi S. 1989, *ApJ*, 345, 372
- Pottasch, S. R., Wesselius, P. R., & Arnal, E. M. 1980, *ESA 2nd European IUE Conf.*
- Ryans, R. S. I., Keenan, F. P., Sembach, K. R., & Davies, R. D. 1997, *MNRAS*, 289, 83
- Sahnou, D., *et al.* 2000, *ApJ*, 538, L7
- Savage, B. D., & Massa, D. 1987, *ApJ*, 314, 380

- Savage, B. D., Meade, M. R., & Sembach, K. R. 2001a, ApJS, 136, 631
- Savage, B. D. & Sembach, K. R. 1991, ApJ, 379, 245
- Savage, B. D. & Sembach, K. R. 1994, ApJ, 434, 145
- Savage, B. D., Sembach, K. R., & Howk, J. C. 2001b, ApJ, 547, 907
- Savage, B. D., Sembach, K. R., Jenkins, E. B., Shull, J. M., York, D. G., Sonneborn, G., Moos, H. W., Friedman, S. D., Green, J. C., Oegerle, W. R., Blair, W. P., Kruk, J. W., Murphy, E. M. 2000, ApJ, 538, L27
- Savage, B. D., Sembach, K. R., & Lu, L. 1997, AJ, 113, 2158
- Savage, B. D., Sembach, K. R., Wakker, B. P., Richter, P., Meade, M., Jenkins, E. B., Shull, J. M., Moos, H. W., & Sonneborn, G. 2002, ApJ, in press
- Sembach, K. R., Howk, J. C., Savage, B. D., Shull, J. M., & Oegerle, W. R. 2001, ApJ, 561, 573
- Sembach, K. R., & Savage, B. D. 1992, ApJS, 83, 147
- Sembach, K. R., & Savage, B. D. 1994, ApJ, 431, 201
- Sembach, K. R., Savage, B. D., & Hurwitz, M. 1999, ApJ, 524, 98
- Sembach, K. R., Savage, B. D., & Tripp, T. M. 1997, ApJ, 480, 216
- Sembach, K. R., *et al.* 2000, ApJ, 538, L31
- Sembach, K. R., Wakker, B. P., Savage, B. D., Richter, P., Meade, M., Shull, J. M., Jenkins, E. B., Sonneborn, G., & Moos, H. W. 2002, ApJ, in press
- Shapiro, P. R., & Benjamin, R. A. 1991, PASP, 103, 923
- Shapiro, P. R., & Field, G. B. 1976, ApJ, 205, 762
- Shelton, R. L. 1998, ApJ, 504, 785
- Shelton, R. L., & Cox, D. P. 1994, ApJ, 434, 599
- Shull, J. M., & Slavin, J. D. 1994, ApJ, 427, 784
- Slavin, J. D., & Cox, D. P. 1992, ApJ, 392, 131
- Slavin, J. D., & Cox, D. P. 1993, ApJ, 417, 187

- Slavin, J. D., Shull, J. M., & Begelman, M. C. 1993, *ApJ*, 407, 83
- Snowden, S. L., Egger, R., Finkbeiner, D. P., Freyberg, M. J., & Plucinsky, P. P. 1998, *ApJ*, 493, 715
- Sofia, U. J., & Jenkins, E. B. 1998, *ApJ*, 499, 951
- Spitzer, L. 1956, *ApJ*, 124, 20
- Spitzer, L. 1996, *ApJ*, 458, L29
- Sterling, N. C., Savage, B. D., Richter, P., Fabian, D., & Sembach, K. R. 2002, *ApJ*, 567, 354
- Sutherland, R. S., & Dopita, M. A. 1993, *ApJS*, 88, 253
- Thompson, R. W., Turnrose, B. E., & Bohlin, R. C. 1982, *A&A*, 107, 11
- Wakker, B. P. 2001, *ApJS*, 136, 463
- Wakker, B. P., Savage, B. D., Sembach, K. R., Richter, P., Meade, M., Jenkins, E. B., Shull, J. M., Ake, T. B., Blair, W. P., Dixon, W. V., Friedman, S. D., Green, J. C., Green, R. F., Kruk, J. W., Moos, H. W., Murphy, E. M., Oegerle, W. R., Sahnou, D. J., Sonneborn, G., Wilkinson, E., & York, D. G. 2002, *ApJ*, in press
- Widmann, H., de Boer, K. S., Richter, P., Kramer, G., Appenzeller, I., Barnstedt, J., Golz, M., Grewing, M., Gringel, W., Mandel, H., Werner, K. 1998, *A&A*, 338, L1
- York, D. G. 1974, *ApJ*, 193, L127
- York, D. G. 1977, *ApJ*, 213, 43

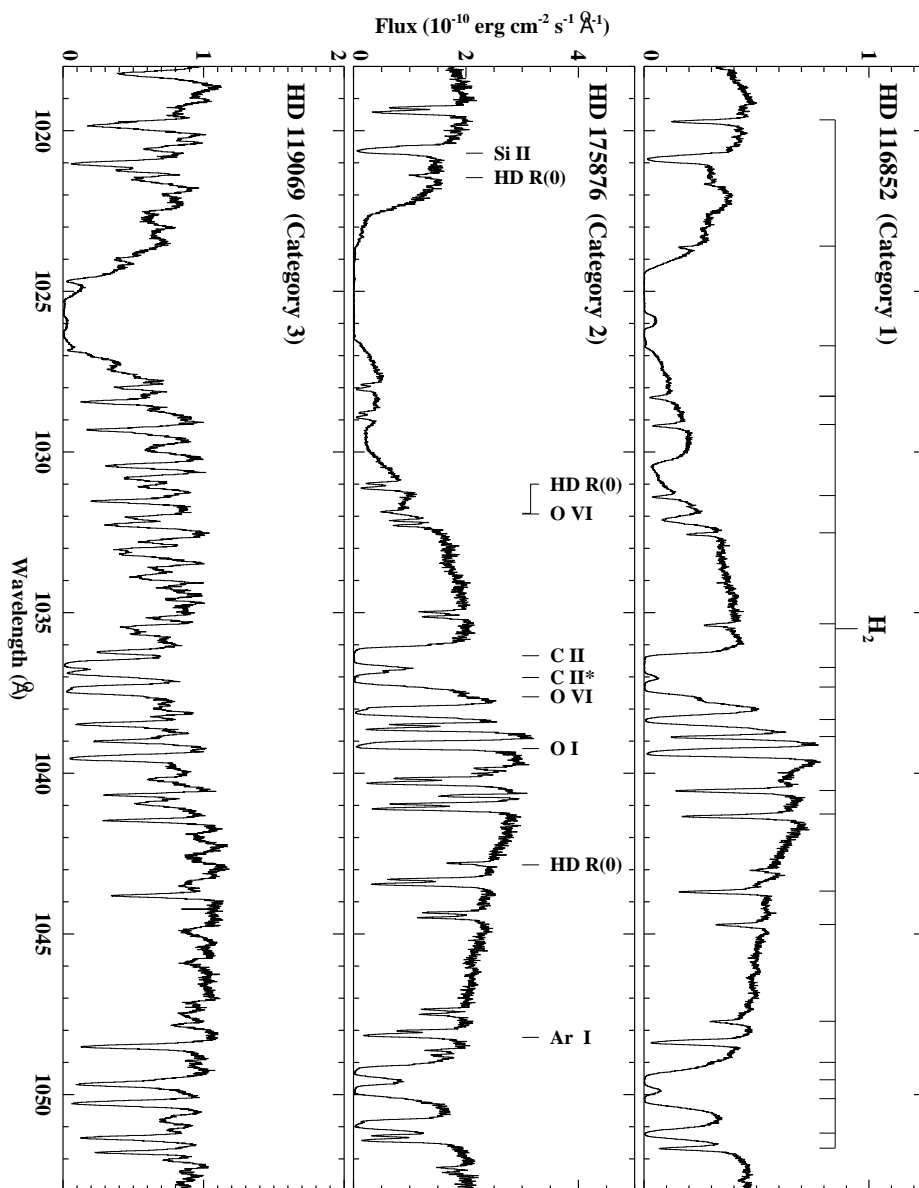


Fig. 1.— Flux versus wavelength over the spectral range 1018-1053 \AA . The prominent H₂ lines are marked in the upper panel while O VI $\lambda\lambda$ 1031.93, 1037.62 and various other atomic transitions are labelled in the middle panel. O VI can be studied in the spectra of Category 1 objects (e.g., HD 116852) but the analysis becomes more difficult and impossible for objects in Category 2 (e.g., HD 175876) and Category 3 (e.g., HD 119069), respectively.

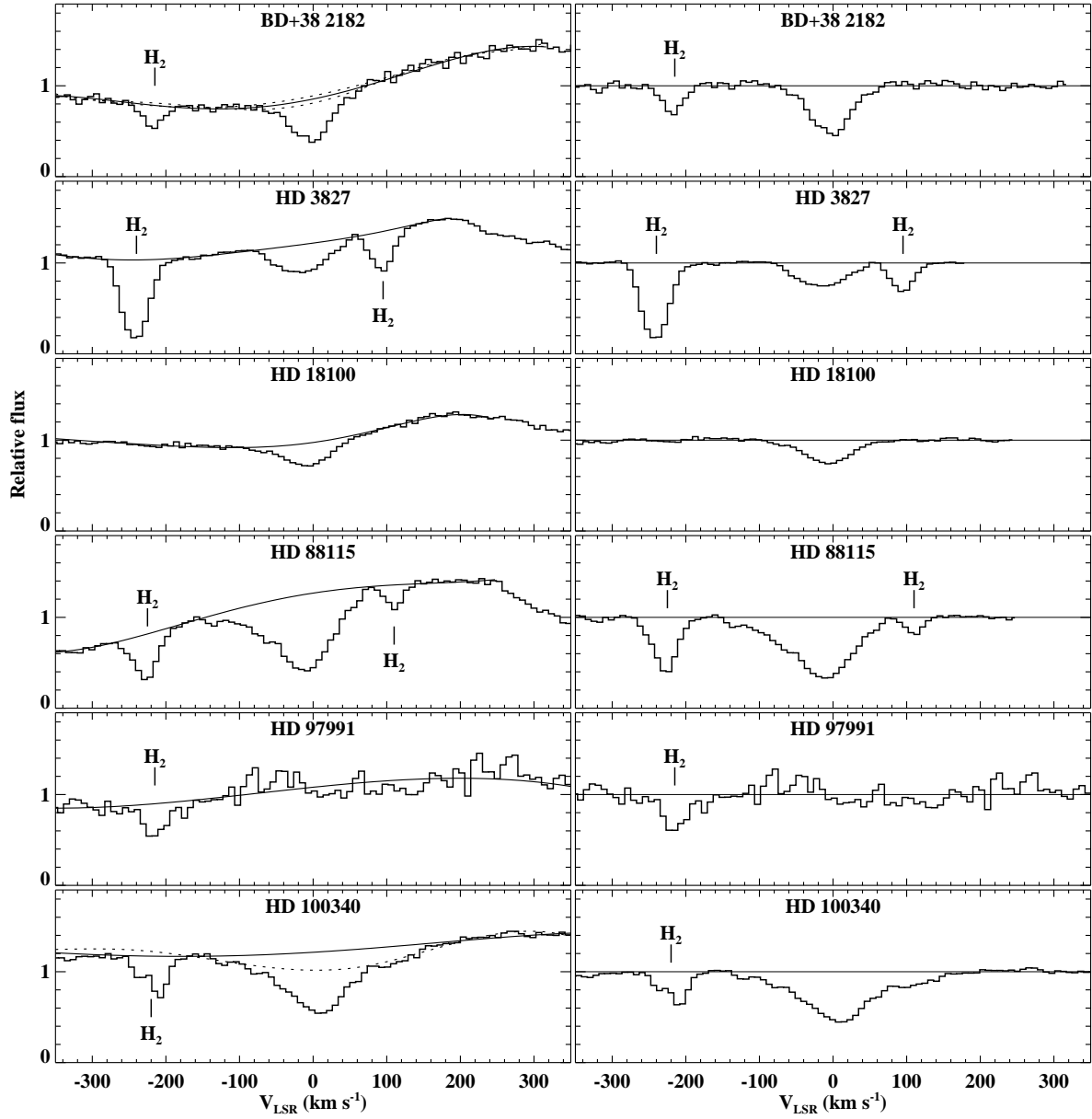


Fig. 2.—

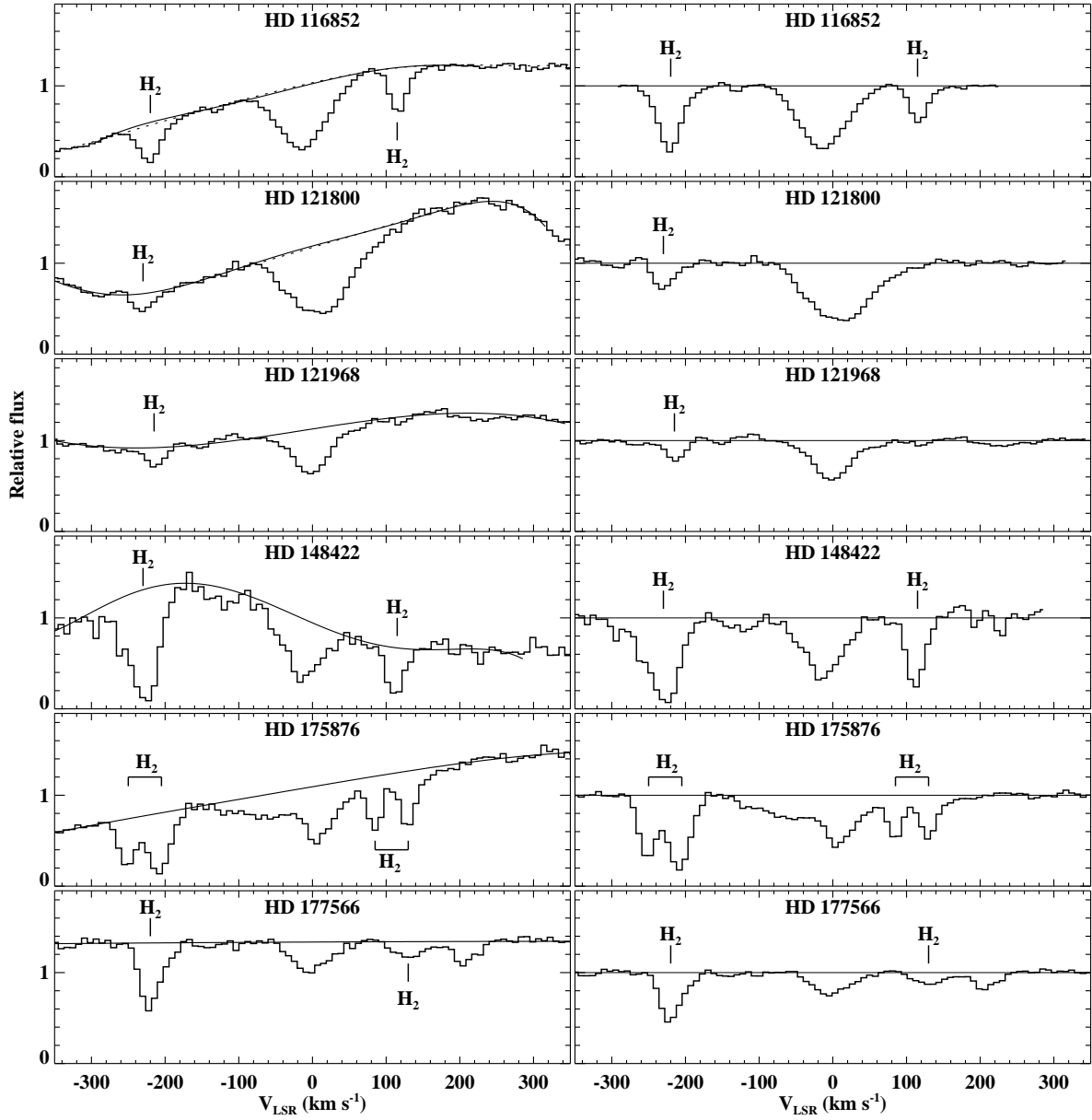


Fig. 2.—

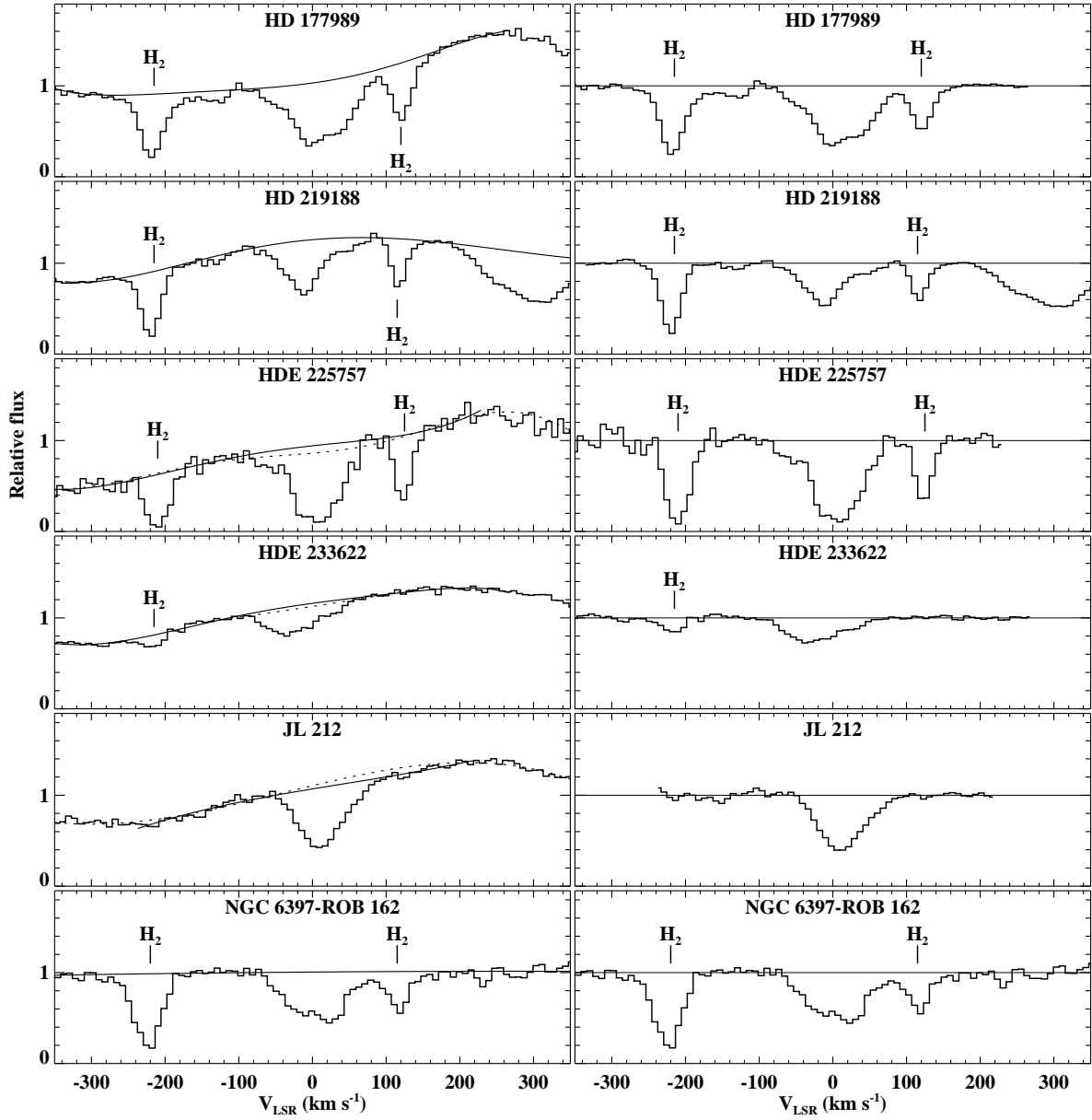


Fig. 2.—

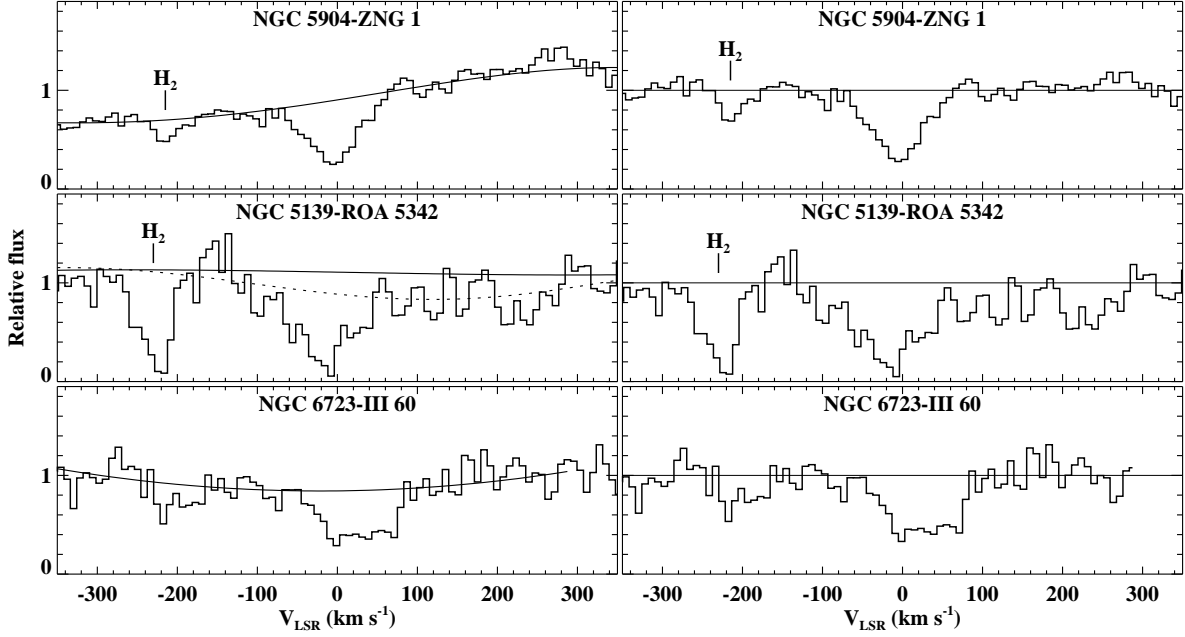


Fig. 2.— The relative flux around the O VI 1031.93 Å line toward the sight lines listed in Table 1. Left: The observed relative fluxes plotted against the LSR velocity. The continua are overplotted by thin lines. If alternative continuum placements were considered, then they are shown by dotted lines. Right: The resulting normalized spectra as a function of LSR velocity. We marked the position of the H₂ *P*(3) 1031.19 Å and *R*(4) 1032.35 Å lines if they were present.

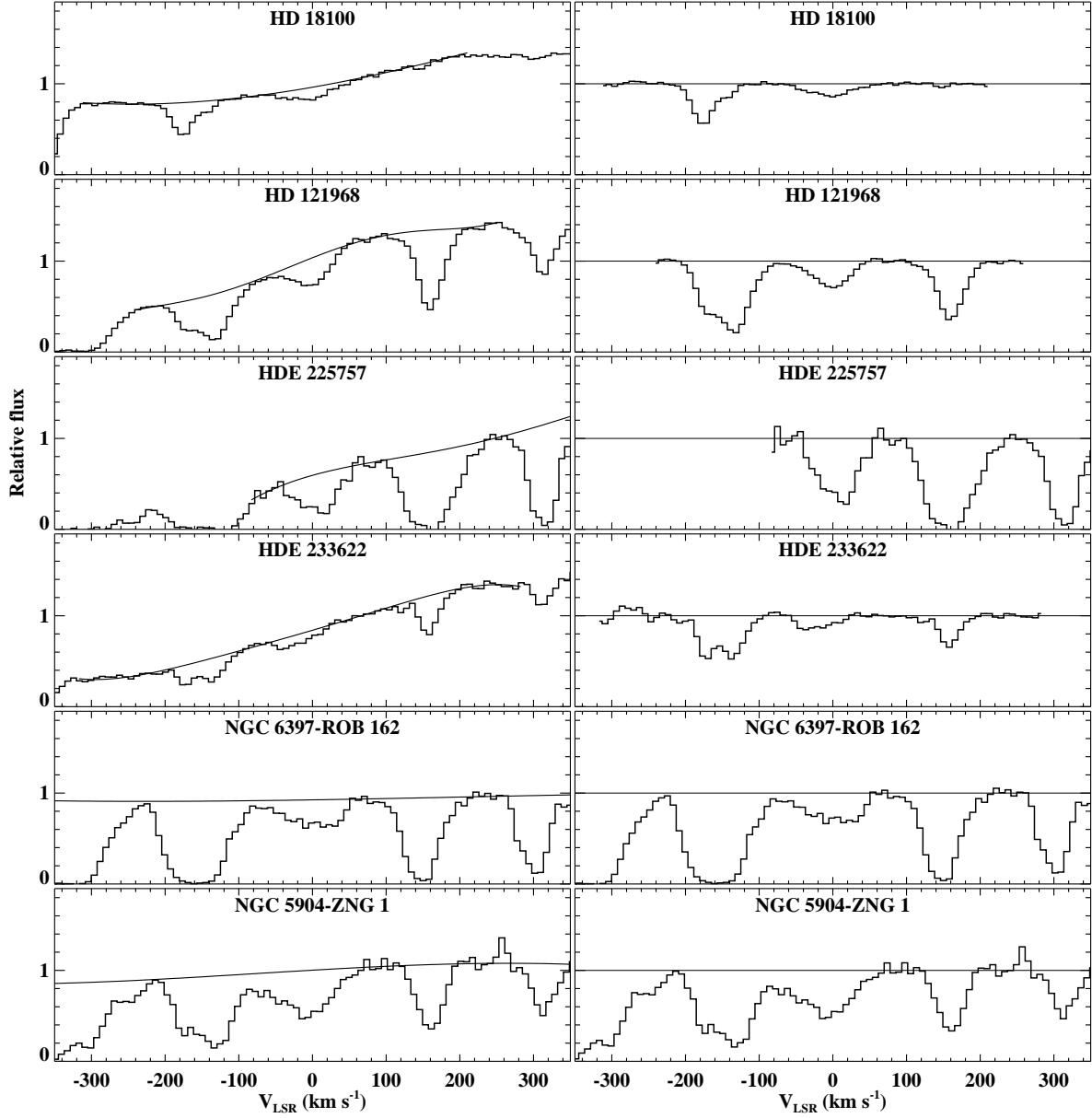


Fig. 3.— Same as Figure 2, but for O VI $\lambda 1037.62$ toward our sight lines. Only 6 of the 22 profiles are shown. Severe interstellar and stellar blending makes measurements of the O VI $\lambda 1037.62$ absorption uncertain for the remaining 16 cases.

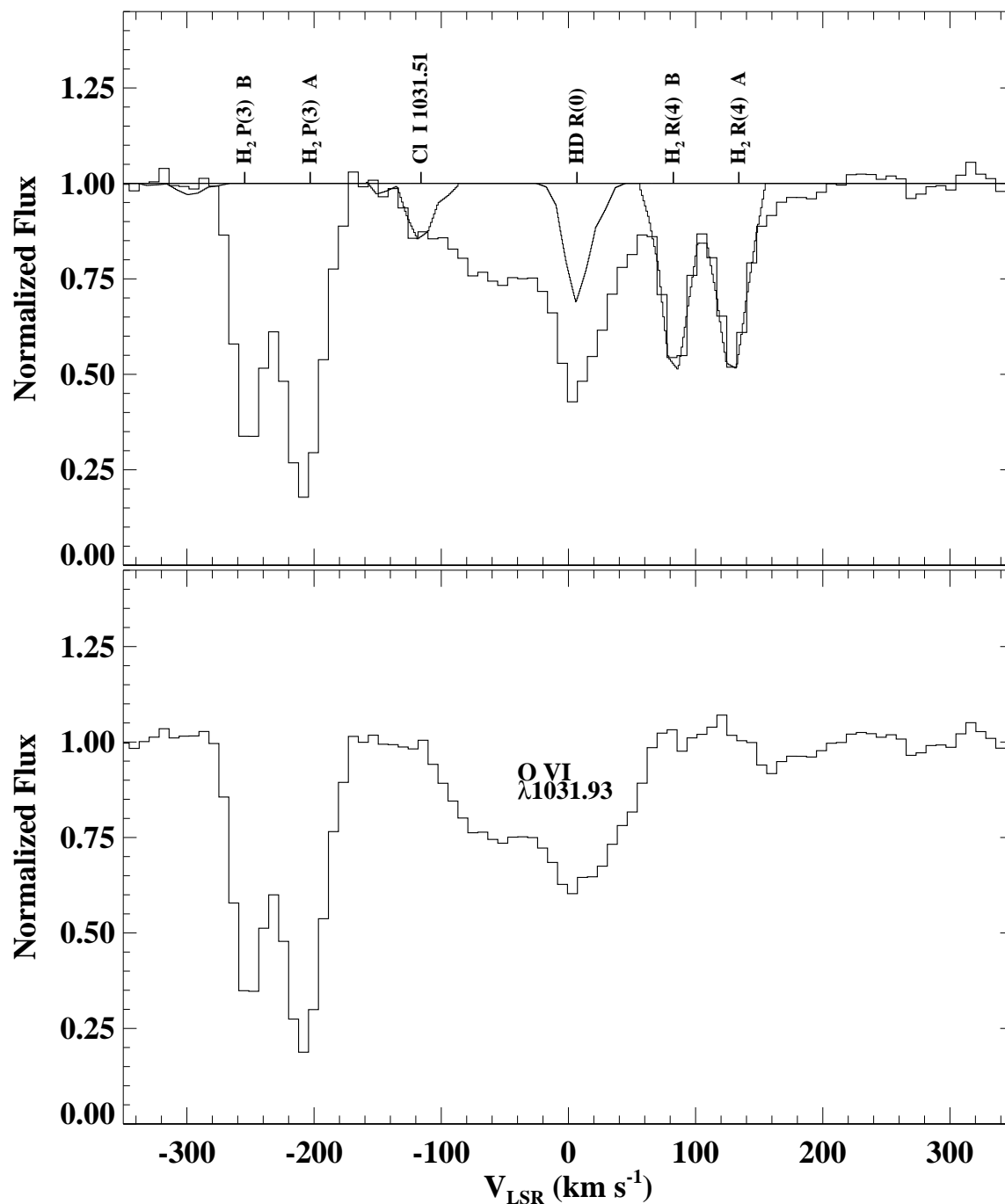


Fig. 4.— The complex system of blended lines around O VI $\lambda 1031.93$ toward HD 175876. The spectra are plotted against LSR velocity. The normalized spectrum is shown with a thick solid line (histogram) in the upper panel, and the calculated Cl I, HD, and H_2 profiles are overplotted with thin lines. The final spectrum cleared of HD, Cl I, and H_2 contributions is plotted in the lower panel. There are two components in the H_2 absorption: component A, which is also visible in Cl I and HD absorption, and component B, which is shifted by $\sim -50 \text{ km s}^{-1}$ with respect to component A.

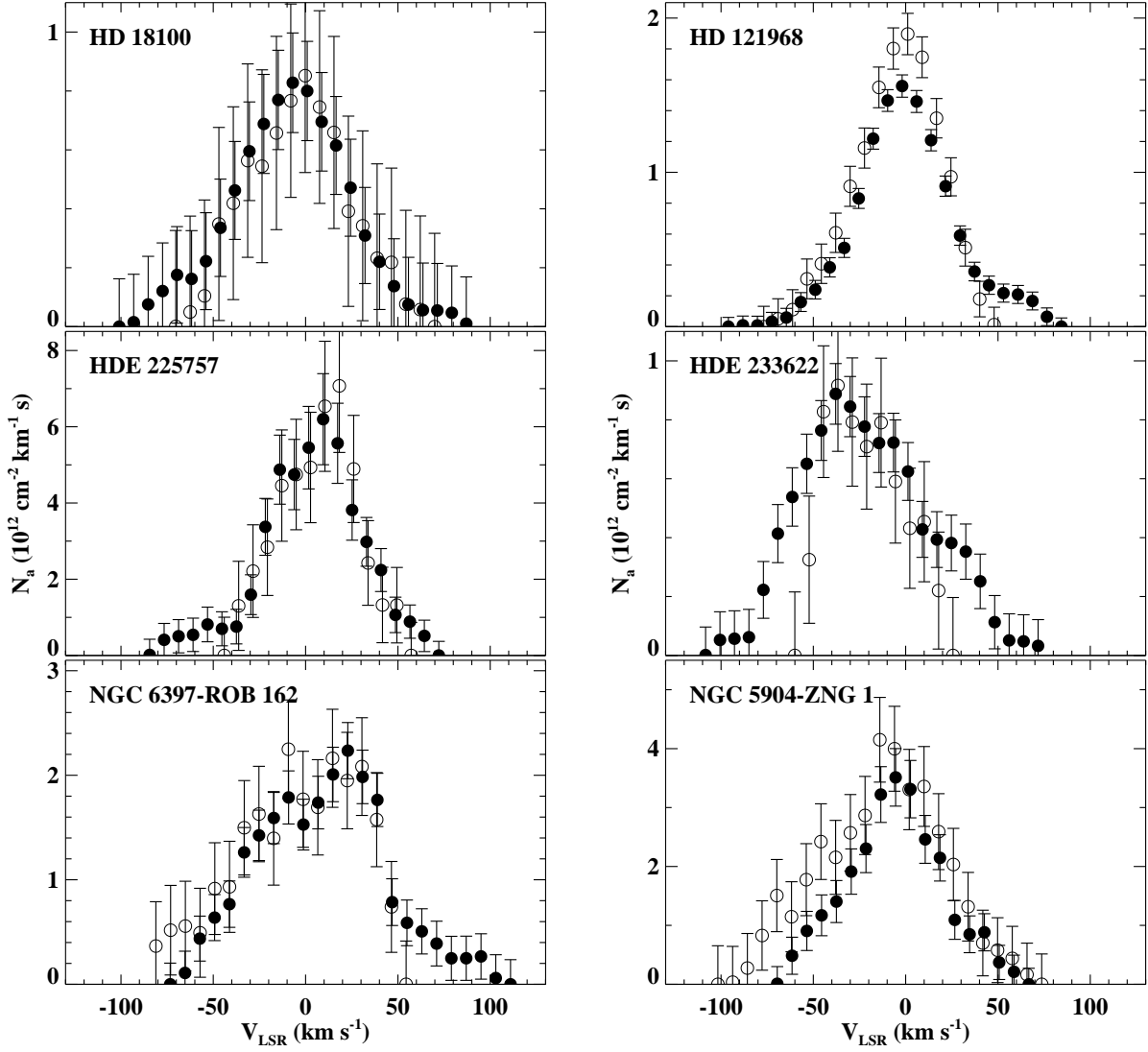


Fig. 5.— The apparent column density profiles of O VI $\lambda 1031.93$ (closed circles) and $\lambda 1037.62$ (open circles) toward the 6 sight lines for which both were extracted. The error bars reflect only the statistical uncertainties. The profiles do not reveal significant saturation effects at $|V_{\text{LSR}}| \leq 50 \text{ km s}^{-1}$, except in the case of HD 121968 where a modest $\sim 20\%$ saturation may be present. There are differences at $|V_{\text{LSR}}|$ greater than $\sim 50 \text{ km s}^{-1}$ where strong C II, C II*, and H₂ absorption limited our ability to find accurate stellar continua around the O VI 1037.62 Å lines.

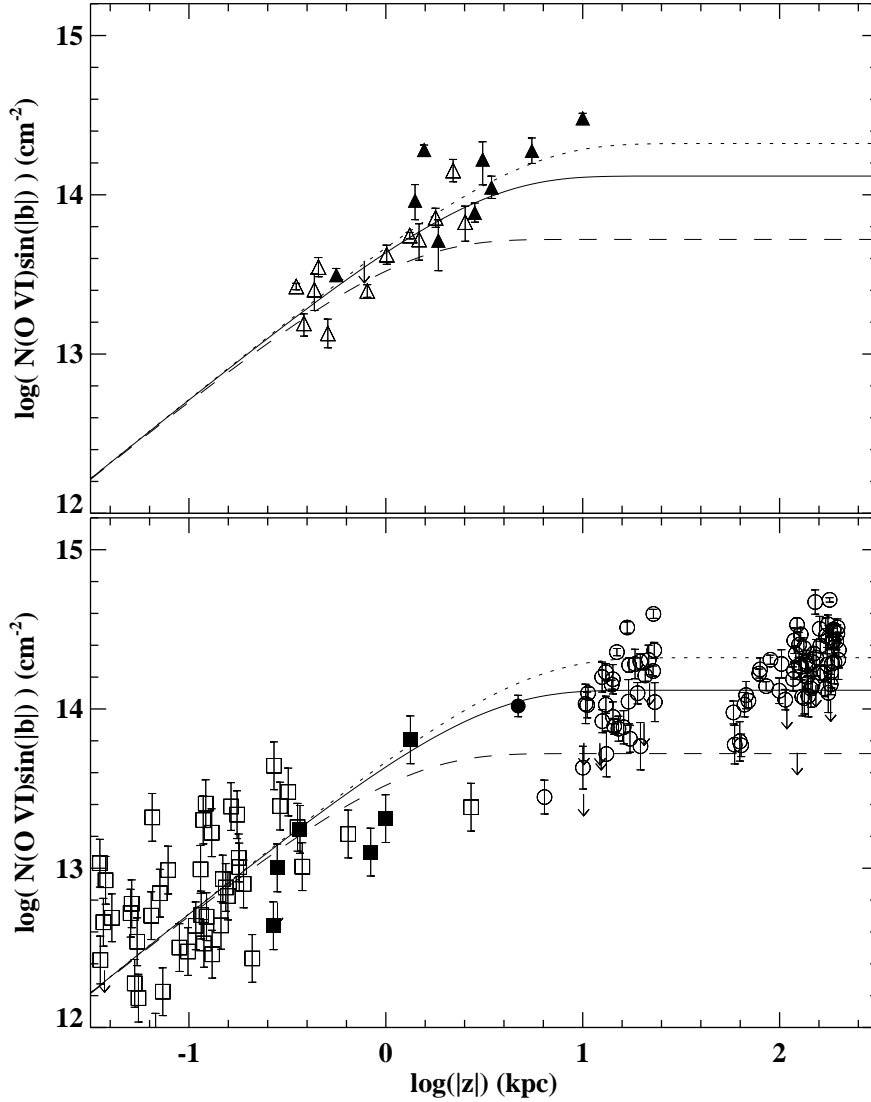


Fig. 6.— The total O VI columns perpendicular to the Galactic plane as a function of vertical distance from the plane (z), plotted on a log-log scale. The panels are identical apart from the datasets plotted. Triangles, circles, and squares are measurements from the present analysis, Savage *et al.* (2002), and Jenkins (1978a), respectively. Downward-pointing arrows indicate upper limits. We display Galactic measurements (disk and halo) with solid symbols if their Galactic latitude and $|z|$ were greater than zero and 0.25 kpc, respectively. The measurements toward extragalactic targets with $b \geq 0^\circ$ are artificially shifted by +1 dex in $\log|z|$ with respect to those with $b < 0^\circ$. The north-south asymmetry, observed by Savage *et al.* (2002), is well illustrated by the different values of $\langle N\sin|b| \rangle$ for the southern ($\log|z| \sim 1.2$) and northern ($\log|z| \sim 2.2$) extragalactic sight lines. The distributions calculated by Equation 5 using a mid-plane density of $n_0 = 1.7 \times 10^{-8} \text{ cm}^{-3}$ and scale heights $h(\text{O VI}) = 2.5 \text{ kpc}$ (solid line), $h(\text{O VI}) = 1 \text{ kpc}$ (dashed line), and 4 kpc (dotted line) are also plotted.

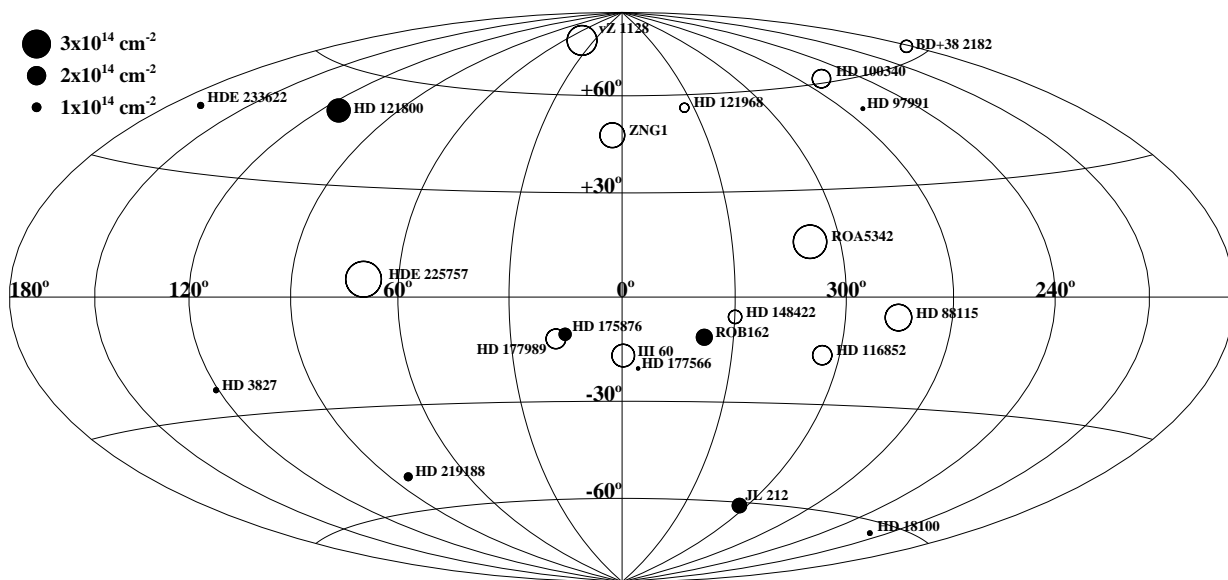


Fig. 7.— Total O VI column densities toward our sight lines, displayed in a Hammer-Aitoff projection. The Galactic Center is in the middle of the Figure and Galactic longitude increases to the left. The diameter of each circle is linearly proportional to the value of the column density, and the scaling is displayed in the upper left corner. The upper limit toward HD 97991 was treated as an observation. Open and closed symbols represent measurements for stars with $d > 3$ kpc and $d \leq 3$ kpc, respectively. The name of each object is printed beside its location. NGC 6397-ROB 162, NGC 5904-ZNG 1, NGC 5139-ROA 5342, and NGC 6723-III 60 were shortened to ROB 162, ZNG 1, ROA 5342, and III 60, respectively.

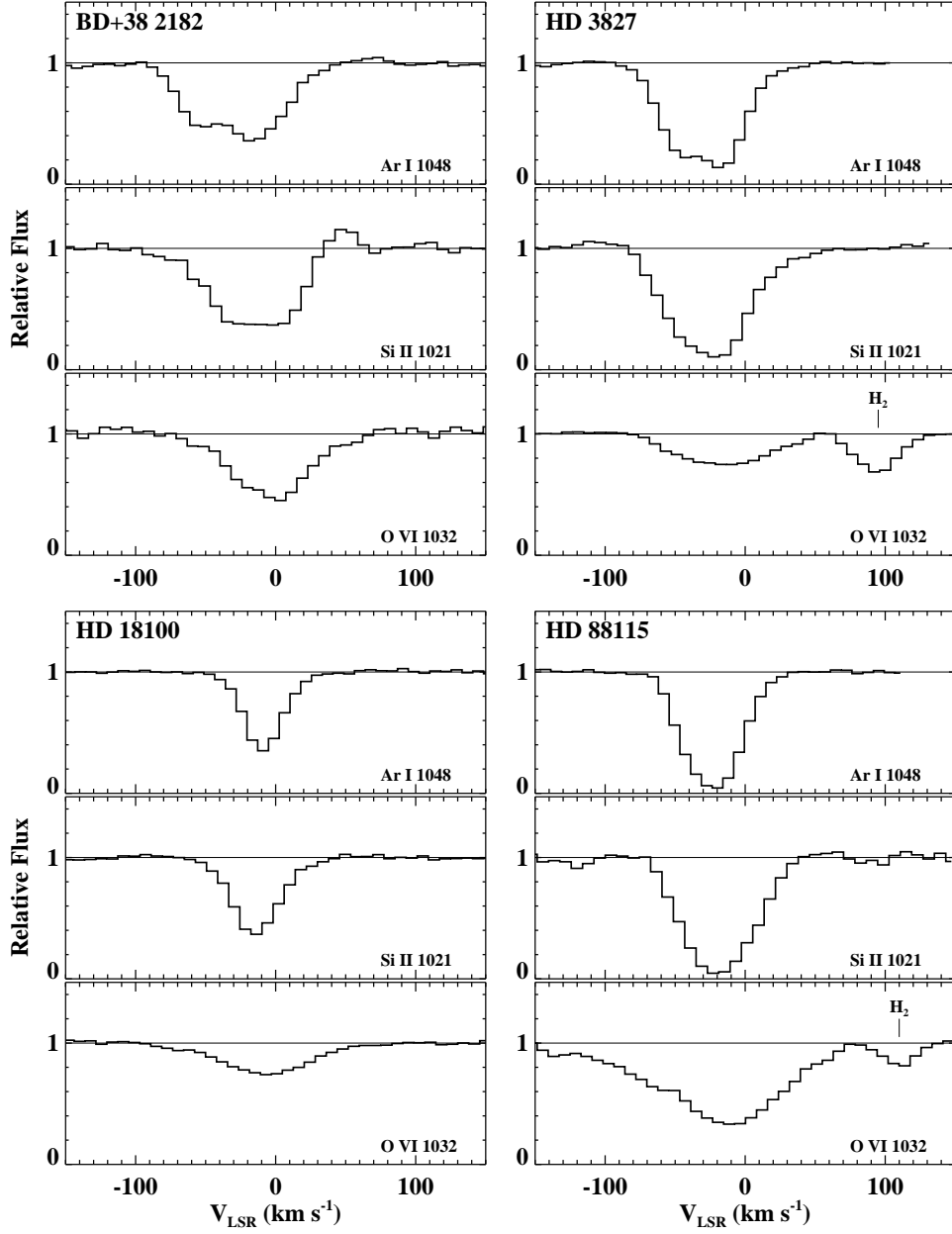


Fig. 8.—

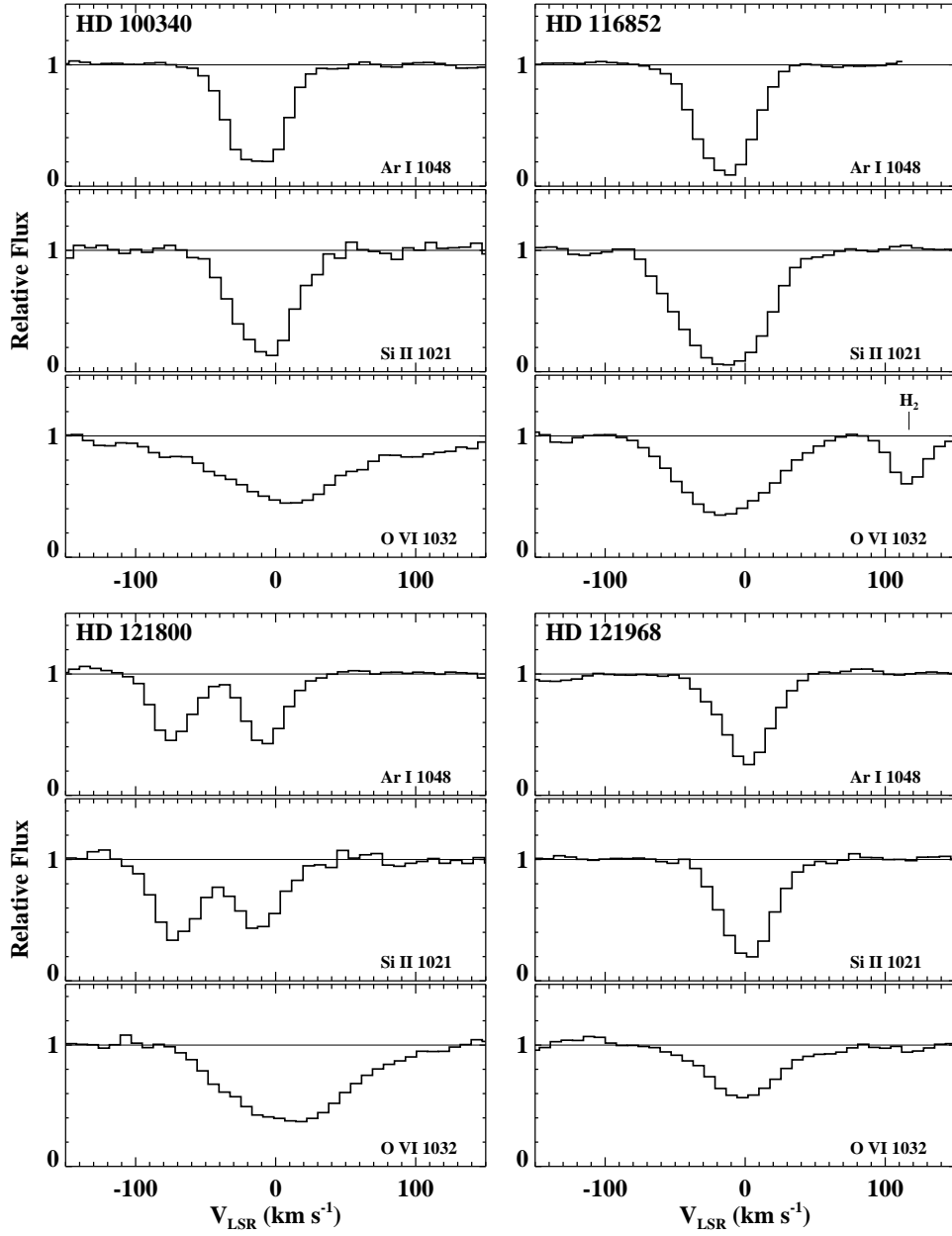


Fig. 8.—

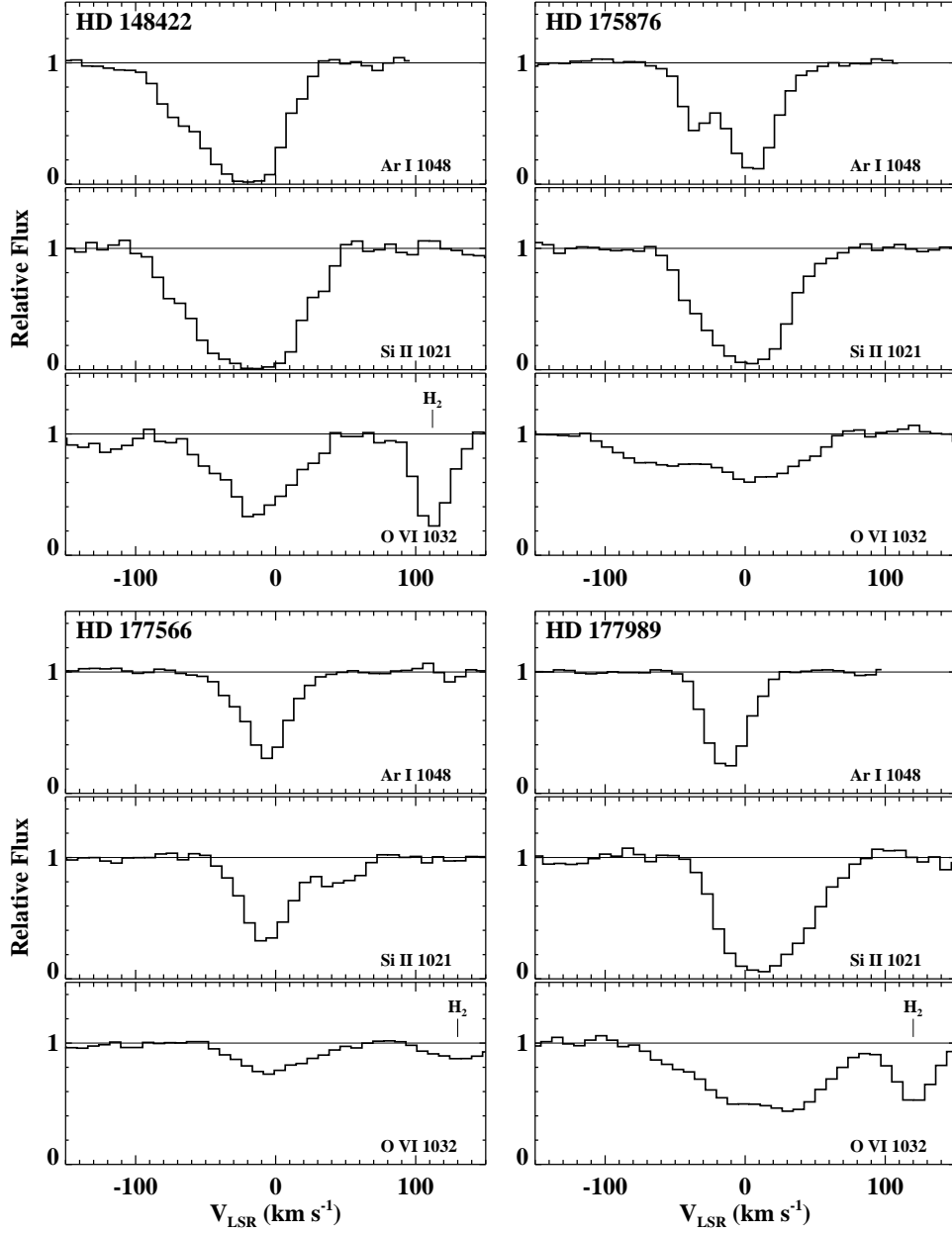


Fig. 8.—

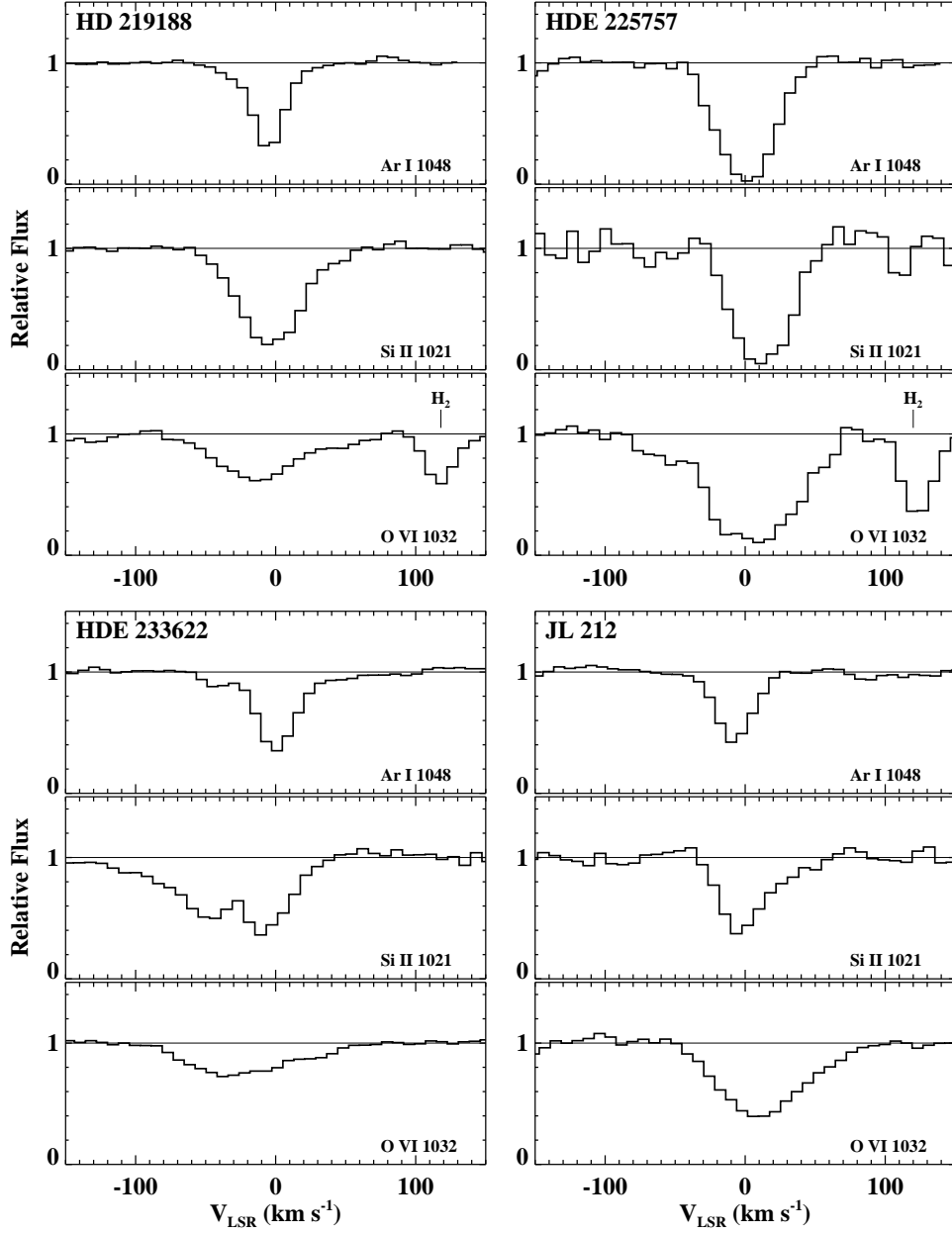


Fig. 8.—

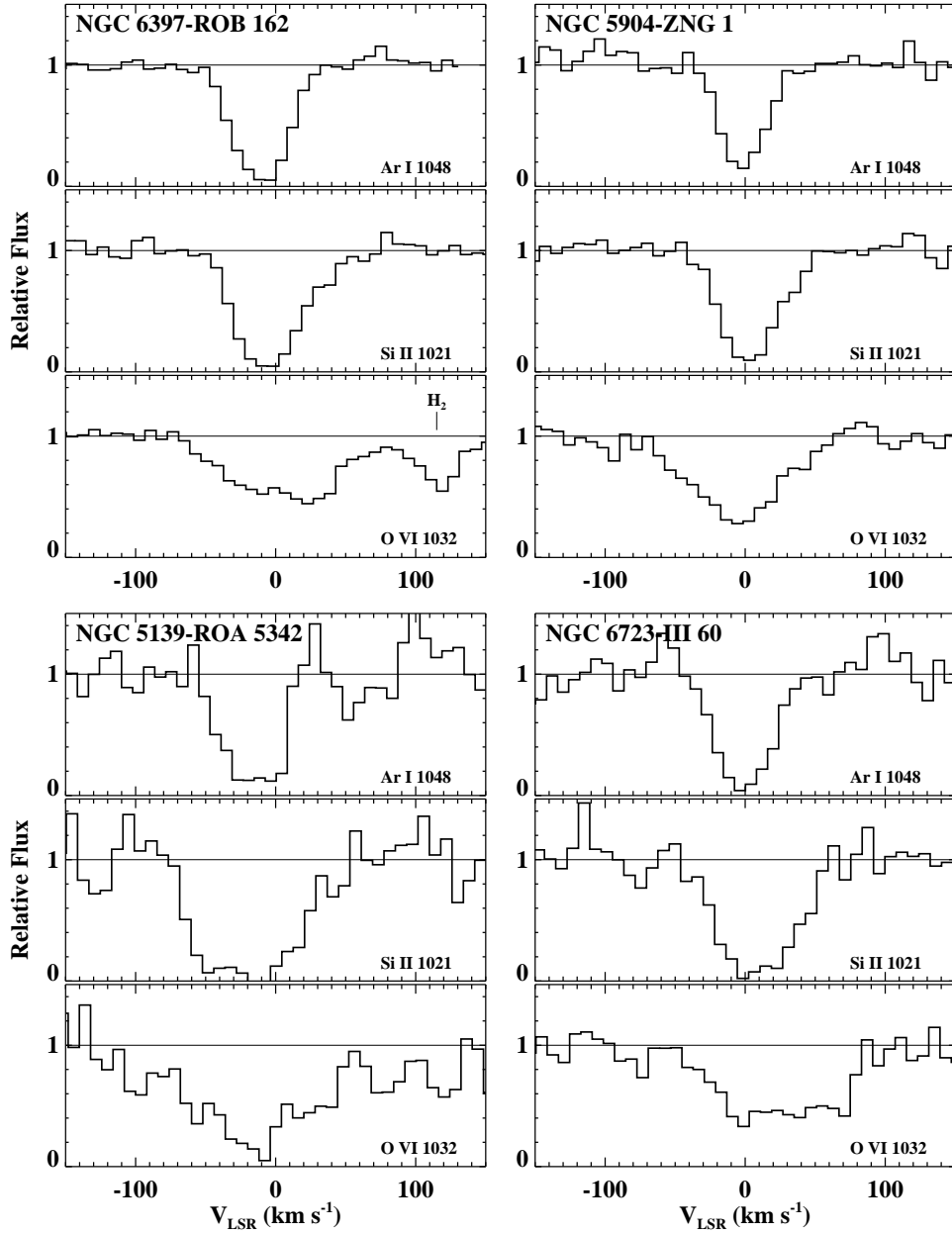


Fig. 8.— The comparison of low-ionization states (Ar I λ 1048.22 and Si II λ 1020.70) with the O VI absorption at 1031.93 Å toward the halo star sight lines. We label the position of the H₂ R(4)_{6–0} line if it is clearly present. A velocity correction of +10 km s^{−1} was applied for the profiles of Ar I λ 1048.22 in the cases of LWRS observations (see Table 3) to account for the systematic calibration errors present in the *FUSE* spectra reduced by CALFUSE v1.8.7 (see §3).

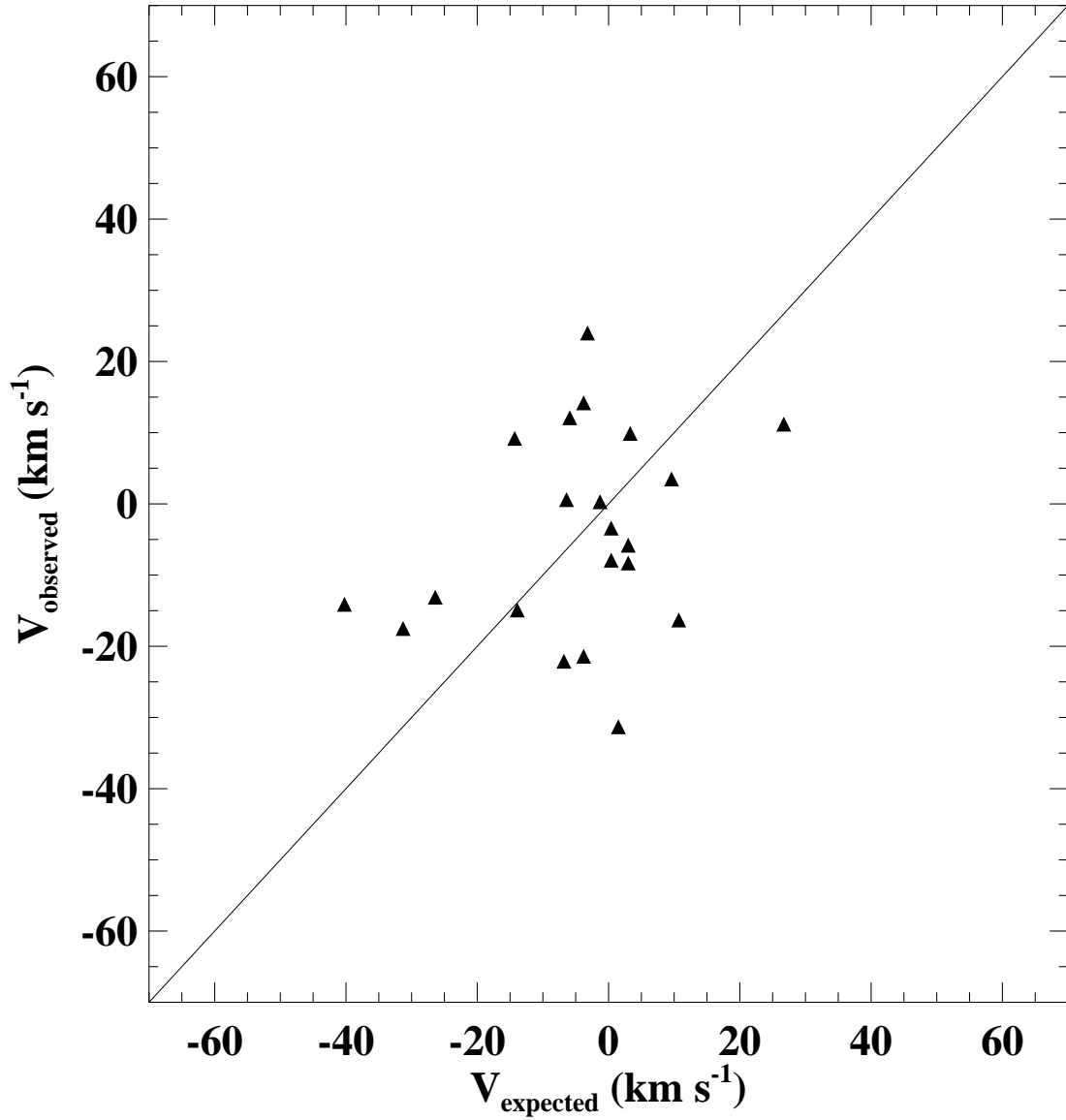


Fig. 9.— The measured O VI line centroid velocities plotted against the velocities expected from the Galactic rotation assuming co-rotation of disk and halo gas and the Clemens (1985) Galactic rotation curve. The solid line represents a 1:1 correlation between the two quantities. HD 97991 was omitted, because only an upper limit for the O VI column was measured.

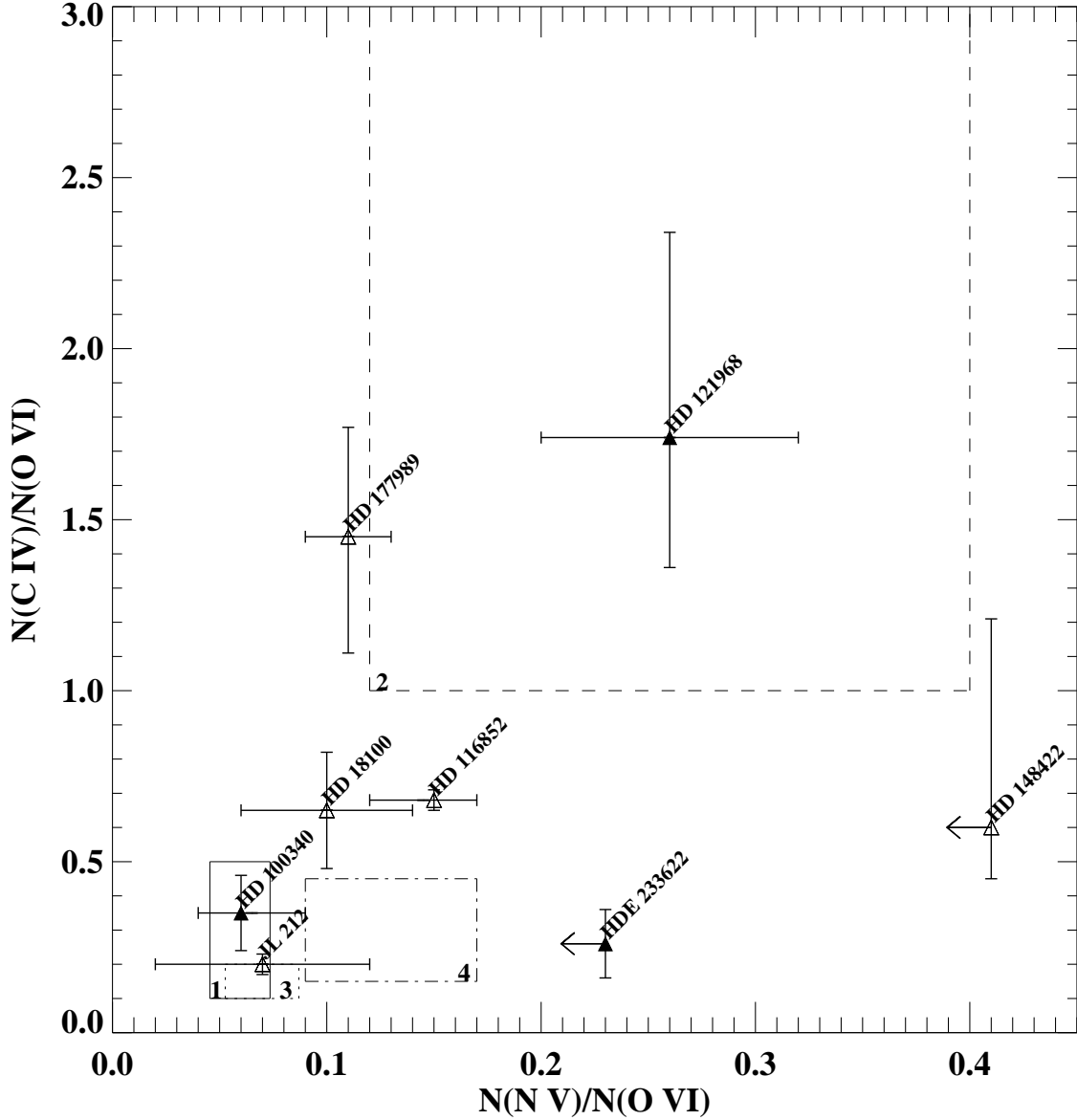


Fig. 10.— The $N(C\ IV)/N(O\ VI)$ ratios plotted against the $N(N\ V)/N(O\ VI)$ ratios. Lower and upper limits are shown by arrows pointing in the appropriate directions. Sight lines with $b \geq 0^\circ$ and $b < 0^\circ$ are displayed by solid and open symbols, respectively. The values that are predicted by a model for high ion production are within the corresponding rectangle in the figure. We displayed the predictions of the following models: 1: (CGF) cooling Galactic fountain model R. Benjamin (2002, private communication), solid lines; 2: (TML) turbulent mixing layer model of Slavin *et al.* (1993), dashed lines; 3: (SNR) cooling supernova remnant model of Slavin & Cox (1992), dotted lines; 4: (CI) thermal conduction model of Borkowski *et al.* (1990), dash-dotted lines.

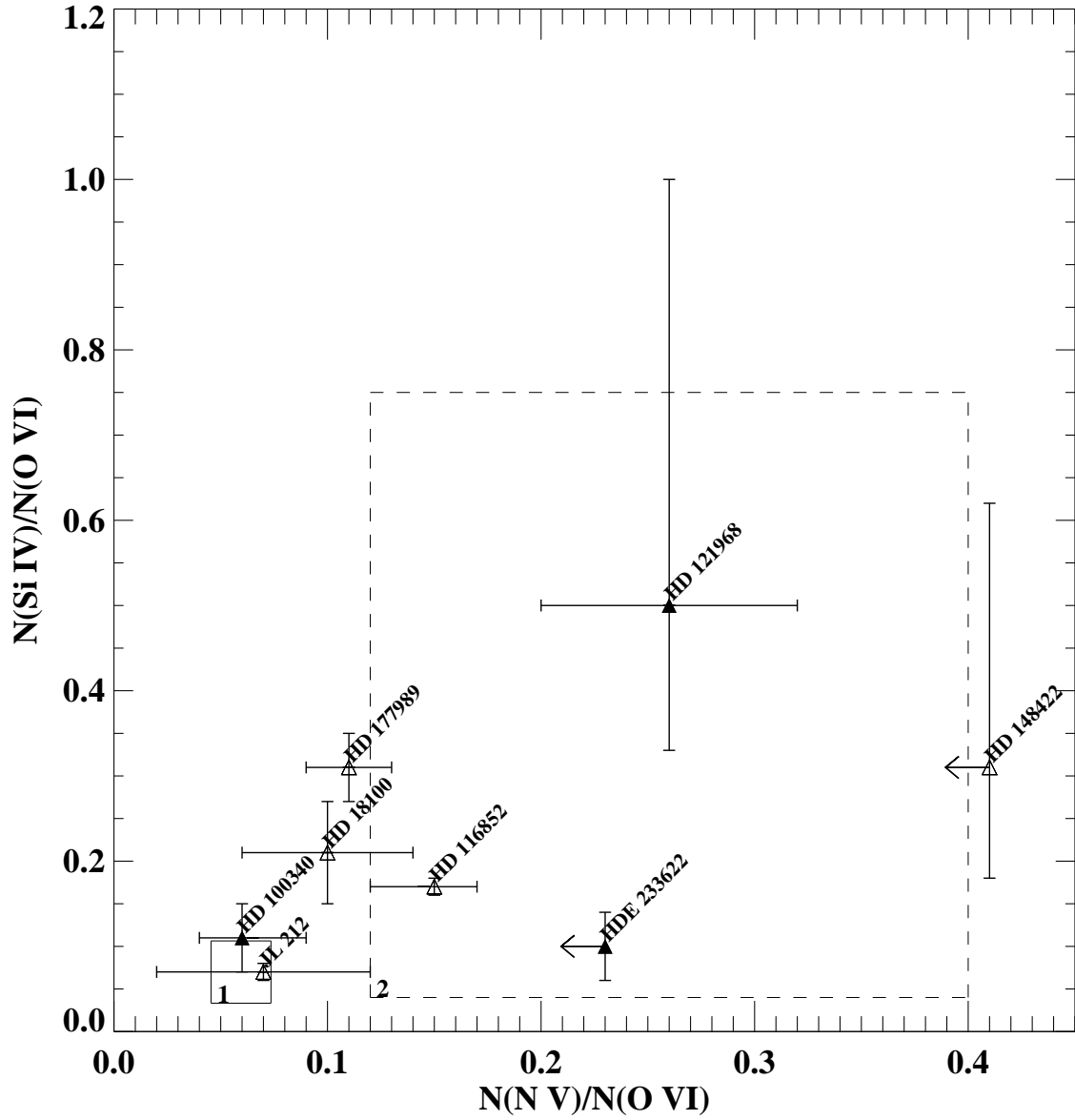


Fig. 11.— Same as Figure 10, but for $N(\text{Si IV})/N(\text{O VI})$ as a function of $N(\text{N V})/N(\text{O VI})$. The predictions of the SNR and CI models for the $N(\text{Si IV})/N(\text{O VI})$ ratios are too low to display.

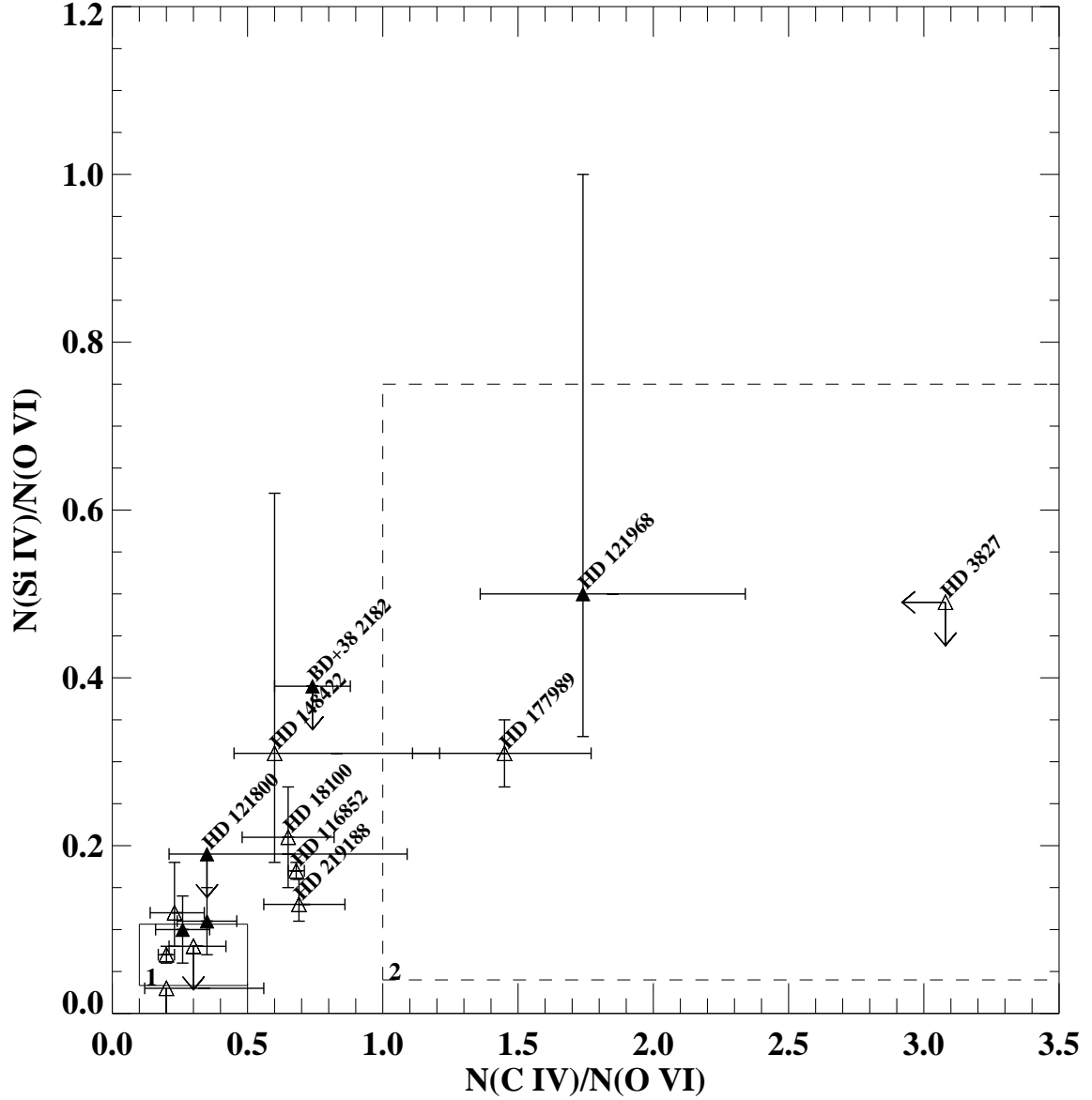


Fig. 12.— Same as Figure 10, but for $N(\text{Si IV})/N(\text{O VI})$ as a function of $N(\text{C IV})/N(\text{O VI})$. The predictions of the SNR and CI models for the $N(\text{Si IV})/N(\text{O VI})$ ratios are too low to display. We did not label sight lines with $N(\text{Si IV})/N(\text{O VI}) \leq 0.15$ and $N(\text{C IV})/N(\text{O VI}) \leq 0.5$ for clarity.

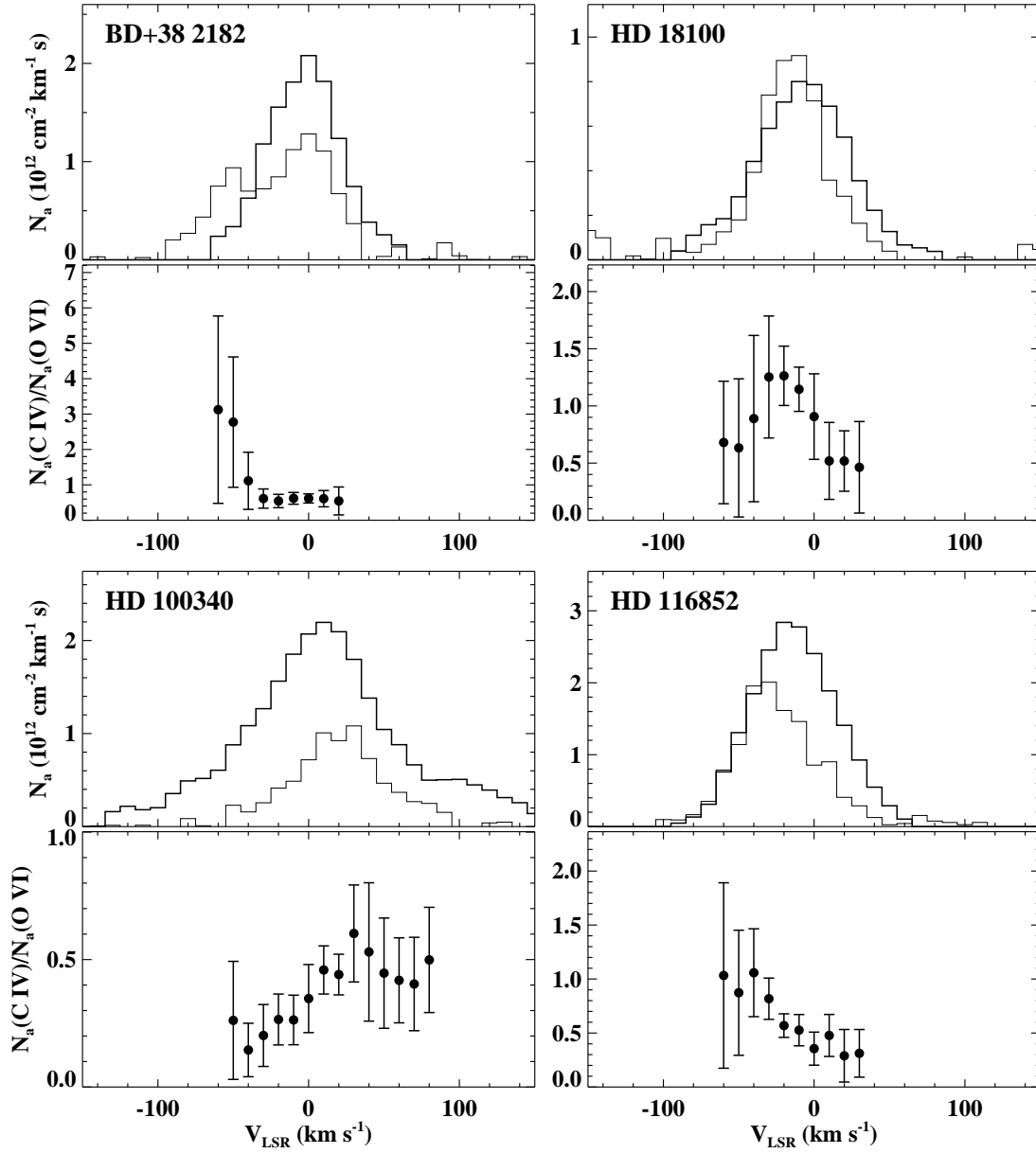


Fig. 13.—

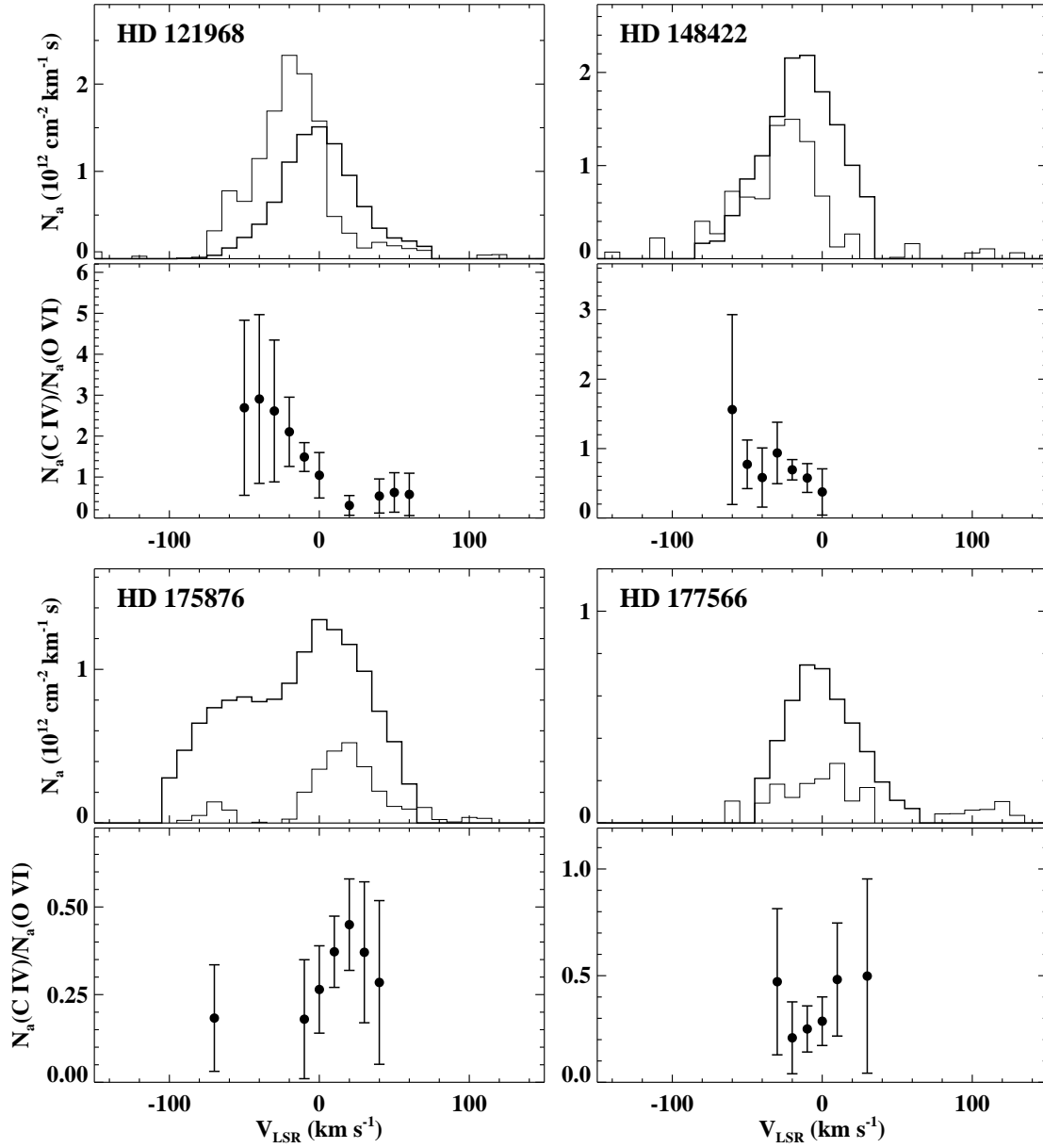


Fig. 13.—

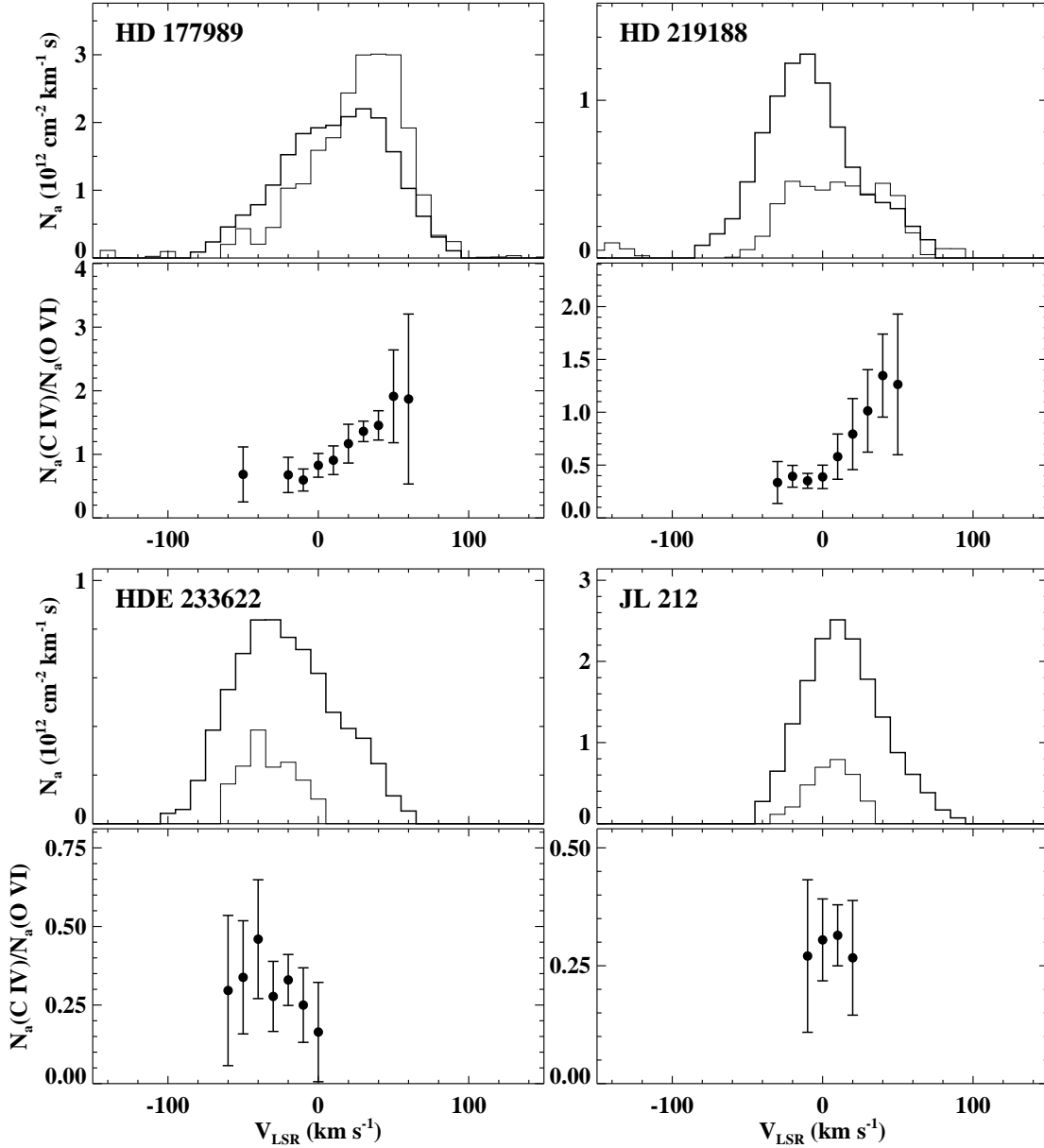


Fig. 13.— Upper panels: Apparent column density profiles of O VI $\lambda 1031.93$ (thick line) and C IV $\lambda 1548.20$ (thin lines) toward sight lines with observed C IV absorption. The C IV $\lambda 1548.20$ profiles are from Savage *et al.* (2001a), except for HDE 233622 and JL 212, which were extracted from STIS archival spectra. We rebinned both profiles to 10 km s^{-1} velocity bins. Lower panels: The C IV to O VI ratio as a function of LSR velocity. The ratios are based on the $N_a(v)$ profiles displayed in the upper panel. The error bars reflect the statistical errors and the uncertainties in the LSR velocity zero-point. The ratios are plotted only if their uncertainties do not exceed the ratio.

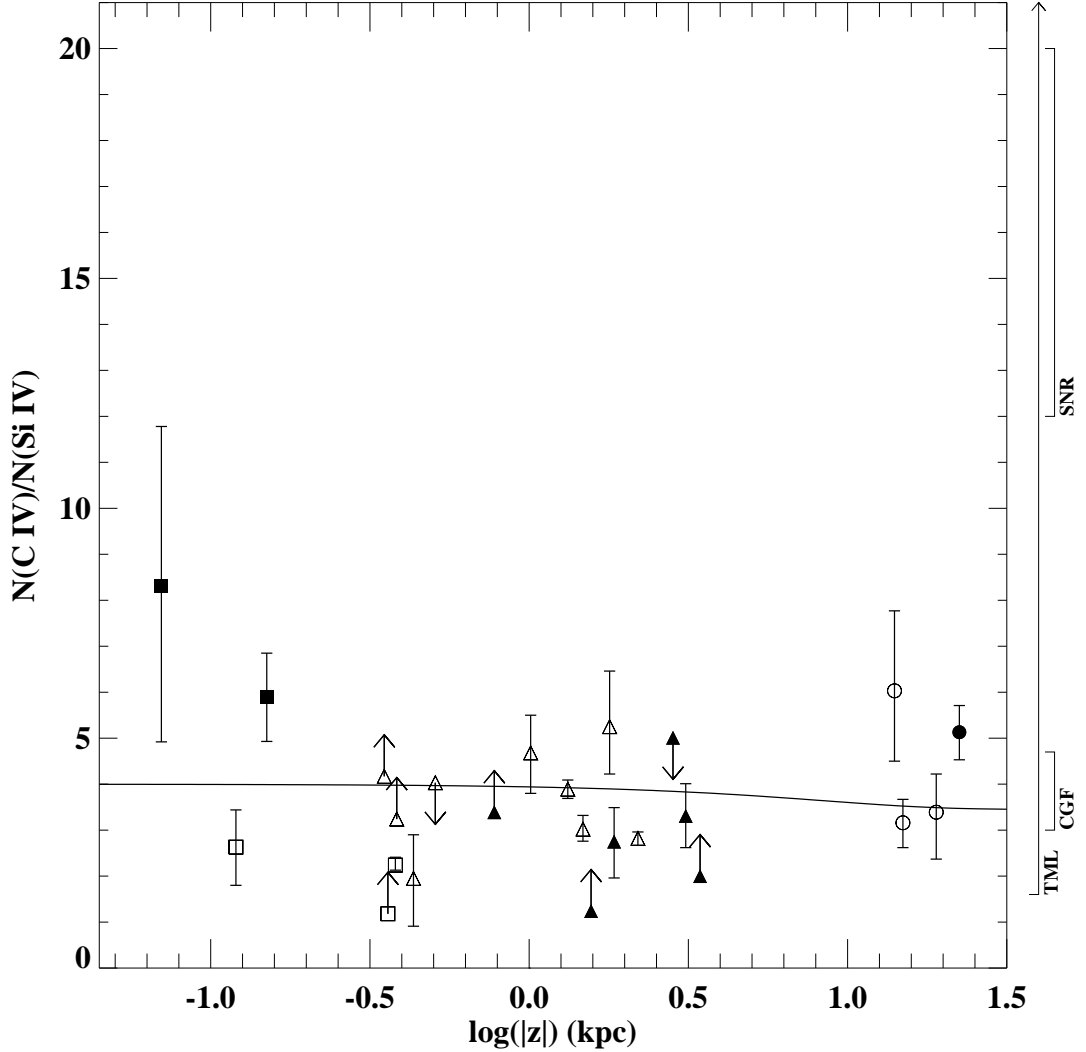


Fig. 14.— The $N(\text{C IV})/N(\text{Si IV})$ ratios as a function of distance from the Galactic plane. Triangles indicate our measurements, while the ratios toward extragalactic targets (Savage *et al.* 2002; Hoopes *et al.* 2002) are shown by circles. We also display the ratios toward the six stars from the disk sample of Spitzer (1996) as squares. Lower and upper limits are indicated by the appropriate arrows. Sight lines with $b < 0^\circ$ and $b \geq 0^\circ$ are shown with open and solid symbols, respectively. The predicted $N(\text{C IV})/N(\text{Si IV})$ ratios, assuming simple exponential distributions, are plotted by a solid line (see §6.2). The ion ratios allowed by the various theories of high ion production are indicated on the right-hand side of the figure. The values and the references for the theoretical predictions are the same as those for Figure 10. References for the Si IV and C IV column densities for disk and extragalactic sight lines can be found in Spitzer (1996), Savage *et al.* (2002), and Savage *et al.* (1997).

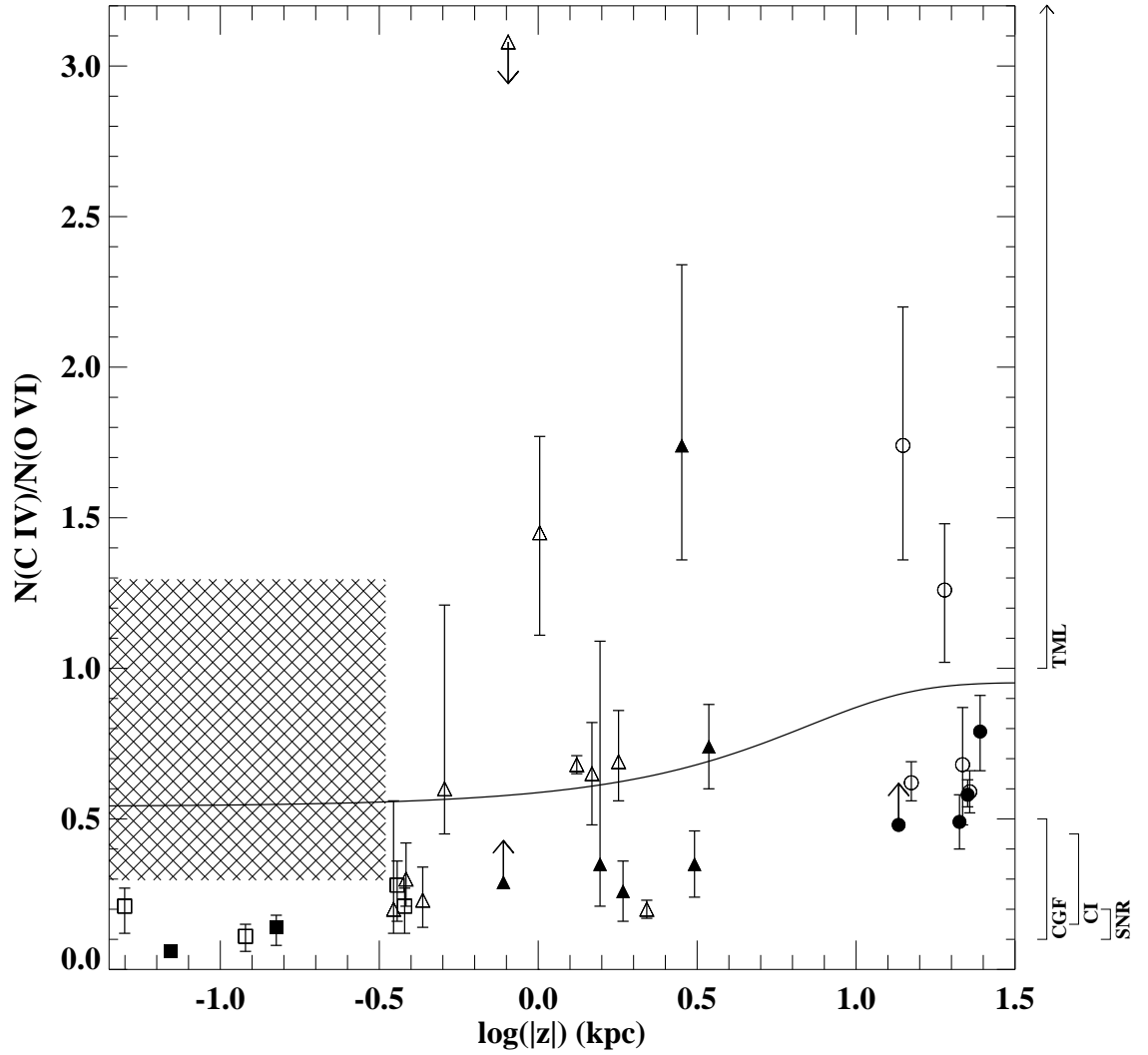


Fig. 15.— Same as Figure 14 for $N(\text{C IV})/N(\text{O VI})$. The cross-hatched region at $\log(|z|) \leq -0.5$ indicates the $\pm 1\sigma$ range of $N(\text{C IV})/N(\text{O VI})$ in the disk survey of E. Jenkins (2002, private communication).

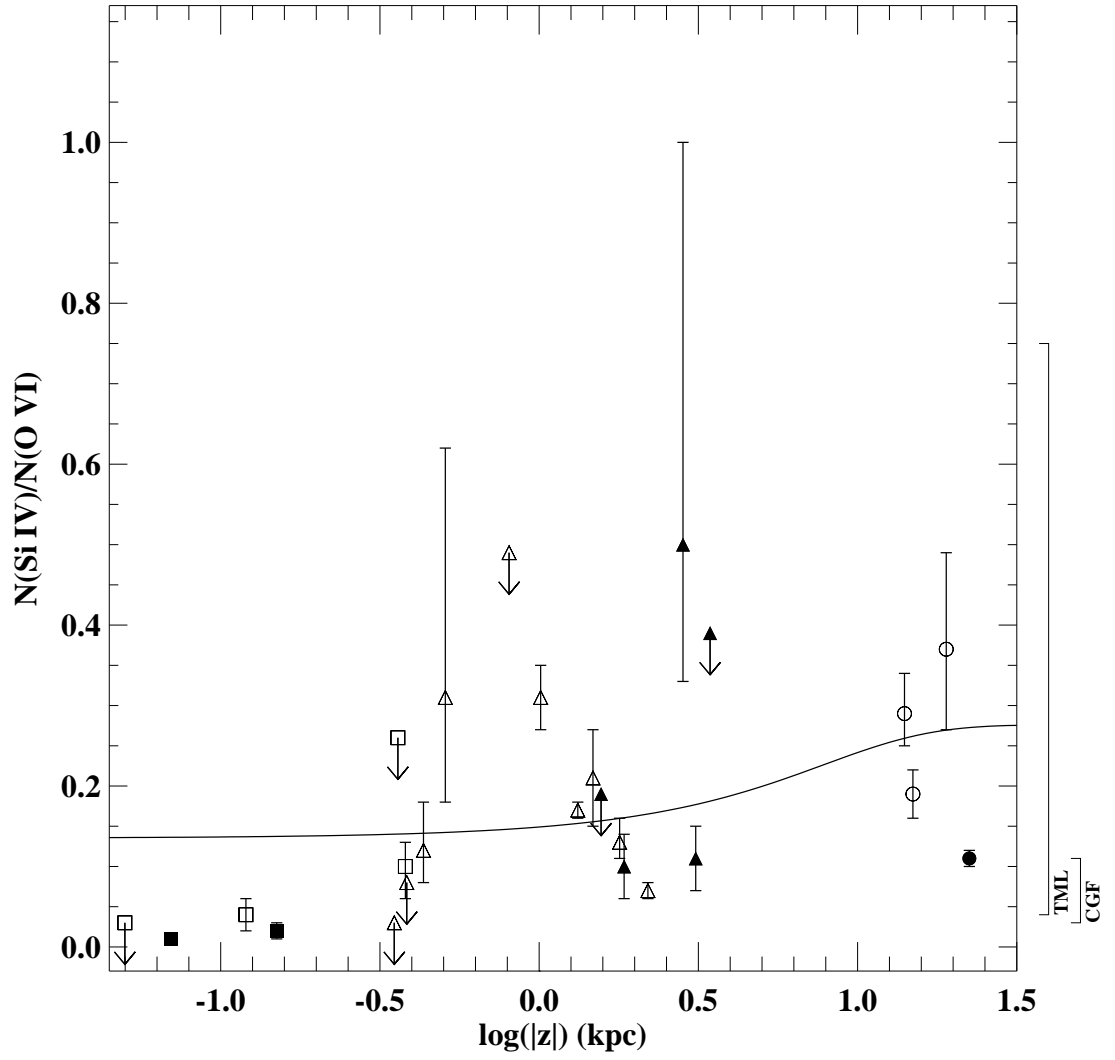


Fig. 16.— Same as Figure 14 for $N(\text{Si IV})/N(\text{O VI})$.

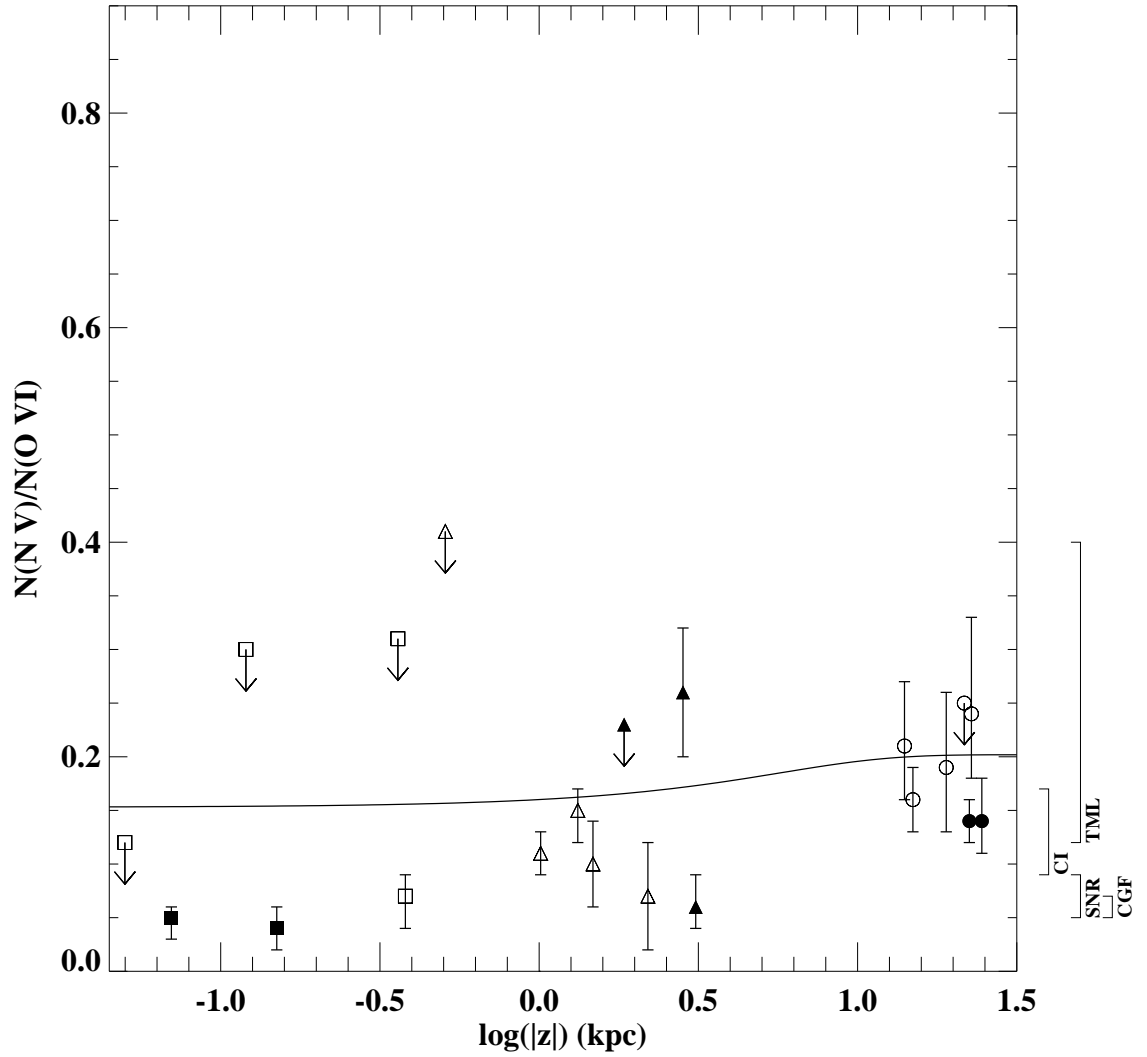


Fig. 17.— Same as Figure 14 for $N(\text{N V})/N(\text{O VI})$. References for the N V column densities for the disk and extragalactic sight lines can be found in Spitzer (1996), Savage *et al.* (2002), and Savage *et al.* (1997).

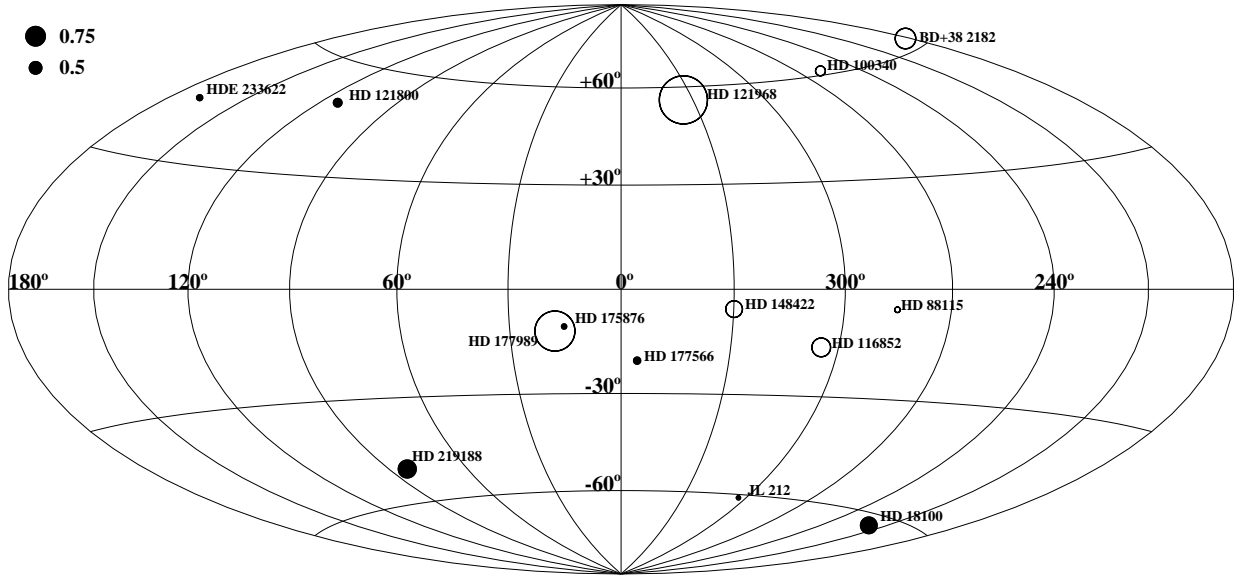


Fig. 18.— The $N(\text{C IV})/N(\text{O VI})$ ratios toward our sight lines, displayed in a Hammer-Aitoff projection. The Galactic Center is in the middle of the Figure and Galactic longitude increases to the left. The diameter of each circle is linearly proportional to the value of the ratio, and the scaling is displayed in the upper left corner. Open and closed symbols represent measurements for stars with $d > 3$ kpc and $d \leq 3$ kpc, respectively. The name of each object is printed beside its location. NGC 6397-ROB 162, NGC 5904-ZNG 1, NGC 5139-ROA 5342, and NGC 6723-III 60 were shortened to ROB 162, ZNG 1, ROA 5342, and III 60, respectively.

Table 1. Target Stars.

Star ID	Spectral type	$v \sin(i)$ km s ⁻¹	V (mag)	E(B-V)	l (°)	b (°)	d (pc)	z (pc)
BD+38 2182	B3V	...	11.25	0.00	182.16	+62.21	3890	3441
HD 3827	B0.7V	125	8.01	0.02	120.79	-23.23	2040	-804
HD 18100	B1V	265	8.46	0.02	217.93	-62.73	1660	-1476
HD 88115	B1.5IIIn	245	8.30	0.16	285.32	-5.53	3640	-351
HD 97991	B1V	...	7.41	0.04	262.34	+51.73	990	777
HD 100340	B1V	275	10.11	0.02	258.85	+61.23	3540	3103
HD 116852	O9III	136	8.47	0.22	304.88	-16.13	4760	-1322
HD 121800	B1.5V	121	9.11	0.08	113.01	+49.76	2050	1565
HD 121968	B1V	160	10.25	0.09	333.97	+55.84	3420	2830
HD 148422	B1Ia	81	8.60	0.28	329.92	-5.60	5200	-507
HD 175876	O6.5IIIIn	266	6.95	0.22	15.28	-10.58	2360	-433
HD 177566	PAGB	...	10.20	0.07	355.55	-20.42	1100	-384
HD 177989	B0III	150	9.33	0.25	17.81	-11.88	4910	-1011
HD 219188	B0.5II-I	197	7.05	0.14	83.03	-50.17	2330	-1789
HDE 225757	B1IIIIn	...	10.59	0.22	69.64	+4.85	6630	560
HDE 233622	B2V	240	10.01	0.03	168.17	+44.23	2650	1849
JL 212	B2	219	10.20	0.13	303.63	-61.03	2510	-2196
NGC 6397-ROB 162	PAGB	...	13.23	0.20	337.90	-11.40	2300	-500
NGC 5904-ZNG 1	PAGB	...	14.20	0.03	3.49	+47.40	7500	5500
NGC 5139-ROA 5342	PAGB	...	15.89	0.12	308.45	+15.40	5300	1400
NGC 6723-III 60	PAGB	...	15.61	0.05	359.69	-16.70	8800	-2600
vZ 1128	PAGB	...	15.03	0.01	42.50	+78.68	10200	10000

Original sources for the listed quantities can be found in Savage & Sembach (1994) and Sembach & Savage (1992). The visual magnitudes of the PAGB-s (except vZ1128) are from Alcaïno & Liller (1980), Bohlin *et al.* (1983), Dickens, Brodie, & Bingham (1988), and Menzies (1974). Their values of E(B-V) and distances are from Heber & Kudritzki (1986) and Harris (1996).

Table 2. Rejected Stars.

Star ID	Spectral ^a type	l (°)	b (°)	FUSE Archival ID	Category ^b
BARNARD29	PAGB	58.97	+40.93	P1015201	3b
BD+35 4258	B0.5Vn	77.19	-4.74	P1017901/P1017902	3b
BD+48 3437	B1Iab	93.56	-2.06	P1018401/P1018402/P1018403	3a/c
CPD-691743	B0.5III _n	303.71	-7.35	P1013701	2a/c
CPD-721184	B0III	299.15	-10.94	S5140102	3a
CPD-741569	O9.5V	317.02	-18.68	P1015301	3a
HD 73	B1.5IV	114.17	-18.69	P1010101/P1010102	3a
HD 12740	B1.5II	135.30	-11.91	P1010701	3a
HD 22586	B2III	264.19	-50.36	P1011101	3a
HD 34656	O7II _f	170.04	+0.27	P1011301	2b/a
HD 66788	O8V	245.43	+2.05	P1011801	2a/b
HD 92702	B1Iab	286.15	+0.96	S5130301	3a/c
HD 93840	BN1Ib	282.14	+11.10	P1012701	3a
HD 119069	B1III	312.05	+16.12	P1014001	3b/a
HD 119608	B1Ib	320.35	+43.13	P1014201	3a
HD 125924	B2IV	338.16	+48.28	P1014701	3a
HD 146813	B1.5	85.71	+43.81	P1014901	3a
HD 149881	B0.5III	31.37	+36.23	P1015102	3a
HD 152218	O9.5IV _n	343.53	+1.28	P1015402	2b/a
HD 156359	O9.7Ib-II	328.68	-14.52	P1015502	2d
HD 158243	B1Iab	337.59	-10.64	P1015601	3d
HD 160993	B1Iab	345.61	-8.56	P1015701	3d
HD 163522	B1Ia	349.57	-9.09	P1015801	3d
HD 163758	O6.5Iaf	355.36	-6.10	P1015901	2d/b
HD 164816	O9.5III-IV	6.06	-1.20	P1016001	3a
HD 167402	B0Ib	2.26	-6.39	P1016201	3a/d
HD 168941	O9.5II-III	5.82	-6.31	P1016501/P1016502	3d
HD 172140	B0.5III	5.28	-10.61	P1016601/P1016602/P1016603	3a
HD 173502	B0.5III	5.36	-12.27	P1016701	3a/b
HD 175754	O8II _f	16.39	-9.92	P1016802	2d/b
HD 178487	B0Ib	25.78	-8.56	P1017201	3a/b
HD 179407	B0.5Ib	24.02	-10.40	P1017301	3a/b
HD 183899	B2III	13.07	-20.14	P1017601	3a
HD 195455	B0.5III	20.27	-32.14	P1017801	2a
HD 201638	B0.5Ib	80.29	-8.44	P1018001	3a
HD 214080	B1Ib	44.80	-56.92	P1018502	3a/d

Table 2—Continued

Star ID	Spectral ^a type	l (°)	b (°)	FUSE Archival ID	Category ^b
HD 215733	B1II	85.16	-36.35	P1018602	3a
HD 218915	O9.5Iab	108.06	-6.89	P1018801	3d/b
LS 4825	B1Ib-II	1.67	-6.63	P1016101	3c

^aThe original sources for spectral types are in Savage & Sembach (1994) and Sembach & Savage (1992).

^bThe category assigned to the star. See §2 for details. The letters indicate the reason for rejection; a: complex stellar continuum; b: blending with unidentified narrow stellar lines or strong HD λ 1031.91 contamination; c: low S/N ratio; d: presence of strong stellar wind features near or at the O VI 1031.93 line.

Table 3. Description of the Observations.

Star ID	FUSE Archival ID	Aperture/Mode ^a	Total Exposure Time per Observation (s)	S/N ^b ratio
BD+38 2182	P1012801	LWRS/TTAG	12226	55
HD 3827	P1010302	MDRS/HIST	2885	92
HD 18100	P1011002	MDRS/HIST	1932	69
HD 88115	P1012301	LWRS/HIST	4512	69
HD 97991	P1013001	LWRS/HIST	59	14
HD 100340	P1013201	HRS/HIST	5281	66
HD 116852	P1013801	LWRS/HIST	7212	77
HD 121800	P1014401	LWRS/HIST	3987	65
HD 121968	P1014501	LWRS/HIST	9301	54
HD 148422	P1015001/P1015002/P1015003	LWRS/TTAG	2063/3026/3243	28
HD 175876	P1016902	MDRS/HIST	1932	85
HD 177566	P1017003	LWRS/HIST	7764	74
HD 177989	P1017101	LWRS/HIST	10289	65
HD 219188	P1018902	MDRS/HIST	1660	72
HDE 225757	P1017701/P1017703	LWRS/TTAG	5805/6351	26
HDE 233622	P1012102	LWRS/HIST	4662	89
JL 212	P1010401	LWRS/HIST	5437	62
NGC 6397-ROB 162	A0260201	LWRS/TTAG	11500	31
NGC 5904-ZNG 1	A1080303	LWRS/TTAG	3900	20
NGC 5139-ROA 5342	A1080101	LWRS/TTAG	7400	11
NGC 6723-III 60	A1080201	LWRS/TTAG	5400	11
vZ 1128	P1014101/P1014102/P1014103	LWRS/TTAG	9151/8248/15610	25

^aTTAG: time-tagged mode; HIST: histogram mode

LWRS: 30×30 arcsec; MDRS: 4×20 arcsec; HRS: 1.25×20 arcsec

^bThe S/N ratio per resolution element ($\sim 20 \text{ km s}^{-1}$) measured around the O VI $\lambda 1031.93$ line.

Table 4. Description of the O VI Absorption.

Star ID	$[l, b]$	$[v_-, v_+]^a$ km s ⁻¹	W_λ^b mÅ	log N	log N_\perp^c	\bar{n}^d (10 ⁻⁸ cm ⁻³)
BD+38 2182	[182.2, +62.2]	[-75, 74]	123±14	14.10±0.07	14.05	1.05±0.17
HD 3827	[120.8, -23.2]	[-88, 53]	71± 8	13.80±0.04	13.40	1.00±0.09
HD 18100	[217.9, -62.7]	[-101, 87]	70±11	13.77 ^{+0.10} _{-0.13}	13.72	1.15±0.30
HD 88115	[285.3, -5.5]	[-152, 75]	250±12	14.44±0.02	13.42	2.45±0.11
HD 97991	[262.3, +51.7]	NA	≤61	≤13.69	≤13.58	≤1.60
HD 100340	[258.9, +61.2]	[-142, 156]	246±23	14.28 ^{+0.11} _{-0.16}	14.22	1.74±0.52
HD 116852 ^e	[304.9, -16.1]	[-96, 68]	179±11	14.30±0.02	13.74	1.36±0.06
HD 121800	[113.0, +49.8]	[-84, 136]	227±19	14.40±0.03	14.28	3.97±0.27
HD 121968	[334.0, +55.8]	[-96, 84]	98±18	13.97±0.06	13.89	0.88±0.12
HD 148422 ^e	[329.9, -5.6]	[-90, 43]	133±25	14.14±0.09	13.13	0.86±0.18
HD 175876 ^e	[15.3, -10.6]	[-114, 66]	146±11	14.14 ^{+0.10} _{-0.13}	13.40	1.90±0.49
HD 177566	[355.6, -20.4]	[-52, 66]	51± 8	13.65 ^{+0.06} _{-0.08}	13.19	1.32±0.21
HD 177989 ^e	[17.8, -11.9]	[-95, 101]	196±10	14.31±0.06	13.62	1.35±0.19
HD 219188 ^e	[83.0, -50.2]	[-85, 79]	99± 8	13.97±0.06	13.86	1.30±0.18
HDE 225757	[69.6, +4.9]	[-84, 72]	253±27	14.57±0.04	13.50	1.82±0.17
HDE 233622	[168.2, +44.2]	[-108, 72]	82±10	13.87 ^{+0.13} _{-0.19}	13.71	0.91±0.32
JL 212	[303.6, -61.0]	[-49, 100]	152±13	14.21±0.07	14.15	2.09±0.34
NGC 6397-ROB 162	[337.9, -11.4]	[-73, 111]	174±22	14.25±0.06	13.55	2.51±0.35
NGC 5904-ZNG 1	[3.5, +47.4]	[-70, 67]	181±34	14.41±0.08	14.28	1.11±0.21
NGC 5139-ROA 5342	[308.5, +15.4]	[-112, 56]	252±83	14.54 ^{+0.10} _{-0.12}	13.96	2.12±0.53
NGC 6723-III 60	[359.7, -16.7]	[-49, 87]	207±67	14.37 ^{+0.10} _{-0.12}	13.83	0.86±0.22
vZ 1128 ^f	[42.5, +78.7]	[-160, 100]	260± 7	14.49±0.03	14.48	0.98±0.07
Average±σ	14.17±0.28	13.77±0.37	1.56±0.75
Median	14.25	13.74	1.35

^aVelocity limits for integration of $N_a(v)$.

^bEquivalent widths are based on the O VI 1031.93 Å line.

^c $N_\perp = N \sin|b|$

^d $\bar{n} = N/d$, the average O VI density along the sight line.

^eSubstantial HD R(0) λ 1031.91 contamination in the O VI absorption at 1031.93 Å . See §4 for a discussion of the HD decontamination process.

^fSee Howk, Sembach, & Savage (2002) for details.

Table 5. Kinematical Description of the Low- and High-Ionization States.

Star ID	v_{exp}^a	Ar I		O VI		C IV		Si IV	
		$\langle v \rangle^b$	b^b	$\langle v \rangle^b$	b^b	$\langle v \rangle^b$	b^b	$\langle v \rangle^b$	b^b
BD+38 2182	0.4	-27.1	36.6	-3.4	35.2	-21.6	42.3	-11.8	47.8
HD 3827	-13.9	-28.1	29.6	-14.9	39.0
HD 18100	3.0	-8.0	19.8	-8.3	45.0	-14.2	27.6	-14.1	20.8
HD 88115	-6.8	-23.2	21.2	-22.1	59.2	-18.5	32.1
HD 97991	1.6	-2.7	24.9	3.5	41.9
HD 100340	3.3	-13.2	23.3	9.9	78.3	18.6	44.5	13.2	36.6
HD 116852	-26.4	-14.3	22.1	-13.1	38.7	-25.9	36.8	-28.7	34.1
HD 121800	-5.9	-6.9 ^c	18.6 ^c	12.1	52.0	-38.2	56.3	-47.9	50.2
HD 121968	-6.4	0.7	22.3	0.6	38.2	-21.5	29.8	-19.1	34.9
HD 148422	-40.2	-26.8	33.5	-14.1	35.5	-30.0	34.5	-35.9	31.7
HD 175876	10.7	-3.2	30.2	-16.3	59.2	21.2	28.4	18.9	25.7
HD 177566	-1.3	-8.1	22.9	0.3	32.6	-3.0	29.6
HD 177989	26.7	-12.7	17.3	11.2	49.5	27.3	41.9	25.5	36.9
HD 219188	0.4	-6.3	19.5	-7.9	43.8	10.7	40.6	8.7	36.3
HDE 225757 ^d	9.6	1.0	20.1	3.5	38.2
HDE 233622	-3.8	-0.1	27.8	-21.4	47.2
JL 212	-3.8	-8.4	18.4	14.2	37.0	28.2	22.8	20.4	22.1
NGC 6397-ROB 162 ^d	-14.3	-10.0	19.2	9.2	48.2
NGC 5904-ZNG 1	3.0	-0.9	18.7	-5.8	36.5
NGC 5139-ROA 5342 ^d	-31.3	-15.8	20.3	-17.5	43.2
NGC 6723-III 60 ^d	-3.2	-0.7	19.6	24.0	44.3
vZ 1128 ^e	1.5	-13.1	20.6	-31.3	52.8

Data for Ar I and O VI are from this investigation, while those for C IV and Si IV are from Savage, *et al.* (2001a).

^aThe expected Galactic rotational velocity based on the Galactic rotation curve of Clemens (1985).

^bBased on the Ar I $\lambda 1048.22$, O VI $\lambda 1031.93$, C IV $\lambda 1548.20$, and Si IV $\lambda 1393.76$ lines. Quantities $\langle v \rangle$ and b are in km s^{-1} and were calculated by Equations 6 and 7.

^c Only the component at lower $|v|_{LSR}$ was used to calculate $\langle v \rangle$ and b . See Figure 8.

^dThe LSR velocities are not well defined.

^eSee Howk *et al.* (2002a) for details.

Table 6. Ion Ratios of Si IV, C IV, N V, and O VI.

Star ID	$\frac{N(C\ IV)}{N(Si\ IV)}$	$\frac{N(C\ IV)}{N(O\ VI)}$	$\frac{N(Si\ IV)}{N(O\ VI)}$	$\frac{N(N\ V)}{N(O\ VI)}$
BD+38 2182	≥ 2.00	0.74 ± 0.14	≤ 0.39	...
HD 3827	...	≤ 3.08	≤ 0.49	...
HD 18100 ^b	$3.02 \pm (0.30, 0.26)$ ^a	0.65 ± 0.17	0.21 ± 0.06	0.10 ± 0.04
HD 88115	≥ 4.17	$0.20 \pm (0.36, 0.08)$	≤ 0.03	...
HD 97991	≥ 3.39	≥ 0.28
HD 100340 ^b	$3.31 \pm (0.70, 0.69)$	0.35 ± 0.11	0.11 ± 0.04	$0.06 \pm (0.03, 0.02)$
HD 116852 ^c	3.89 ± 0.20	0.68 ± 0.03	0.17 ± 0.01	$0.15 \pm (0.02, 0.03)$
HD 121800	≥ 1.23	$0.35 \pm (0.74, 0.14)$	≤ 0.19	...
HD 121968 ^d	≤ 5.00	$1.74 \pm (0.60, 0.38)$	$0.50 \pm (0.50, 0.17)$	0.26 ± 0.06
HD 148422 ^e	≤ 4.03	$0.60 \pm (0.61, 0.15)$	$0.31 \pm (0.31, 0.13)$	≤ 0.41
HD 175876	$1.95 \pm (0.95, 1.04)$	$0.23 \pm (0.11, 0.09)$	$0.12 \pm (0.06, 0.04)$...
HD 177566	≥ 3.24	$0.30 \pm (0.12, 0.09)$	≤ 0.08	...
HD 177989 ^f	$4.68 \pm (0.82, 0.88)$	$1.45 \pm (0.32, 0.34)$	0.31 ± 0.04	0.11 ± 0.02
HD 219188	$5.25 \pm (1.21, 1.03)$	$0.69 \pm (0.17, 0.13)$	$0.13 \pm (0.03, 0.02)$...
HDE 233622 ^g	$2.75 \pm (0.74, 0.79)$	0.26 ± 0.10	0.10 ± 0.04	≤ 0.23
JL 212 ^g	$2.82 \pm (0.14, 0.15)$	0.20 ± 0.03	0.07 ± 0.01	0.07 ± 0.05
Average ^h $\pm 1\sigma$	3.46 ± 1.09	0.60 ± 0.47	0.20 ± 0.13	0.12 ± 0.07
Models :				
CGF ⁱ	3.0-4.7	0.1-0.5	0.03-0.11	0.05-0.07
TML ^j	1.6-90	1.0-8.4	0.04-0.75	0.12-0.4
SNR ⁱ	12-20	0.1-0.2	≤ 0.01	0.05-0.09
CI ^k	27-50	0.15-0.45	≤ 0.02	0.09-0.17

Data for C IV and Si IV are always from Savage *et al.* (2001a) unless noted otherwise.

^a $3.02 \pm (0.30, 0.26) = 3.02^{+0.30}_{-0.26}$.

^b Si IV, C IV, and N V column densities are from Savage & Sembach (1994).

^c Si IV, C IV, and N V column densities are from Sembach & Savage (1994).

^d N V column density is from Sembach, & Savage (1992).

^e N V column density is from Sembach *et al.* (1997).

^f Si IV, C IV, and N V column densities are from Savage *et al.* (2001b).

^g Si IV, C IV, and N V column densities were measured by the authors of the present article using STIS observations.

^h The lower and upper limits were not included in the calculation.

ⁱ The Cooling Galactic Fountain (CGF) model of R. Benjamin (2002, private communication) and the cooling SNR model of Slavin & Cox (1992). The quoted numbers are from Sembach *et al.* (1997).

^j The Turbulent Mixing Layer (TML) model of Slavin *et al.* (1993). The quoted ranges cover all values that are predicted by the TML models for the entrainment velocities, abundances, and postmixed gas temperatures used by Slavin *et al.* (1993).

^k The magnetized Conductive Interface (CI) model of Borkowski *et al.* (1990). The values are appropriate for magnetic field inclinations between 0° and 85° (relative to the front normal) and for a conduction front age of 2.5×10^5 years.

Table 7. Closely Aligned Galactic and Extragalactic Sight Lines.

Star/AGN ID	$[l, b]$	Δ^a ($^\circ$)	d (pc)	$[v_-, v_+]^b$ (km s^{-1})	$\log N$	Note ^c
HD 175876	[15.3, -10.6]	...	2360	[-114, 66]	$14.14^{+0.10}_{-0.13}$	MW
HD 177989	[17.8, -11.9]	2.8	4910	[-95, 101]	14.31 ± 0.06	MW
vZ 1128	[42.5, +78.7]	...	10200	[-160, 100]	14.49 ± 0.03	MW
PG 1402+261	[33.0, +73.5]	5.7	...	[-120, 115]	14.53 ± 0.05	MW
HD 219188	[83.0, -50.2]	...	2330	[-85, 79]	13.97 ± 0.06	MW
NGC 7469	[83.1, -45.5]	4.7	...	[-65, 45]	13.96 ± 0.09	MW
				[-370, -235]	14.18 ± 0.12	MS
				[-235, -120]	14.22 ± 0.16	LG
NGC 7714	[88.2, -55.6]	6.2	...	[-60, 45]	13.85 ± 0.15	MW
				[-310, -230]	14.13 ± 0.13	MS
HD 121800	[113.0, +49.8]	...	2050	[-84, 136]	14.40 ± 0.03	MW
PG 1351+640	[111.9, +52.0]	2.4	...	[-100, 100]	14.38 ± 0.07	MW
				[-160, -100]	13.67 ± 0.24	C
				[100, 160]	13.44 ± 0.26	Oth
Mrk 279	[115.0, +46.9]	3.2	...	[-115, 100]	14.41 ± 0.03	MW
				[-210, -115]	13.67 ± 0.14	C
HDE 233622	[168.2, +44.2]	...	2650	[-108, 72]	$13.87^{+0.13}_{-0.19}$	MW
Mrk 106	[161.1, +42.9]	5.3	...	[-100, 100]	14.45 ± 0.09	MW
				[-150, -100]	13.81 ± 0.22	A
Mrk 116	[160.5, +44.8]	5.5	...	[-125, 110]	14.21 ± 0.06	MW
BD+38 2182	[182.2, +62.2]	...	3890	[-75, 74]	14.10 ± 0.07	MW
Mrk 421	[179.8, +65.0]	3.0	...	[-130, 100]	14.39 ± 0.04	MW
				[100, 185]	13.51 ± 0.22	EPn
HS 1102+3441	[188.6, +66.2]	4.9	...	[-140, 95]	14.71 ± 0.08	MW
				[95, 210]	14.30 ± 0.12	EPn
Ton 1187	[188.3, +55.4]	7.5	...	[-90, 65]	14.35 ± 0.08	MW

Table 7—Continued

Star/AGN ID	$[l, b]$	Δ^a ($^\circ$)	d (pc)	$[v_-, v_+]^b$ (km s^{-1})	$\log N$	Note ^c
HD 18100	[217.9, −62.7]	...	1660	[−101, 87]	$13.77^{+0.10}_{-0.13}$	MW
HE 0238-1904	[200.5, −63.6]	7.9	...	[−120, 110]	14.33 ± 0.09	MW
HD 100340	[258.9, +61.2]	...	3540	[−142, 156]	$14.28^{+0.11}_{-0.16}$	MW
Mrk 734	[244.8, +63.9]	7.0	...	[−35, 140] [140, 275]	14.55 ± 0.08 14.10 ± 0.19	MW EPn
JL 212	[303.6, −61.0]	...	2510	[−49, 100]	14.21 ± 0.07	MW
Fairall 9	[295.1, −57.8]	5.4	...	[−110, 100] [100, 275]	14.38 ± 0.09 14.33 ± 0.10	MW MS
HD 177566	[355.6, −20.4]	...	1100	[−52, 66]	$13.65^{+0.06}_{-0.08}$	MW
NGC 6723-III 60	[359.7, −16.7]	5.4	8800	[−49, 87]	$14.37^{+0.10}_{-0.12}$	MW
Tol 1924-416	[356.9, −24.1]	3.9	...	[−70, 95]	14.62 ± 0.05	MW

Data for the thick disk and the high velocity absorption toward extragalactic sight lines are from Savage *et al.* (2002) and Sembach *et al.* (2002), respectively.

^aAngular separation is measured from the first sight line in each group.

^bVelocity limits for integration of $N_a(v)$.

^cIdentification of the O VI absorption: MW= Milky Way thick disk/low halo, A= Complex A, C= Complex C, EPn= Extreme Positive (North), LG= Local Group, MS= Magellanic Stream, Oth= Other. See Sembach *et al.* (2002) for details on HVC identification.